SUBJECT-SPECIFIC 4D ULTRASOUND LIVER MODEL AND DYNAMIC PHANTOM FOR ROBOTIC-ASSISTED LIVER BIOPSY STUDY

LI CHENG

(*B.Eng, Shanghai Jiao Tong University, China*)

A THESIS SUBMITTED

FOR THE DEGREE OF DOCTOR OF PHILOSOPHY

DEPARTMENT OF BIOMEDICAL ENGINEERING

NATIONAL UNIVERSITY OF SINGAPORE

2015

DECLARATION

I hereby declare that this thesis is my original work and it has been written by me in its entirety. I have duly acknowledged all the sources of information which have been used in the thesis.

This thesis has also not been submitted for any degree in any university previously.

Li Cheng

Aug. 2015

ACKNOWLEDGEMENTS

First of all, I would like to express my deepest thanks to my supervisor Dr. Yu Haoyong for his invaluable guidance and continuous support of my PhD study and research. He has taught me so many things over the years, and made me understand that any achievement comes from positive attitude, appropriate methodology and most indispensably, hardworking. I am eternally grateful for his patience and all the pearls of wisdom he has generously shared with me.

Then, I would like to thank Dr. Liu Jimin and his group members, Prof. Tian Qi, Dr. Chi Yanling, Mr. Huang Su from Singapore Bioimage Consortium (SBIC), A*STAR. Dr. Liu has introduced me to the research field and guided me generously and professionally. I enjoyed the time that worked with him and his team. Their passions in research and work have left lasting impressions on me.

Special thanks go to Dr. Wu Jiaze, another senior who played a significant role in my research. His suggestion on technical details is always useful, and he is so creative that always inspires me along the research journey. He is very heartwarming and encouraging. The work done in this thesis would not have been possible without his help.

I would also like to thank my colleagues in my laboratory: Mr. Kyung-Ryoul Mun, Mr. Chen Gong, Dr. Guo Zhao, and Dr. Huang Sunan. My PhD life becomes more enjoyable because of their company and support.

Everything I have achieved in my life is all only possible thanks to the care and love from my family. I grew up in a single-parent family, and my father is

the best father a son could ever wish for. His optimistic attitude has been always encouraging me to keep smile no matter how tough life is.

Last but not least, I would like to thank my dearest girlfriend. She has sacrificed a lot to put up with me when I was in bad mood, and support me unconditionally all the time during these years. I feel sorry that I could not spend enough time with her because of my busy schedule of study and research. This thesis is dedicated to her.

CONTENTS

DECLARATION ..... **II**

ACKNOWLEDGEMENTS ..... **III**

SUMMARY ..... **VIII**

LIST OF PUBLICATIONS ..... **X**

LIST OF TABLES ..... **XII**

LIST OF FIGURES ..... **XIII**

LIST OF ABBREVIATIONS ..... **XVIII**

CHAPTER 1. INTRODUCTION AND BACKGROUND **1**

1.1 Introduction **2**
1.2 Background **4**
1.2.1 The liver and liver biopsy *4*
1.2.2 Respiratory organ motion *6*
1.2.3 Existing methods to handling respiratory organ motion in clinical practice *9*
1.2.4 Related works for obtaining subject-specific respiratory motion *12*
1.3 Objective and Structure of the Thesis **16**

CHAPTER 2. EXTRACTION OF RESPIRATORY SIGNAL FROM INTRA-OPERATIVE ULTRASOUND IMAGE **20**

2.1 Introduction **21**
2.2 Adaptive Template Searching **22**
2.2.1 Noise reduction *23*
2.2.2 Template region *23*
2.2.3 Similarity measurement *24*
2.2.4 Adaptive searching *24*
2.3 Experiments **26**
2.4 Results and Discussion **28**
2.4.1 Noise reduction *28*
2.4.2 Template region *31*
2.4.3 Adaptive searching *33*
2.4.4 Consistency validation *36*
2.5 Limitations **41**
2.6 Conclusion **42**

CHAPTER 3. SUBJECT-SPECIFIC AND RESPIRATION-CORRECTED 4D ULTRASOUND LIVER MODEL **43**

3.1 Introduction **44**
3.2 System Overview **46**
3.3 Experimental Setup **48**

3.4 Generation of the Liver Model **50**
3.5 Evaluation **53**
3.5.1 Manual annotations *54*
3.5.2 Evaluation measures *55*
3.6 Motion Analysis **56**
3.7 Results **57**
3.7.1 4D liver model *57*
3.7.2 Accuracy of the liver model *58*
3.7.3 Motion analysis *62*
3.8 Discussion **68**
3.9 Limitations **70**
3.10 Conclusion **70**

CHAPTER 4. PHANTOM STUDY - DYNAMIC LIVER PHANTOM: DESIGN, VALIDATION, AND TEST FOR US BIOPSY SYSTEM **72**

4.1 Introduction **73**
4.2 Supporting Data and Design Concepts **74**
4.2.1 Supporting data *74*
4.2.2 Design concepts *75*
4.3 Mechanical Design of the Phantom **76**
4.4 Phantom Control **79**
4.5 Experiments **81**
4.5.1 Validation *81*
4.5.2 Biopsy test on the phantom *84*
4.6 Results and Discussion **86**
4.6.1 Validation *86*
4.6.2 Biopsy test on the phantom *88*
4.7 Limitations **92**
4.8 Conclusion **92**

CHAPTER 5. EXPERIMENTAL STUDY - CREATION OF SIMULATED TUMORS FOR REAL-TIME ULTRASOUND IMAGE-GUIDED LIVER BIOPSY **94**

5.1 Introduction **95**
5.2 Creation of Simulated Liver Tumors **96**
5.2.1 Agar-based tumor model *96*
5.2.2 Vaseline-based tumor model *97*
5.3 Experiments **98**
5.3.1 Ex-vivo experiment *98*
5.3.2 Live animal (in-vivo) experiment *99*
5.3.3 Targeting of simulated lesion *101*
5.4 Results **106**
5.4.1 Results of biopsies *106*
5.4.2 Comparison of ultrasound image of the target area *107*
5.4.3 Quantitative analysis of the injection *108*
5.5 Discussion **110**
5.6 Limitations **113**

5.7 Conclusion **114**

CHAPTER 6. SUPPLEMENTARY WORK: A QUANTITATIVE EVALUATION FUNCTION FOR 3D TREE-LIKE STRUCTURE SEGMENTATIONS IN LIVER IMAGES **115**

6.1 Introduction **116**
6.2 Description of QEF **118**
6.3 Validation of QEF **123**
6.4 Experimental Results and Discussion **126**
6.5 Limitations **132**
6.6 Conclusion **133**

CHAPTER 7. CONCLUSION AND RECOMMENDATIONS FOR FUTURE WORK **135**

7.1 Contributions **136**
7.2 Recommendations for future work **139**

BIOBLIOGRAPHY **142**

SUMMARY

It is challenging to accurately perform liver intervention procedures such as biopsy and ablation in clinical practice, where the target (a tumor, usually) is moving during the treatment due to respiratory liver motion and deformation. Such motion makes both imaging, and locating of the target area, more difficult. In this thesis, three aspects in particular are focused on, namely image processing, phantom study, and experimental study, to develop new techniques and look for practical solutions to this problem. Specifically, we apply respiratory signal extraction and 4D liver modeling, dynamic liver phantom evaluation, ex-vivo and in-vivo biopsy testing, and hybrid schemes to improve biopsy efficiency and accuracy.

In the first part of the thesis, a new approach providing fast and robust extraction of respiratory signal from real-time ultrasound images is introduced to identify the respiratory phase of the liver. This approach is able to achieve accurate motion estimation within several seconds, and thus demonstrates its suitability as a build-in respiratory motion-tracking algorithm for the US image-guided biopsy robotic system. Moreover, a novel method for generating a subject-specific and respiration-corrected 4D ultrasound liver model is described, to visualize and analyze liver motion during respiration. This method creates a sequence of respiration-corrected 3D image volumes, to capture liver motion, and hence to provide subject-specific preoperative information to improve the accuracy of diagnosis and treatment.

Second, a novel dynamic liver phantom, which can be applied as a liver motion simulator, is presented for the development and validation of an image-guided biopsy system. By tracking the marker position inside the phantom, we found this dynamic phantom capable of providing stable and repeatable movement cycles to simulate subject-specific respiration under different settings of parameters. This phantom reduces the reliance on living subjects, and at the same time also reduces the potential harmful effects of tested devices on living subjects.

Third, to obtain ideal testing objects for the US image-guided biopsy study, a unique Vaseline-based technique, for easy creation of simulated tumors of different sizes inside porcine livers, is proposed. Its performance was investigated in ex-vivo and in-vivo biopsy studies. This technique provides practical solutions to the problem of a lack of ideal testing objects, and has value in terms of application in any biopsy-related study, such as biopsy training, biopsy imaging, and biopsy needle function testing and so on.

In addition, a supplementary work on quantitative evaluation of vascular segmentations in liver images is illustrated, because analysis of vascular structure from volumetric datasets plays a crucial role in many clinical applications, including biopsy. Though this work was based on automatic segmentation results from patients' CT datasets, it is worth mentioning that this method is also suitable for vessel segmentations from US volume data as well.

List of Publications

Journal Papers

1. **C Li**, J Wu, Y Chi, J Liu, Q Tian, H Yu, 'A quantitative evaluation function for 3D tree-like structure segmentations in liver images,' *Computer Methods in Biomechanics and Biomedical Engineering: Imaging & Visualization*, pp. 1-9, 2014.

2. **C Li**, J Wu, A Gogna, BS Tan, J Liu, H Yu, 'Subject-specific and Respiration-corrected 4D Liver Model from Real-time Ultrasound Image Sequences,' *Computer Methods in Biomechanics and Biomedical Engineering*. (Accepted)

3. **C Li**, JY Teo, J Wu, A Gogna, BS Tan, LL Ooi, J Liu, H Yu, 'Creation of Clinically-differential Tumor Mimic Model Using Vaseline-based Materials with Barium Sulfate for the Validation of Real-time Ultrasound Image-guided Liver Biopsy System,' *Biomedical Engineering: Applications, Basis and Communications*, 28: 1650003, 2016.

4. J Wu, **C Li**, S Huang, F Liu, BS Tan, LL Ooi, H Yu, J Liu, 'Fast and robust extraction of surrogate respiratory signal from intra-operative liver ultrasound images', *International Journal of Computer Assisted Radiology and Surgery (IJCARS)* 1-9, 2013.

5. J Wu, **C Li**, A Gogna, BS Tan, LL Ooi, J Liu, H Yu, 'Technical Note: Automatic Real-Time Ultrasound Tracking of Respiratory Signal Using Selective Filtering and Dynamic Template Matching', *Medical Physics*, 2015, 42(8): 4536-4541.

Conference Papers

1. **C Li**, SP Ang, J Liu, H Yu, 'A Dynamic Liver Phantom for Ultrasound Image Guided Biopsy', *15th International Conference on Biomedical Engineering (ICBME)*, Springer International Publishing, 2014: 152-155.
2. **C Li**, JY Teo, J Wu, J Liu, LL Ooi, H Yu, 'Ultrasound Image Guided Biopsy on Vaseline-based Mimic Porcine Liver Tumors', *11th Anniversary Asian Conference on Computer Aided Surgery (ACCAS)*, 2015.
3. J Wu, **C Li,** S Huang, F Liu, BS Tan, LL Ooi, H Yu, J Liu, 'A Fast and Robust Method to Extract Respiratory Motion from Liver Ultrasound Images', *27th International Congress and Exhibition on Computer Assisted Radiology and Surgery (CARS)*, 2013, S60-S61.
4. J Wu, Y Chi, **C Li**, BS Tan, LL Ooi, J Liu, 'Automatic and Real-time Identification of Breathing Pattern from Ultrasound Liver Images', *joint 6th International Workshop on Medical Imaging and Augmented Reality (MIAR) and 8th MICCAI Workshop on Augmented Environments for Computer-Assisted interventions (AE-CAI)*, 2013, 27-34.

List of Tables

Table 2.1 Computation time for different template region sizes. The image sequences and corresponding template regions are the same as in Figure 2.5. 32

Table 2.2 Comparison of computation time for center-fixed searching strategy, and adaptive searching strategy. The image sequences and corresponding template regions are the same as in Figure 2.6......36

Table 2.3 Consistency is quantitatively analyzed using the correlation coefficient (CC) metric. The image sequences and selected template regions are the same as in Figure 2.7.....39

Table 3.1 Profile of four volunteers......48

Table 3.2 Overlap of liver boundary at EE and EI of half respiratory cycle. .59

Table 3.3 Matching error of eight landmarks......59

Table 4.1 Average position reading of 10 cycles for 3 markers (unit: mm)....86

Table 5.1 Average tumor size from the injected mixtures......109

Table 6.1 Quality evaluation values for the vessel segmentation shown in Figure 6.3(B)-(D) taking (A) as reference standard ground truth 125

Table 6.2 Quality evaluation values for the vessel segmentation shown in Figure 6.4. [a] *R: Resolution, D: Dimension,* [b] *Se: sensitivity, Sp: specificity, Acc: accuracy*.....131

List of Figures

Figure 1.1 Liver biopsy [4].....2

Figure 1.2 Orthogonal slices showing the liver and its position in the upper abdomen. (a) transversal or axial, (b) coronal, (c) sagittal view [33].....4

Figure 1.3 Principle of trucut biopsy [56].....5

Figure 1.4 Mechanics of breathing [31].....7

Figure 1.5 Structure of the thesis.....17

Figure 2.1 The flowchart of ATS. MIUE (Model-based Image Understanding Environment) is a customized imaging tool developed based on our in house software platform [114].....23

Figure 2.2 The adaptive searching strategy updates searching center on current frame, based on the matched result of previous frame. Due to the slow variation of the liver tissue on two successive frames, the searching space (dashed green square on the right subfigure) can be very small.....26

Figure 2.3 Experimental setup. On the left side, A: US transducer with the probe holder for imaging; B: NDI Aurora EM tracking device; C: an EM sensor tracked by B. On the right side, the laptop belongs to a part of the Terason US system, which is used for displaying the acquired images, which are simultaneously loaded into our MIUE framework on the bigger monitor 27

Figure 2.4 Experiment results of noise reduction. X-axis: time; y-axis: vertical displacement 30

Figure 2.5 Experiment results of extracted respiratory motion curves use increasing template region sizes. X-axis: time; y-axis: vertical displacement. 32

Figure 2.6 Experiment results of center-fixed searching strategy with increasing searching range (row 3-5), and adaptive searching strategy with smaller searching ranges (row 6-7). X-axis: time; y-axis: vertical displacement. 35

Figure 2.7 Visual and quantitative comparison between the identified motion curves (in red) and the EM-tracked reference motion (in green). The motion

curves extracted near the liver boundaries (A, B, F, H, K, L) and vessels (D, I) highly approximate to the reference respiratory curves X-axis: time; y-axis: vertical displacement. 38

Figure 3.1 Schematic diagram of system overview 48

Figure 3.2 Experimental setup. A: 2D US probe; B: NDI EM tracking device; C: EM sensor on the umbilicus of volunteer tracked by B; D: Probe holder. 49

Figure 3.3 Overall processing flow of 4D ultrasound imaging using a 2D ultrasound probe, and a robotic arm enabling tilt-scanning of the probe. A series of 3D images is created to capture the moving liver from EE to EI......51

Figure 3.4 Establishment of the coordinate system on the 2D ultrasound image plane, and manual annotation of liver boundary (in red color) and an internal landmark (in blue color). 54

Figure 3.5 Three volumes are reconstructed at three different respiratory phases (left: EE, middle: Middle phase, right: EI). Three orthogonal views of the US volumes are shown 58

Figure 3.6 Individual landmark trajectories as annotated by three engineers (presented in three different colors) of four landmarks (n = 1, 3, 5, 7) 61

Figure 3.7 The overlay of the liver boundary (A, B) and internal landmarks (C, D) of the two subjects 1(A, C) & 3(B, D). The scale is shown on the left side of each image. The timing of the movement is shown in the color map style at the top. The coordinate system, fixed on the center of the image, is shown in white. 64

Figure 3.8 The displacement, velocity, and acceleration in Y direction of the liver boundary for the four subjects in Pr. S denotes subject. The figure was plotted in a black dash line, solid red line, short dash blue line, and dash dot pink line, for subjects 1 to 4, respectively. 65

Figure 3.9 The displacement, velocity, and acceleration in Y direction of the landmarks for the four subjects in Pr. S denotes subject. The figure was plotted in a black dash line, solid red line, short dash blue line, and dash dot pink line for subjects 1 to 4, respectively. The scale is intentionally kept the same as in Figure 3.8......66

Figure 3.10 The displacement, velocity, and acceleration in X direction of the landmarks for the four subjects in Pr. S denotes subject. The figure was

plotted in a black dash line, solid red line, short dash blue line, and dash dot pink line for subjects 1 to 4, respectively. The scale is intentionally kept the same as in Figure 3.8......67

Figure 4.1 Liver movement in the CC direction is very close to that of the diaphragm [118].....75

Figure 4.2 Design of the phantom.....77

Figure 4.3 Prototype of the phantom. A: chest-like case; B: actuator holder; C: sponge holder; D: Firgelli L16 actuator; E: pushing plate. 79

Figure 4.4 Customized Labview program for the actuator.....81

Figure 4.5 Coordinates definition of the phantom.....81

Figure 4.6 Placement of 3 steel bolts on the surface of porcine liver.....82

Figure 4.7 Movement of the pushing plate from the start position (A, 0mm) to the maximum position (B, 20mm) in the X direction.....83

Figure 4.8 Detection of the position of markers using Terason t3000 ultrasound probe (A), and real-time US image of the marker (in red circle, B-E)......84

Figure 4.9 Targeting of the injected simulated tumor. Red rectangle: target; yellow arrow: trajectory of biopsy needle; green arrow: boundary of porcine liver. 86

Figure 4.10 The side view of the pathways of 3 markers as averages.....87

Figure 4.11 A successful (A) and an unsuccessful (B) biopsy attempt, respectively 89

Figure 4.12 Visual check on injected simulated tumor.....90

Figure 5.1 Materials for agar-based tumor model: agar powder (left) and glycerol (right)......96

Figure 5.2 Condition of the agar-based mixture: liquid when heated to greater than 50 ^{o} Centigrade (left); solid at room temperature (26 ^{o} Centigrade, right). 97

Figure 5.3 Making the Vaseline-based tumor model: Vaseline jelly (left); hot water bath (right). 97

Figure 5.4 Addition of clinical barium sulfate to the Vaseline-based mixture 98

Figure 5.5 Injection of Vaseline-based simulated tumor model in ex-vivo experiment 99

Figure 5.6 Preparation of the micropig for in-vivo experiment. 100

Figure 5.7 Injection of Vaseline-based simulated tumor model in live animal (in-vivo) experiment. 101

Figure 5.8 Setup of the ex-vivo (A) and in-vivo (B) experiments. 102

Figure 5.9 Biopsy attempt without cutting the abdominal skin of the micropig. The red circle shows the bending of the biopsy needle during insertion 104

Figure 5.10 Delivering the biopsy with the needle holder. A: ex-vivo experiment; B: in-vivo experiment. Red arrows: the needle holder. 105

Figure 5.11 View on gross pathology of injected simulated tumors (left column), and successful biopsy attempts on injected simulated tumors (right column). Top row: an agar-based simulated tumor; Middle and bottom row: Vaseline-based simulated tumors with barium sulfate, in ex-vivo and in-vivo experiment, respectively. 107

Figure 5.12 Comparison between real-time ultrasound images of simulated tumors with/without barium sulfate. Left: Vaseline-based simulated tumor with barium sulfate; right: agar-based simulated tumor. Red arrow: location of target; Yellow arrow: 'shadow' phenomenon. 108

Figure 5.13 Comparison between real-time ultrasound images of simulated tumors with/without barium sulfate. Left: Vaseline-based simulated tumor with barium sulfate; right: Vaseline-based simulated tumor without barium sulfate. Red arrow: location of target; Yellow arrow: 'shadow' phenomenon. 108

Figure 5.14 Comparison of the 'shadow' size for different amounts of injected material. Left: 3 ml of mixture injected; right: 10 ml of mixture injected. 109

Figure 6.1 Flow-chart to show how this quantitative evaluation function works. 119

Figure 6.2 One example to showcase the situation where the overlap volume ratio of two volumes is high, but their skeletons are significantly different. Red line (with width) represents the skeleton of the volume. 121

Figure 6.3 Branch level division of a typical tree-like structure: Red circle identify the root of this tree; Black color branch: level 1 (i=1); Blue color branch: level 2 (i=2); Green color branch: level 3 (i=3); Orange color branch: level 4 (i=4). 122

Figure 6.4 One example of segmentation results to show the properties of COSB and for its validation. (A): Reference-standard. (B)-(D): Segmentation results under different threshold setting. In red color: hepatic vein; green color: portal vein; black color in (C): ungrouped vessel pieces. 124

Figure 6.5 Eight groups of liver vessel segmentation results to test the performance of COSB and other commonly-used QEFs (Se, Sp, Acc). CT01-08_GT: Reference-standard ground truth. CT01-08_Rst: Segmentation results using context-based voting algorithm. In red color: hepatic vein; green color: portal vein. 128

Figure 6.6 Averages of human scores (HS), Acc, Se, Sp and COSB values on eight groups of segmentation results. 132

Figure 7.1 Solution with proposed techniques in an integrated manner..... 139

List of Abbreviations

1D	One-dimensional
2D	Two-dimensional
3D	Three-dimensional
4D	Four-dimensional
US	Ultrasound
CT	Computed Tomography
MR	Magnetic Resonance
MRI	Magnetic Resonance Imaging
ABC	Active Breathing Control
FH	First Hit (of the biopsy)
EM	Electromagnetic
ATS	Adaptive Template Searching
SI	Superior-Inferior
AP	Anterior-Posterior
LR	Left-Right
CC	Correlation Coefficient
ROI	Region Of Interest
SNR	Signal-to-Noise Ratio
QEF	Quantitative Evaluation Function
EE	End of Exhale
EI	End of Inhale

CHAPTER 1. INTRODUCTION AND BACKGROUND

This Chapter introduces the background, motivation, and objectives of the thesis.

1.1 Introduction

Liver disease, especially liver cancer, is one of the leading causes of death worldwide [1]. An accurate diagnosis of all types of liver disease in their early stages is a key factor for successful treatment, and in avoiding patients suffering from disease progression and facing the risk of losing all liver function. End-stage liver disease is usually fatal [2]. For the last several decades, liver biopsy has been considered as the gold standard for assessing the stage and the grade of liver disease (Figure 1.1). More specifically, it has been widely applied to diagnose unexplained liver diseases or abnormal liver function tests, sample suspicious tumor cells, determine the severity of liver diseases including non-alcoholic liver disease, certain liver disease such as chronic hepatitis B or C, primary biliary cirrhosis, autoimmune hepatitis or Wilson's disease, and monitor the liver after a liver transplantation [3].

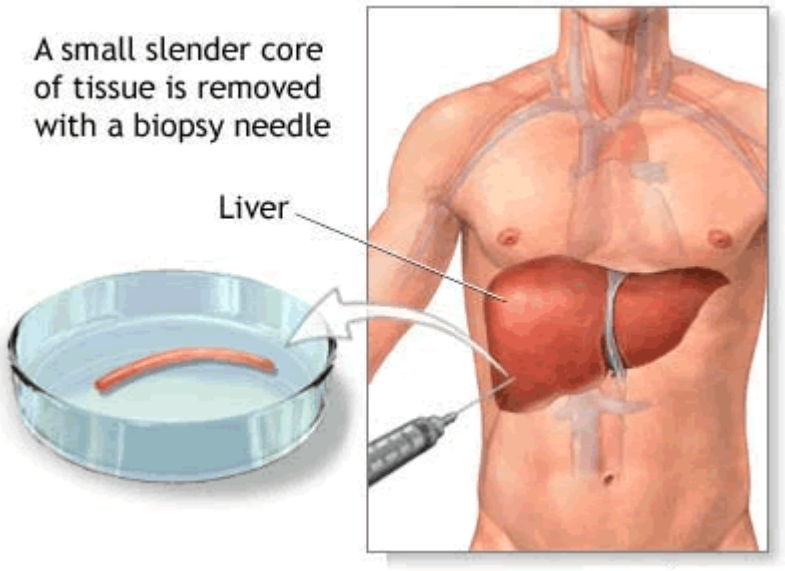

Figure 1.1 Liver biopsy [4]

However, liver biopsy is an invasive examination, and its accuracy is affected by liver motion due to respiration. Although it has become possible to employ liver biopsy with minimally invasive techniques under the guidance of

real-time 2D ultrasound image, accurate percutaneous liver biopsy is still difficult and challenging.

Many methods have been reported to handle the respiratory liver motion problem in clinical practice, where this issue is the chief difficulty during an image-guided biopsy procedure. These methods, physically or physiologically, ease the breathing-induced liver motion in a 'straightforward' way, and specifically, can be divided into the following categories: breath-holding [5, 6], gating [7-10], tracking [11-13], coaching and bio-feedback [14-17]. However, all of these methods have limitations – such as requiring patients' participation, which is not always possible, or making strong assumptions on the regularity of the respiratory motion. These measures can, in the end, add extra cost or a psychological burden to the patient. In this study, we look for clinically practical solutions for the problem of respiratory liver motion, on the assumption that free-breathing of the subjects is allowed during the whole procedure of diagnosis and treatment.

In terms of image-guided methods applied in the treatment of liver intervention procedures, MR- (Magnetic Resonance), CT- (Computed Tomography) and US- (Ultrasound) based solutions have been reported in the literature [18-28, 30-36]. Traditionally, to capture the respiratory motion of the liver, MRI has been seen to be preferable to CT imaging, mainly because patients are not exposed to ionizing radiation, and the fact the orientation of the scanned slices can be chosen freely. However, image-guided methods based on MR datasets are time-consuming and expensive. At present, US-based image processing algorithms to handle respiratory liver motion are becoming more and more popular, due to the advantages of their economy,

safety, flexibility, and real-time properties. Specifically, this research will focus on respiration-corrected 4D US.

1.2 Background

1.2.1 The liver and liver biopsy

The liver is both the largest internal organ and the largest gland in the human body, and performs a major role in metabolism with numerous functions in the human body, including regulation of glycogen storage, decomposition of red blood cells, plasma protein synthesis, hormone production, and detoxification [29, 96]. Figure 1.2 [33] shows orthogonal slices through the abdomen to demonstrate the exemplary shape of the liver, and its position.

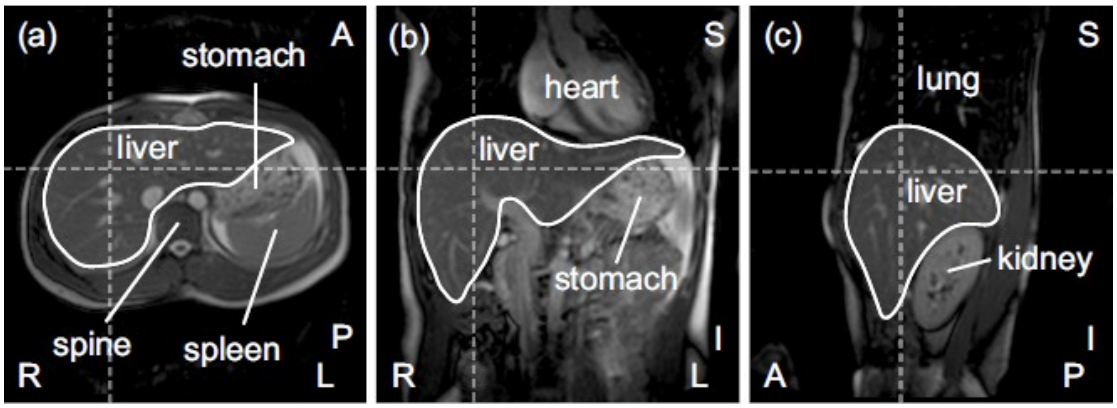

Figure 1.2 Orthogonal slices showing the liver and its position in the upper abdomen. (a) transversal or axial, (b) coronal, (c) sagittal view [33]

As mentioned in the previous section, liver biopsy is a procedure that involves obtaining a small piece of liver tissue, which is then analyzed in the laboratory. It is an important and effective diagnostic tool for clinicians in determining the severity and aggressiveness of liver diseases, especially liver cancer (non-resectable tumors). The principle of trucut biopsy that explains the detail on procedures of biopsy is shown in Figure 1.3 [56].

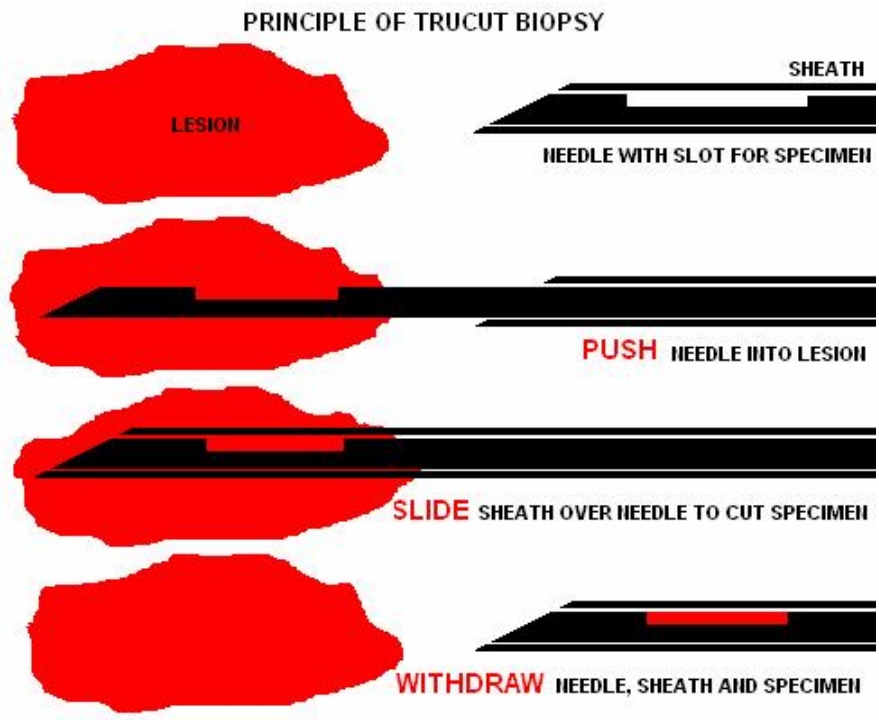

Figure 1.3 Principle of trucut biopsy [56]

The typical biopsy needle (Figure 1.3) has an outer cannula, an inner tube, and a stylet. A snare in the form of a coil is provided between the distal ends of the outer cannula and the inner tube. The coil is coupled to a sleeve affixed to the inner surface of the outer cannula using axially directed coupling elements. Upon rotation of the inner tube with respect to the outer cannula, the coil will decrease in diameter to either sever or hold the biopsy piece within the outer needle.

In practice, once the outer cannula reaches the surface of the liver, the stylet will cut a small incision before the pushing step. Then, the stylet will progress inside of the tumor, and the outer cannula will slide in. These steps are called ‘First Hit’ (FH). After FH, the inner part will move out with the sample, but the outer cannula will be fixed on the target position to ensure the next samples will also be taken at the right spot. Since the outer cannula is fixed

and can follow the movement of the tumor caused by respiration, we can say that if there is a successful FH, the biopsy is successful.

It is worth mentioning that for the diagnosis of liver cancer, other commonly used clinical techniques include blood test, ultrasonography, and computed tomography [38]. In the blood test, most patients with hepatoma demonstrate a positive reaction to Alpha Fetal Protein. However, it cannot be implied the liver is normal when the reaction is negative. In the ultrasonography, the difference of texture between hepatoma segmented and normal tissue can be observed. However, the ultrasonic image may not clearly show the region of interest of possible carcinoma due to its resolution and field of view limitations. CT cannot detect small hepatomas, and some patients are allergic to the contrast medium which is necessary for the CT imaging. Thus, although biopsy is an invasive examination, it is frequently used as a final confirmation method of the diagnosis of liver disease. The information gained from this procedure cannot be obtained from other, less invasive tests [37].

1.2.2 Respiratory organ motion

The main types of lethal cancer include liver, lung, stomach, colon, breast, and prostate cancer. Unfortunately, all these sites are affected by respiratory motion. This introductory section provides an overview of respiratory motion and the resulting issues in the liver biopsy procedure.

A) The mechanics of breathing

Human breathing refers to the exchange of air between an organism′s circulatory system and its external environment. The main muscles involved in breathing are the diaphragm, which is the large muscle that forms the floor of

the chest cavity, and the intercostal muscles, which are attached to the ribs. The breathing mechanism involves the action of these muscles, such that the transport of oxygen and carbon dioxide is continuing. In order to breathe, we must continuously contract and relax our respiratory muscles about 30,000 times a day or a billion times for a lifetime of 90 years [46].

Breathing consists of two phases, namely, inhalation (or inspiration) and exhalation (or expiration). During inhalation, the diaphragm actively contracts and pushes the contents of the abdomen in inferior direction [33]. At the same time, the external intercostal muscles pull the ribs up and further expanding the thoracic cavity. During exhalation, generally, the diaphragm and the external intercostal muscles passively relax, thereby the volume of the thoracic cavity decreases and the abdominal organs move up in superior direction again (Figure 1.4) [31].

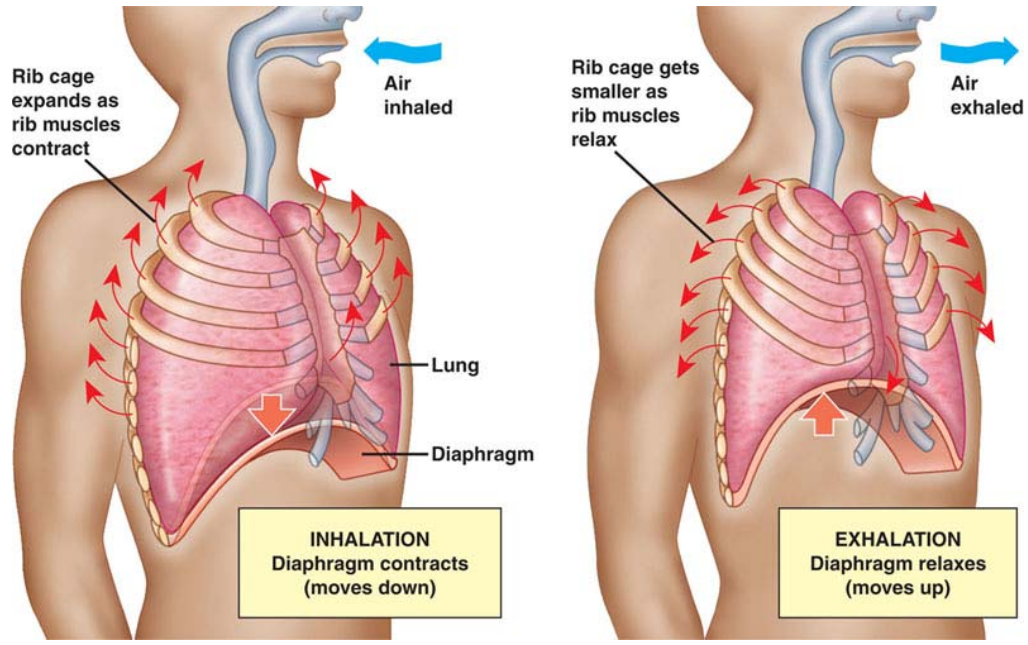

Figure 1.4 Mechanics of breathing [31]

B) Observation of respiratory organ motion

The respiratory organ motion in the thorax and abdomen has been quantified in numerous works [39-45]. Here, a brief overview is provided. Since respiration is mainly driven by the diaphragm, it typically shows a predominant superior-inferior motion of 10-30mm during quiet breathing in healthy subjects [39, 44, 45]. Seppenwoolde et al. [42] reported motion with average amplitude of 12mm for targets not attached to rigid structures in the lung. Weiss et al. [44] found 2.3-7.8mm motion for the heart and 0.9-7.0mm motion for the trachea. Brandner et al. [46] observed 1-25mm superior-inferior motion for the kidneys, and 13mm superior-inferior motion for the spleen. Even in the prostate, respiratory organ motion in the range of 1.0-10.2mm (average 3.3mm) was observed [47].

In the following section, there will be a focus on the liver and on biopsy procedure targets within the liver that is subject to extensive respiratory motion.

C) Respiratory liver motion

The shape of the liver is mainly determined by the surrounding structures such as the diaphragm and the lower ribs. Since the location of liver is directly below the diaphragm, it is strongly influenced by respiration [96]. Motion in the liver is generally not as pronounced as that of other organs, such as the heart. The main component of liver respiratory motion is a superior-inferior shift, typically in the range of 5-25mm for relaxed breathing, as quantified by a large number of works [39, 46-50, 52, 127, 128]. Besides, Rohlfing et al. [18] reported the liver additionally shows motion in anterior-posterior (1-12mm) and left-right direction (1-3mm). Zhang et al. [129] also discussed on the

deformation of the liver which can range from as low as 2mm to as high as 18mm in 3D positions. In addition, liver tumor, which is the target for biopsy or treatment, its motion during respiration was also qualified by Kitamura et al. [41]. It is worth mentioning that these results of quantification or qualification of liver motion were mostly from direct observation and measurement of the liver motion via high resolution CT or MR images acquired at different respiratory phase of the patients or subjects. Their results showed that the extent of tumor motion depends on the position in the liver to a certain degree; however, these factors are not sufficient to predict the motion of a target in the liver to ensure accurate delivery [33]. Therefore, patient-specific assessment of liver respiratory motion is highly recommended in clinical applications [51, 53-55].

1.2.3 Existing methods to handling respiratory organ motion in clinical practice

In this section, the existing methods for handling organ motion in clinical practice are discussed.

Before detailing specific methods to handling respiratory motion, the method for monitoring and detection of respiratory signals is outlined below. Typically, most commonly used methods can be divided into two categories: 1) internal-signal-based methods, which directly monitor structures, such as diaphragm, liver boundary, or internal landmarks inside the body [12, 18, 41-44], and 2) external-signal-based methods, which measure the displacement of the chest or the abdomen using external optical or electromagnetic markers and devices [14, 57-59].

A) Breath-holding

A straightforward approach to handle organ motion is to reduce the extent of breathing by instructing the patient to breathe shallowly [33]. This can be assisted by providing oxygen [60], or by applying gentle pressure on the abdomen using a belt [60], a cushion [61], or a compression plate [62, 63]. Except for the breathing reduction approaches, other methods that will completely interrupt breathing have been also applied in clinical practice. This can be achieved by voluntary breath-holding [5, 6], such as deep inspiration breath-hold (DIBH) method [64], or forced breath-holding, such as active breathing control (ABC) method [65, 66], with the use of special designed ABC devices.

However, holding their breath and following the respective instructions requires a considerable amount of cooperation on the part of the patient. Not surprisingly, some patients may have problems holding their breath for what is typically a period of 20 seconds or more.

B) Gating

Gating technology is more widely used in radiation therapy to deal with the respiratory motion problem [14, 20, 59, 79, 80, 89]. In gated-based treatment, the therapy beam is only turned on during a portion of the breathing cycle, for instance when the target is close to the exhalation position [33], to achieve high overall dose delivery accuracy.

However, controlling the needle for sampling is quite different to turning on or turning off the radiation therapy beam; the gating method is not, therefore,

very suitable in this case, unless the inserting of the needle is very fast, which always requires robotic arm assistance.

C) Tracking

When the target is moving, it is always desirable to keep the target in view throughout the breathing cycle. The aim of this kind of approach is to obtain a possibly static target in the needle's eye view without interrupting breathing. An obvious advantage of tracking is that it only requires minimal patient cooperation when compares to breath-holding. However, tracking a target requires great technical effort with three essential factors that are not necessary for breath-holding: needle adaptation (requires robotic arm assistance), prediction of target motion, and real-time motion compensation [10]. Unfortunately, the large technical gap has prevented tracking methods from being widely adopted in clinical practice so far.

D) Bio-feedback

Bio-feedback is a treatment technique that can be used to handle respiratory motion, in which patients are guided to gain more control of their breathing by using respiratory signals from their own bodies. It is often beneficial to provide visual feedback, which is displayed on a screen or via display goggles, to the patients who are able to comply, because this can strongly improve the regularity of breathing [13, 16, 67, 68].

Although bio-feedback has mostly led to more regular breathing, the reproducibility of respiratory motion is still low in some cases [69-71]. Additionally, it has to be emphasized again that the correlation between a respiratory signal and the internal target motion may not be stable [33]. Even

if a patient can achieve, for example, a perfectly reproducible skin motion with visual coaching, this cannot guarantee an accurate localization of a target inside the abdomen.

1.2.4 Related works for obtaining subject-specific respiratory motion

When moving organs are considered, a natural extension of static imaging is to acquire a series of time-resolved images, and thereby capture the temporal behavior of an organ [33]. In this section, related works for obtaining subject-specific respiratory motion using 4D imaging techniques are discussed.

A) Related works for the 4D image method on MR/CT datasets

Traditional 4D imaging techniques, such as 4D-CT and 4D-MRI, have been widely used to assess patient-specific breathing motion, mostly for determining individual safety margins in radiation therapy. However, there is no well-established and clinically available 4D-CT or 4D-MRI technique for radiation therapy, to the knowledge of the researchers, let alone for biopsy and ablation procedures. Several methods have been proposed, yet none have been implemented in the clinic, due to either insufficient image quality or excessive technical involvement.

Two main approaches have been taken in 4D-MRI development [72-78]: (1) to use fast 3D-MRI sequences to acquire real-time volumetric images (i.e., real-time 4D-MRI), and (2) to use fast 2D-MRI sequences to continuously acquire images from all respiratory phases and then retrospectively sort these images by respiratory phase (i.e., retrospective 4D-MRI).

The first approach is typically accomplished with parallel imaging and echo-sharing techniques. However, limitations with currently available hardware and software make it impossible to acquire high-resolution 4D image sets without significantly compromising image quality. Typical temporal resolution of real-time 4D-MRI is greater than 1 second, and typical voxel size is approximately 4mm [72, 73]. For example, Dinkel et al. used a 3D time-resolved MRI to demonstrate the difference of individual motion pattern of lung tumors [72]. The temporal resolution was 1.4 second and the voxel size was $3.1 \times 3.1 \times 1.4$ mm, in this study. This temporal resolution is inadequate compared to a typical human's breathing cycle of 4-5 seconds. Overall, the image quality of real-time 4D-MRI is low. The loss of image quality can be partially compensated for by co-registration with high quality reference images, but computational cost increases.

The second approach requires respiratory surrogate (either internal or external) to monitor patient motion during image acquisition. Compared to real-time 4D-MRI, the image quality is improved with this method [74-78, 81-84]. Remmert et al. demonstrated a retrospective 4D-MRI technique on a dynamic lung phantom, using an external signal for motion monitoring [74]. The pixel size was 2.7×2.7 mm at 10mm slice thickness. Von Siebenthal et al. developed a retrospective 4D-MRI technique using a navigator slice at a fixed position for motion monitoring [75]. All images were acquired in sagittal planes, and an alternating scheme was used to acquire data frames at all slice positions, interleafed with navigator frames, with an in-plane resolution of 1.8×1.8 mm and an out-of-plane resolution of 3-4mm. Disadvantages of this technique include the need for sequence modification and longer acquisition

time, as every other image is acquired purely for retrospective sorting purposes. Consequently, the complex nature of this technique is the major factor limiting its implementation in radiation therapy and biopsy or ablation procedure.

B) Related works for the 4D image method using Ultrasound

Inspired by the existing 4D MR techniques that aim at obtaining the respiratory organ motion, more and more researchers have realized similar technical concepts may be applied to US image. The concept of 'slice stacking' [81-84], for instance, has potential in the development of a robust, reliable, and clinically practical 4D US technique, in achieving both technical simplicity and sufficient image quality.

At present, the dedicated 3D US probe is still very expensive [94], and also has a limited field of view. Therefore, freehand [85] and mechanically-swept [86] 3D US systems are more cost-effective in image-guided interventions, and have been comprehensively studied by scientists [87]. Such a 3D US system firstly needs to be able to attach a position sensor to a 2D US probe, and then perform scanning by changing probe position and orientation, finally combining all the acquired 2D images with position information into a 3D US image [95]. This system is quite effective for imaging static targets. However, when the imaged targets (e.g., liver tumors) have noticeable motion and deformation caused by breathing, or other physiological processes, it will be quite challenging to create 3D US images to track the moving targets. This is because acquired 2D images often have different orientations and motion states, thus being unable to provide consistent information about organs when combined into a 3D US image. Therefore, motion-corrected/gated techniques

during image acquisition are required to make sure that the acquired 2D images have the same motion state, or that the created 3D images can capture the moving organ in any motion state. Here, 4D ultrasound imaging refers to a sequence of breathing-corrected 3D ultrasound images designed to capture the moving organs.

Up to now, there have been only a small number of literatures related to 4D US imaging. Nakamoto et al. [88] proposed a freehand 4D US imaging method, which uses a laparoscopic US probe and a magnetic position sensor together to acquire 2D images with position information, and create breathing-aligned 3D images. Wachinger et al. [89] combined a mechanically swept 3D US probe and a manifold learning based respiratory gating method to acquire respiration-corrected 3D US images.

C) Choice of image modality

Imaging is widely-performed at all stages of biopsy procedure, including pre-operative planning, intra-operative delivery, and post-operative verification. Previous section A) explored in detail the limitations of traditional 4D-MRI and 4D-CT image methods for biopsy study, which aimed at solving the respiratory motion problem. In one word, 4D-CT involves a high imaging dose being given to the patient due to the increased scan time [55, 69, 90], and respiratory organ motion during image acquisition can cause blurring, or reconstruction artifacts that are visible as false structures [33]; while 4D-MRI is expensive and not available for every patient. Neither image modalities are real-time. Consequently, traditional 4D-MRI or 4D-CT liver methods have significantly limited practical value in clinical applications – which require both time- and cost-effective, as well as absolutely accurate,

delivery for each patient. Conversely, US has excellent properties such as being safe, cheap, flexible, and non-invasive to the patient, and being particularly amenable to integration with other complicated medical (i.e. robotic-assisted) systems. The major concern regarding US imaging is its limitation in image quality, but technically, this could be improved in a variety of ways. Therefore, in this thesis, we will focus on the studying, exploring, and developing of new techniques based on the US image.

1.3 Objective and Structure of the Thesis

In this section, the motivation and objectives of this thesis are introduced. Since respiratory liver motion is a complicated and challenging issue to be solved, works should be done in multiple aspects, with connection to each other. Figure 1.5 shows the structure of the thesis. We divide the works into the following 3 aspects: 1) imaging processing; 2) phantom study; and 3) experimental study. The main goal of our work is to develop and evaluate new techniques covering these three aspects to improve biopsy efficiency and accuracy.

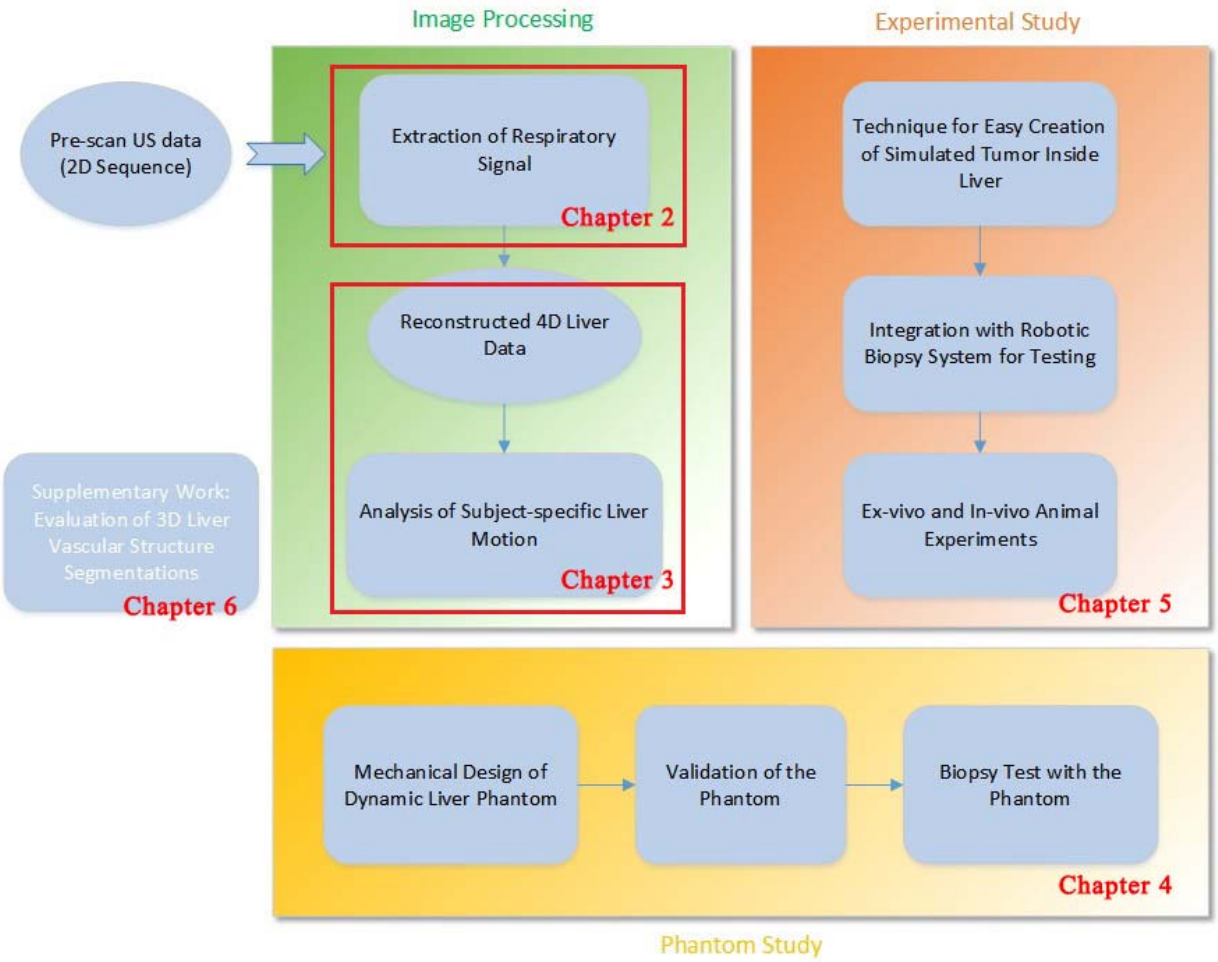

Figure 1.5 Structure of the thesis

Specifically, this work includes the following specific objectives:

1) To develop a novel respiratory signal extraction algorithm for liver motion phase identification, and to parameterize a 4D liver model.

2) To develop a novel subject-specific and respiration-corrected 4D US liver model for capturing and visualization of the liver motion during respiration. To perform motion analysis based on the 4D liver model, and help clinicians utilize this preoperative subject-specific motion information to improve diagnostic efficiency.

3) To design and validate a novel dynamic liver phantom for liver motion simulation, and therefore enable biopsy study on moving objects for the evaluation and assessment of the developing biopsy devices.

4) To develop a novel technique for easy creation of the simulated tumor inside porcine livers ex-vivo and in-vivo, to obtain ideal testing objects for US image-guided biopsy at low cost.

This thesis is organized as follows.

Chapter 1 introduces the background and specific aims of the thesis.

With the concept of fast and robust US image processing, Chapter 2 introduces a method which uses an adaptive template searching strategy to extract respiratory signal from 2D US image sequences. The effects of various template regions or searching regions on the accuracy of extracted signal are also discussed.

Chapter 3 illustrates the details of generating sequences of subject-specific and respiration-corrected 3D ultrasound images from multiple robotic-assisted-swept 2D US image sequences. The motion differences between subjects are quantitatively observed.

Chapter 4 describes the design concepts, and the mechanical design of a novel dynamic phantom, which consists of a linear servo actuator for respiratory motion generation, and an ultrasound-compatible compartment that can hold real porcine livers for testing. More importantly, the capability of the phantom for generating stable and repeatable movement cycles to simulate human respiration, and test the biopsy system, is verified.

To solve the commonly seen problem that ideal testing is hard to ensure in an experimental biopsy study, Chapter 5 presents a novel method to create simulated tumors inside porcine livers ex-vivo and in-vivo, for US image-guided biopsy. The performance of our proposed method is evaluated by comparing it to the more widely used approaches.

Chapter 6 describes a supplementary work, on quantitative evaluation of vascular segmentations in liver images. The significance of analysis of liver vessel structure to image-guided liver intervention procedures is discussed.

Finally, conclusions and recommendation for future work are summarized in Chapter 7.

CHAPTER 2. EXTRACTION OF RESPIRATORY SIGNAL FROM INTRA-OPERATIVE ULTRASOUND IMAGE

This Chapter introduces a method which uses an adaptive template searching strategy to extract respiratory signal from 2D US image sequences. The effects of various template regions or searching regions on the accuracy of extracted signal are also discussed.

*The following results were first published in: J Wu, **C Li**, S Huang, F Liu, BS Tan, LL Ooi, H Yu, J Liu, 'Fast and robust extraction of surrogate respiratory signal from intra-operative liver ultrasound images', International Journal of Computer Assisted Radiology and Surgery (IJCARS) 1-9, 2013*

2.1 Introduction

Image-guided and robot-assisted surgery and intervention are now widely applied in clinical applications to overcome limitations of traditional open and minimally invasive procedures. It plays an established role in complex surgeries, but its use in relatively simple procedures, such as biopsy, is conversely limited, because of high cost of surgical robot system and consumables, long set-up time, and absence of built-in intelligence. To address this issue, a new trend [91] in medical device is to develop simple image-guided, dedicated, and low-cost robotic systems for specific surgical and/or interventional procedures.

Enlightened by the success of the prostate robot [92], we are developing an US-guided robot to achieve quantitatively targeted liver tumor biopsy and ablation. However, it is challenging due to the movement and deformation of the liver soft tissue mainly caused by the respiration [93]. For liver motion compensation, a set of external or internal landmarks are always tracked as the surrogate of the respiratory pattern to either form the correlation with the true motion to be estimated, or be applied as input to drive the motion model. On the one hand, external landmarks, always placed on the abdomen or chest, are usually tracked using special optical or electromagnetic (EM) devices [102, 103]. These devices, however, create certain restrictions for surgical robots. For example, optical or magnetic obstruct along the optical or electromagnetic line-of-sight of these trackers is not allowed. On the other hand, internal landmarks, such as implanted fiducials [101], have issue of invasiveness, which may lead to infections or other complications. The superior-inferior (SI)

motion of the diaphragm is also a good indicator of the breathing signal [30, 97, 98], but the diaphragm does not always appear in the intra-operative US liver images.

To overcome these problems, and particularly, to further reduce the cost of our surgical robot, and make it noninvasive, simple and portable, we aim to identify the respiratory signals directly from intra-operative US liver images. In this Chapter, we first present an efficient and robust method for extracting the respiratory motion from intra-operative US liver images, and then evaluate the consistency between the identified respiratory motion and the motion of the skin landmark recorded by an EM tracker.

2.2 Adaptive Template Searching

The flowchart of our adaptive template searching (ATS) method is shown in Figure 2.1, which consists of 6 consecutive steps: 1) image acquisition, 2) video loading, 3) pre-processing (pre-filtering), 4) template region selection, 5) frame-by-frame template matching (registration), and 6) breathing signal extraction. In step 3), the image sequence is processed by a median filter (5×5 pixel) to smooth the speckles. In step 5), a frame-by-frame matching process, based on normalized cross correlation, is executed. Specifically, the template compares to various windows in the search region, starting from the top left, moving to the top right, and then going into the next row, and so on. Here, ‘adaptive searching’ refers to the methodology that the searching center on space of each frame is not fixed, but determined by the matching result of previous frame.

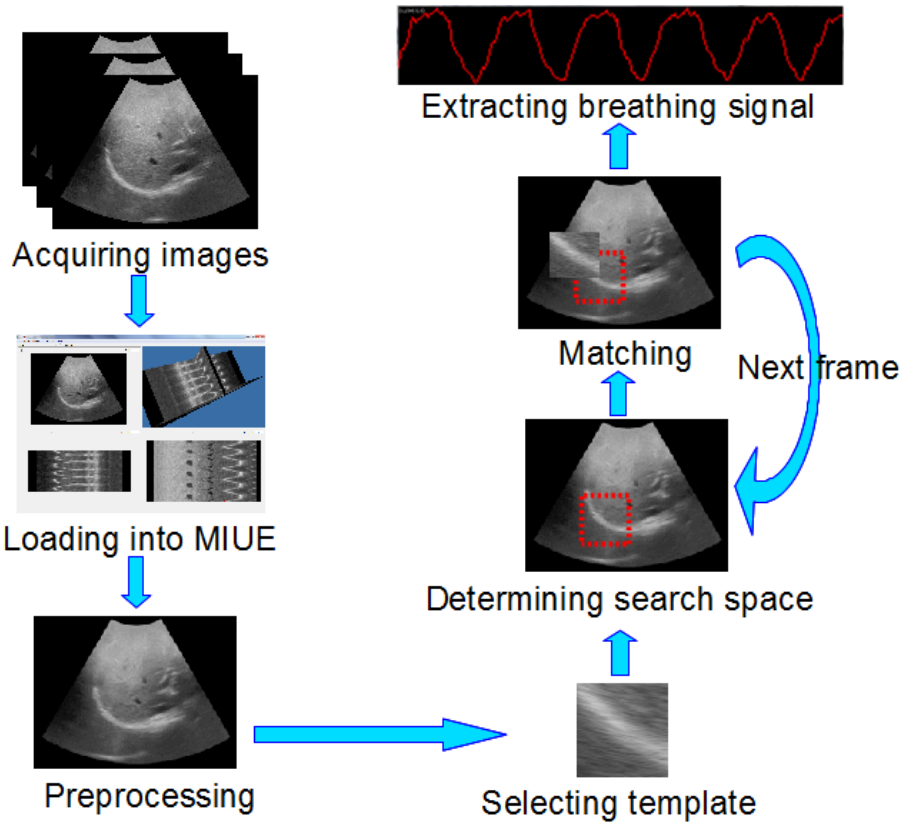

Figure 2.1 The flowchart of ATS. MIUE (Model-based Image Understanding Environment) is a customized imaging tool developed based on our in house software platform [114]

2.2.1 Noise reduction

Speckle-like noise, which is often seen in US images, disturbs the frame-by-frame matching process and leads to unstable matching results. A median filter (5×5 pixel) is firstly employed to process the image sequence before template matching. How this procedure improves the robustness and accuracy of the matching process will be demonstrated in the experiments.

2.2.2 Template region

The criterion for selection the template region in the US image is that this region should contain pronounced feature, such as liver boundaries or vessels, for robust matching. It is obvious that larger size of template region has

greater possibility to contain such pronounced feature; however, the computational cost becomes higher at the same time. Experiments on deciding appropriate template region size for robust and fast matching will be performed.

2.2.3 Similarity measurement

The intensity of dynamic liver US image may not change greatly for successive frames during respiration. Hence, in this study, the normalized cross correlation method [101] is a suitable choice as the image similarity metric of the matching procedure. This metric calculates pixel-wise cross correlation and divides it by the square root of the autocorrelation of the images [101]:

$$LC(A,B) = -\frac{1}{N}\frac{\sum_{i=1}^{N} A_i B_i}{\sqrt{\left(\sum_{i=1}^{N} A_i^2\right)\left(\sum_{i=1}^{N} B_i^2\right)}} \tag{2.1}$$

where A and B are the measured image or image region pair, and N is the number of pixels of an image or its sub-region.

2.2.4 Adaptive searching

To achieve efficient registration, a basic principle is to set the searching space as small as possible on the targeted image. Due to the quasi-periodic property of normal respiration, the liver tissue also moves in an approximately periodical way. Therefore, the liver tissue repeatedly appears in a relatively fixed extent (1-12mm [18]) in a normal or deep breathing cycle, such that the

searching space can be restricted in a neighborhood range of the template region. Traditional searching strategies (‘center-fixed’ searching) always fix the searching center at the center of the template region on each frame to be searched, aiming to find the optimum near the searching center. However, this searching strategy is very time-consuming.

Motivated by this, we present a new ‘adaptive searching’ strategy, which defines a series of small center-variant searching spaces in the frame-by-frame matching process. Specifically, the position of searching center of next frame is updated by the center of the template with best match of the current frame. This searching strategy makes use of the inter-frame dependency of the US image sequence, with the assumption that the motion of the liver tissue is small in two successive frames. Therefore, any specified image feature in the previous US frame should be found in a small neighbor region in the current US frame. Here, we call center-variant searching space as adaptive searching space, and the basic matching process using adaptive searching strategy is delineated in Figure 2.2.

When compared to center-fixed searching method, the adaptive searching method is usually faster, more robust, and with higher efficiency. In this study, the reference feature template (ground truth) is the template in the first frame and remains unchanged during the whole searching process, which means though the searching is adaptive, the search process can still find the optimal matching without accumulating the errors, because error accumulation only occurs when the matching template itself is adaptive. In other words, the center of the searching template will be updated on the next frame, but the

reference feature template will not be updated or replaced by the best match template on the current frame.

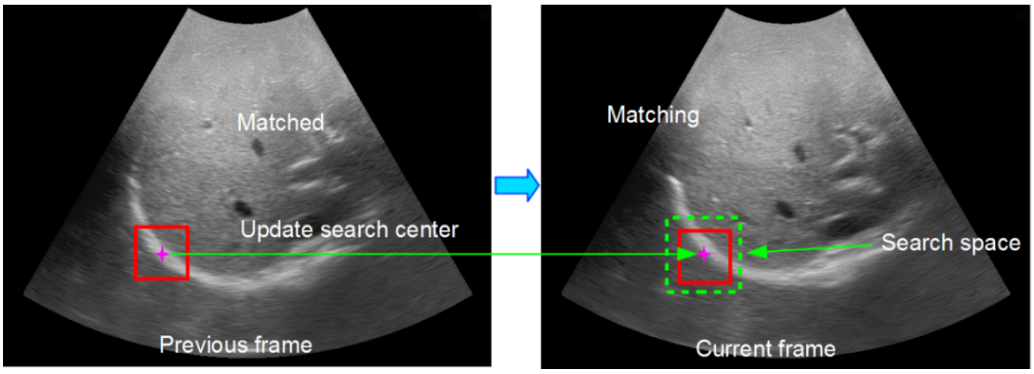

Figure 2.2 The adaptive searching strategy updates searching center on current frame, based on the matched result of previous frame. Due to the slow variation of the liver tissue on two successive frames, the searching space (dashed green square on the right subfigure) can be very small

2.3 Experiments

Figure 2.3 shows the experimental setup. The US imaging device used in this study is a Terason t3000 US system [139] with a 5C2 curve linear transducer (frequency 3.5 MHz). The 2D B-mode US image sequences (with image resolution of 640 × 480 pixels, pixel size of 0.37 × 0.37mm, and temporal resolution of 10 FPS) were obtained from four healthy volunteers, and each sequence contained 256 frames. All the experiments on extracting the respiratory motion in this study were performed on a Dell workstation with Intel Xeon CPU E5620 2.4 GHz and 12G RAM, and single-thread programming mode was used. In order to avoid the tremor of the probe by human hands, we designed a probe holder connecting to a robotic arm to hold this US probe as still as possible.

In order to validate the respiratory signals identified by our method, a NDI Aurora EM tracking system was used, to track an EM sensor placed on the umbilicus of the volunteers while acquiring the US images. Note that usually the EM sensor will not be put on the chest area, otherwise the signal obtained could be disturbed by the heartbeat of the subject. Instead, the anterior-posterior (AP) motion of the abdominal umbilicus was selected as reference respiratory motion for verification, because the umbilicus is usually a good position for placing an external marker to monitor the respiration, and is often adopted in respiratory motion modeling to obtain the surrogate breathing signals [28]. By using dynamic libraries provided by NDI and Terason vendors, we implemented a customized module in our software system to record the EM signals and US images to avoid large latency. Since the function to read the EM data executes extremely fast (far less than 1ms), the latency between each EM signal and US data was negligible. Finally, each US frame corresponds to an EM position.

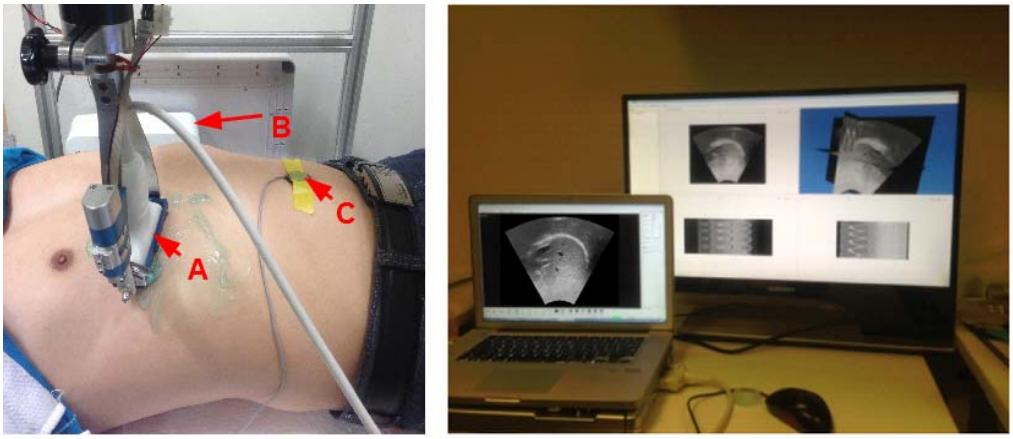

(a) US and EM tracking setup (b) Visualization for US images

Figure 2.3 Experimental setup. On the left side, A: US transducer with the probe holder for imaging; B: NDI Aurora EM tracking device; C: an EM sensor tracked by B. On the right side, the laptop belongs to a part of the

Terason US system, which is used for displaying the acquired images, which are simultaneously loaded into our MIUE framework on the bigger monitor

2.4 Results and Discussion

In this section, multiple sets of experiments performed are presented. These experiments were designed to analyze 1) the effect of noise reduction, 2) trade-off of the template region size, 3) the efficiency and robustness of the adaptive searching strategy, and 4) consistency validation, by visually and quantitatively compare the extracted respiratory motion from image sequence of 256 image frames, to the reference motion of the abdominal umbilicus tracked by the EM system.

2.4.1 Noise reduction

In this experiment, four image sequences from four different volunteers were used, the template region was fixed to 65×65 pixels, the adaptive searching space to 17×17 pixels, and the filter size was gradually increased to analyze the impact of filtering on the identified respiratory motion curves. The results were shown in Figure 2.4 (x-axis: time; y-axis: vertical displacement). The first row in Figure 2.4 displays four reference images, corresponding to the first image of each image sequence of four volunteers in turn. For each reference image, an exemplary region is selected as the matching template, labeled by a red square. The second row in Figure 2.4 shows four reference respiratory signals of the umbilicus, tracked by the EM system while acquiring these image sequences. The last three rows list the extracted respiratory motion curves from these image sequences without filtering, with a median filter of 5×5 or 9×9 pixels, respectively. The experiment results show that the

median filter can remove the speckle-like noise present in the US images, and make the frame-by-frame matching process more robust and accurate. Consequently, noise is removed from the respiratory motion curves, such that the entire profile of the motion curve is well preserved.

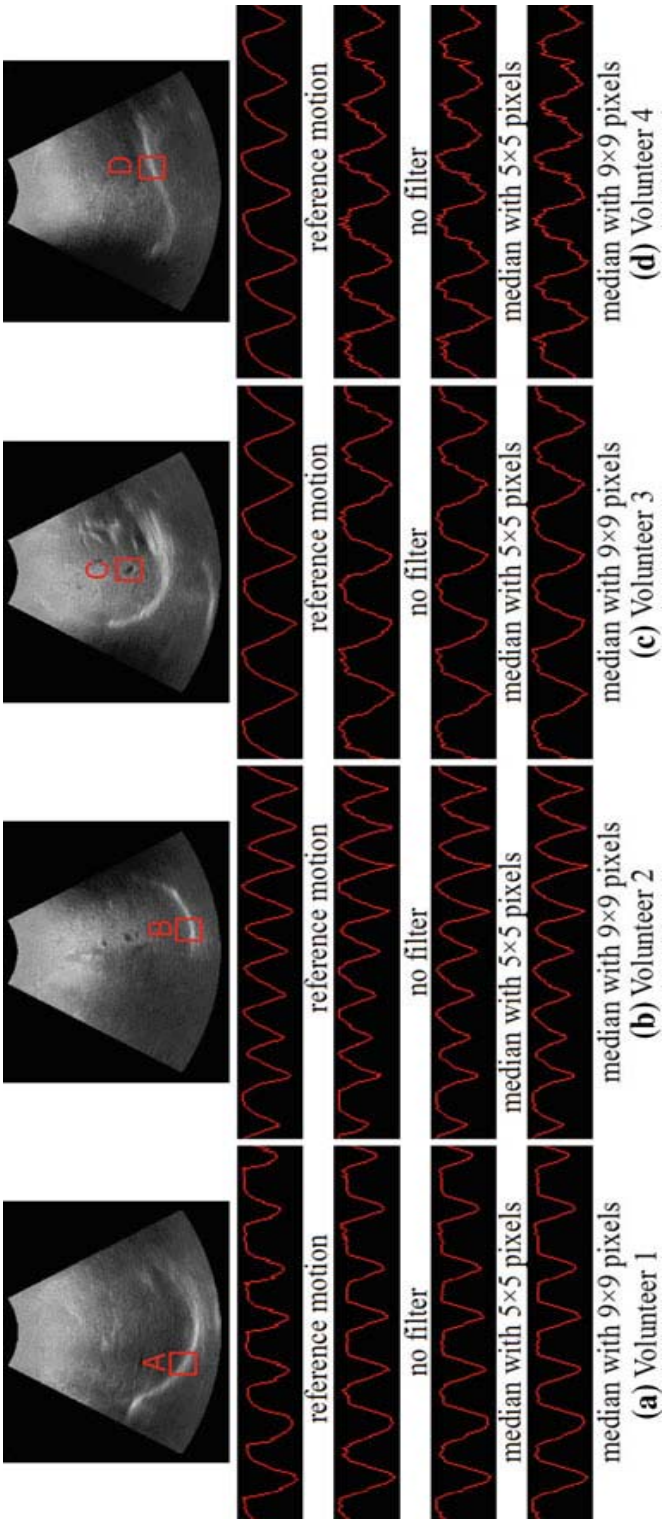

Figure 2.4 Experiment results of noise reduction. X-axis: time; y-axis: vertical displacement.

2.4.2 Template region

In order to demonstrate the effect of the template region size on the resulting respiratory motion curves, experiments were performed by gradually increasing the size of the template region, as displayed in Figure 2.5 (x-axis: time; y-axis: vertical displacement). For variable control, the filtering was not applied, and the size of the adaptive searching space was fixed as 17×17 pixels. Similarly, four exemplary template regions (A, B, C, and D) from the sequences of four volunteers respectively, were selected for analysis (the first row of Figure 2.5), using the template regions of which the sizes vary from 33×33 pixels to 129×129 pixels. It was observed that, using a template region of 33×33 pixels, the extracted motion curves are unstable with heavy noise and shape distortion (the third row of Figure 2.5), compared to the reference EM motion curves (the second row of Figure 2.5). When the template regions grow to 65×65, 97×97, and 129×129 pixels, these motion curves were found to have relatively low noise, and similar shapes to the reference curves (the last three rows of Figure 2.5).

The computation time on image sequence of 256 image frames for different template region sizes is listed in Table 2.1; it linearly increases with the pixel number (size) of the template region. For trade-off between stability and computation time, a template region of 65×65 pixels was found to be adequate. Therefore, in the other experiments detailed in this study, the sizes of the template regions will be fixed to 65×65 pixels.

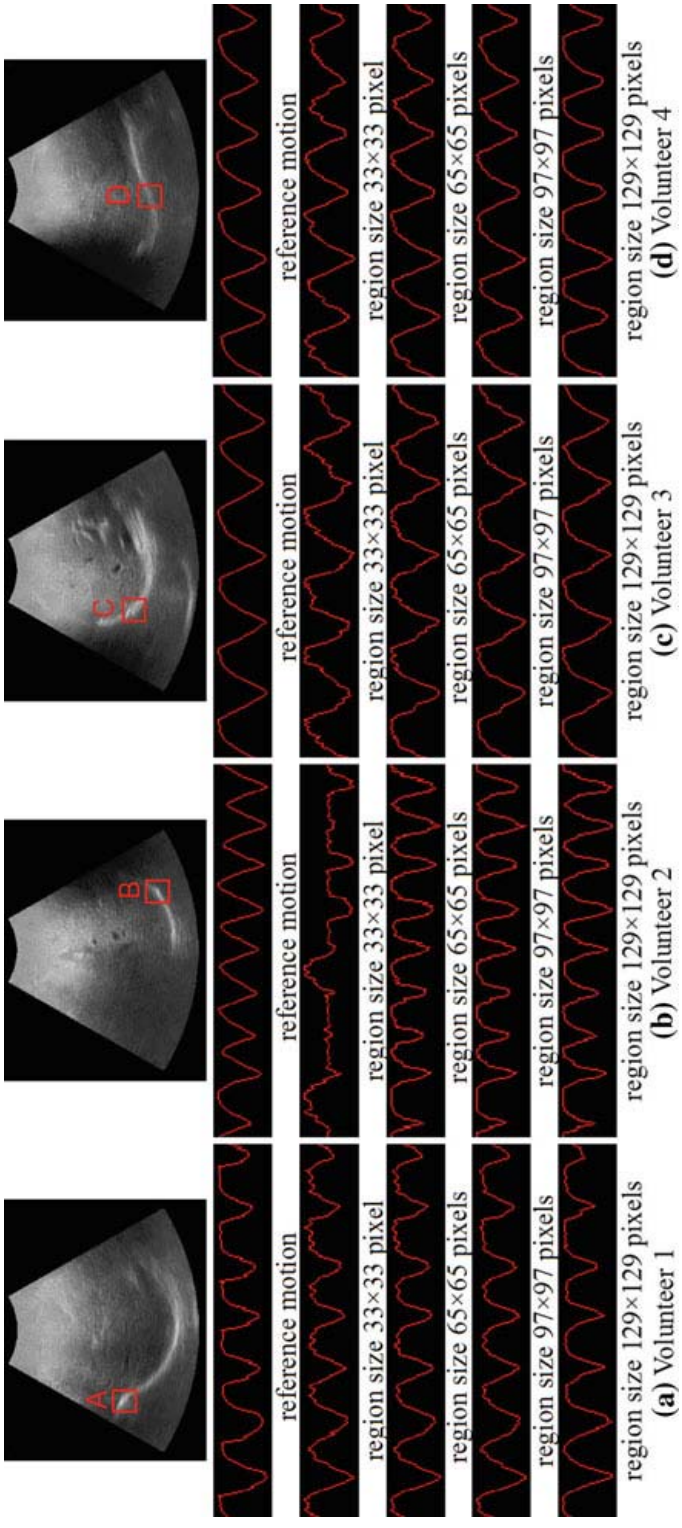

Figure 2.5 Experiment results of extracted respiratory motion curves use increasing template region sizes. X-axis: time; y-axis: vertical displacement.

Table 2.1 Computation time for different template region sizes. The image sequences and corresponding template regions are the same as in Figure 2.5.

Template region	Region size (searching time, in seconds)			
	33×33	65×65	97×97	129×129
A	1.33	5.17	11.50	20.37
B	1.33	5.15	11.53	20.26
C	1.32	5.10	11.41	20.05
D	1.33	5.24	11.63	20.38

2.4.3 Adaptive searching

A series of experiments was performed to test the efficiency and robustness of our adaptive searching method, in comparison with the traditional center-fixed searching strategy. For variable control, the filtering was not used, and the size of the template region was fixed as 65×65 pixels. The results were shown in Figure 2.6 (x-axis: time; y-axis: vertical displacement). Four typical template regions A, B, C, and D were manually selected from the image sequences of volunteer 1, 2, 3, and 4 respectively (the first row of Figure 2.6, labeled in red square). Based on the results of center-fixed searching, it would not be possible to obtain correct respiratory motion curves using the searching range of 33×33 or 65×65 pixels (the third and fourth rows of Figure 2.6). Only when the searching range is increased to 129 ×129 pixels (the fifth row of Figure 2.6), are correct respiratory motion curves available – however, this leads to a large computational cost. In contrast, use of the adaptive searching technique facilitates finding an optimal match in a much smaller searching range, usually a region of 17×17 pixels (the seventh row of Figure 2.6).

In addition, the computation time on image sequence of 256 image frames for the extracted respiratory motion curves in Figure 2.6 is listed in Table 2.2. In order to obtain satisfactory respiratory curves, using adaptive searching

strategy (17×17 pixels) can extract the curves in about 5 seconds for image sequence of 256 frames in Figure 2.6. On the other hand, requires about 300 seconds by using center-fixed searching strategy to get the satisfactory results as adaptive searching strategy. So a great speedup can be achieved using our proposed adaptive searching technique. In addition, the adaptive searching strategy leads to a relatively small searching range, making the matching process more robust, and consequently alleviating the noise present in the final motion curves.

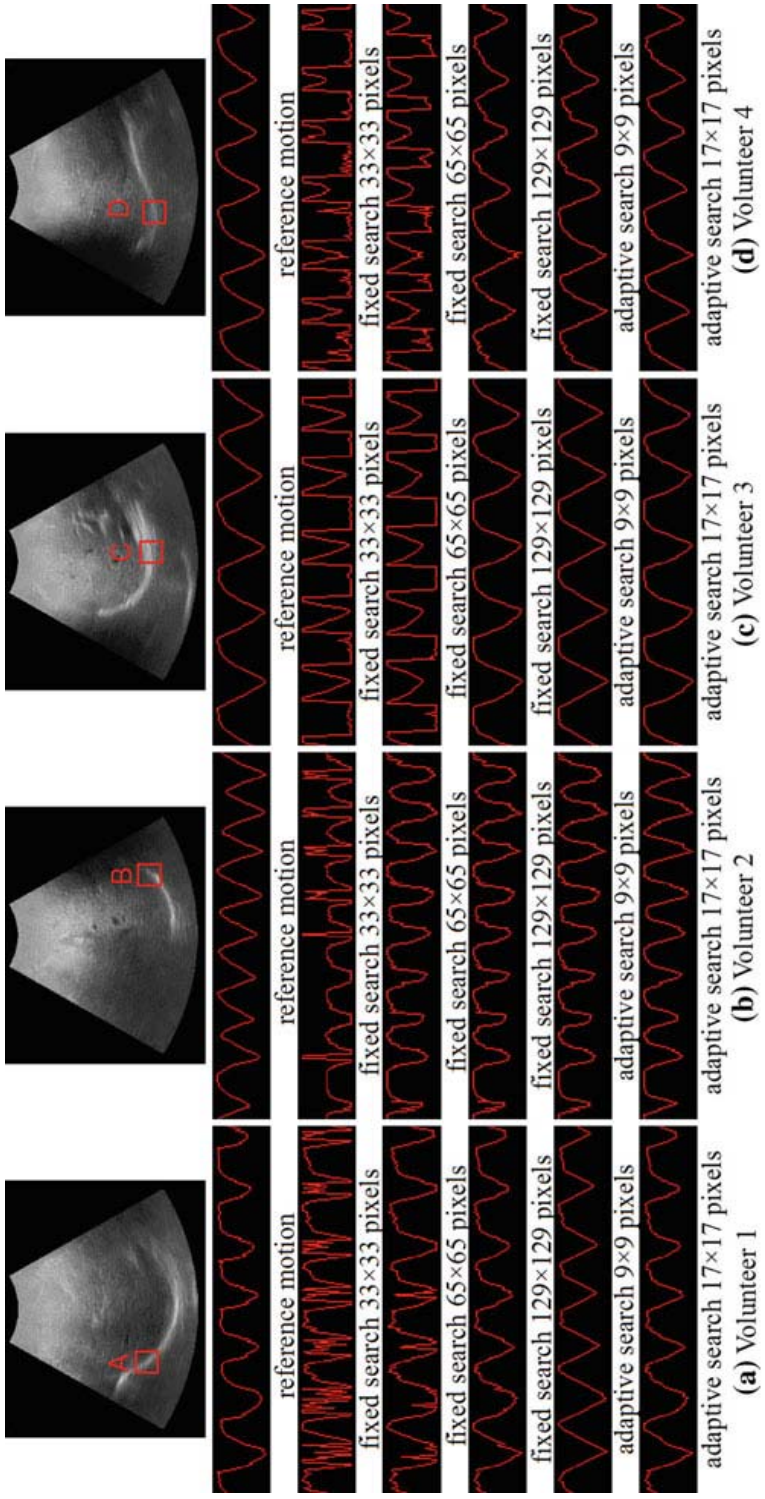

Figure 2.6 Experiment results of center-fixed searching strategy with increasing searching range (row 3-5), and adaptive searching strategy with smaller searching ranges (row 6-7). X-axis: time; y-axis: vertical displacement.

Table 2.2 Comparison of computation time for center-fixed searching strategy, and adaptive searching strategy. The image sequences and corresponding template regions are the same as in Figure 2.6.

Template region	Traditional (time, in seconds)			Adaptive (time, in seconds)	
	33×33	65×65	129×129	9×9	17×17
A	19.31	75.10	293.34	1.43	5.08
B	19.85	76.90	304.27	1.49	5.27
C	19.46	75.26	296.17	1.44	5.13
D	19.40	75.13	295.66	1.42	5.16

2.4.4 Consistency validation

In order to evaluate the accuracy of our method, three exemplary regions on each reference image of each volunteer's image sequence (the first row of Figure 2.7; x-axis: time; y-axis: vertical displacement) were selected as matching templates, and the identified motion curves (the second to fourth rows of Figure 2.7, in red) were visually compared to the reference motion tracked by EM device (in green). For better visual inspection, the identified curves were linearly scaled to have the same minimum and maximum as the EM reference curves.

In addition, the identified motion curves were also quantitatively compared with the reference motion curves, using a correlation coefficient (CC), which is listed in Table 2.3. As can be observed in Figure 2.7 and Table 2.3, the motion curves extracted from the liver boundaries and vessels (in red color) have nearly consistent respiratory phases with the reference curves (in green color), and the corresponding CC values are all greater than 0.9. The purpose

of plot the overlay of these two lines in this figure is to qualitatively show the overlap degree of the results and the reference. Higher overlap degree of these two lines suggests the identified respiratory signal is closer to that of the ground truth, and vice versa. Note that the amplitudes of both curves are slightly different, but they were normalized when overlaid, because I only focused on whether the phase changes of the identified signal can be synchronized with the EM sensor signal or not. The absolute amplitude changes were not observed here. In this study, I only focused on extracting 2D motion information from 2D US images, essentially 2D projection of the 3D liver motion. I put two lines together on the same figure only for comparing their similar respiratory phase changes. In addition, these high CC values prove that the translational motion of the liver boundaries and vessels are highly relevant to respiration, which reveals the potential to extract surrogate breathing signals from intra-operative US images, instead of tracking external landmarks. On the other hand, for other regions without pronounced features, the translational motion is difficult to detect. Therefore, the identified curves near these regions are heavily inconsistent with the reference curves, and the corresponding CC values are very small, at less than 0.2.

All the experiments above demonstrate that images of some areas of the liver, such as the liver boundary and vessels, carry more respiration-relevant information than others, and we can extract from intra-operative US liver images the surrogate respiratory signals, which is comparable to that determined by tracking the external landmarks. This observation supports our recommendation of removing extra tracking devices from our ongoing surgical robots, which is expected to be simple, portable and low-cost.

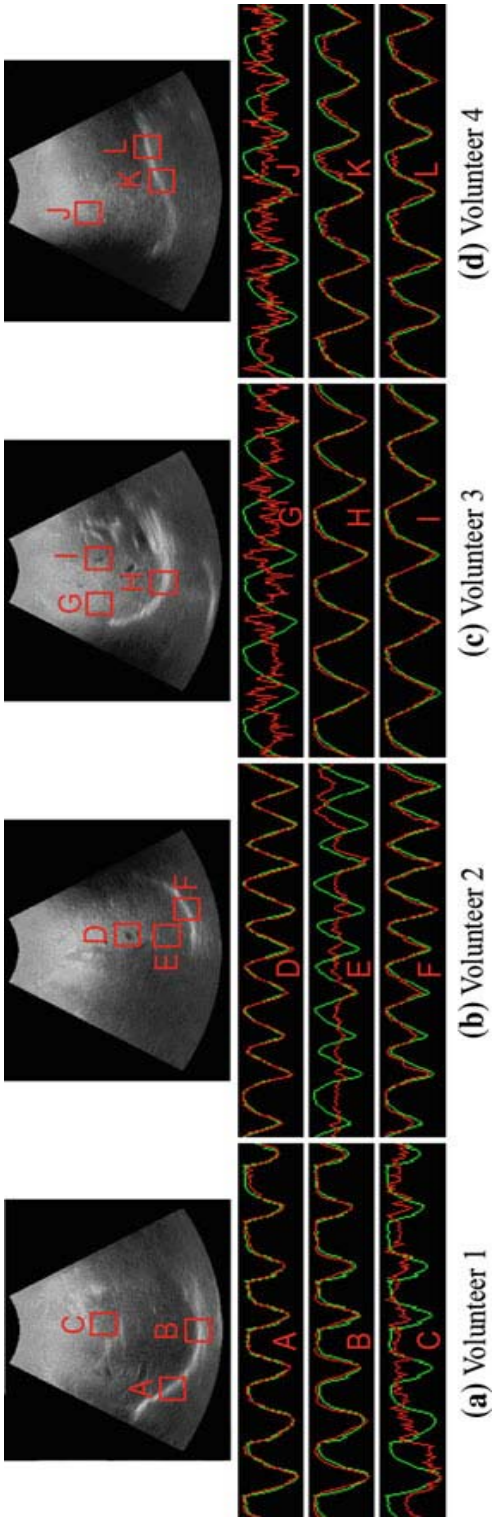

Figure 2.7 Visual and quantitative comparison between the identified motion curves (in red) and the EM-tracked reference motion (in green). The motion curves extracted near the liver boundaries (A, B, F, H, K, L) and vessels (D, I) highly approximate to the reference respiratory curves. X-axis: time; y-axis: vertical displacement.

Table 2.3 Consistency is quantitatively analyzed using the correlation coefficient (CC) metric. The image sequences and selected template regions are the same as in Figure 2.7.

	Volunteer 1			Volunteer 2		
Region	A	B	C	D	E	F
CC Value	0.9591	0.9415	0.1187	0.9701	0.0627	0.9379
	Volunteer 3			Volunteer 4		
Region	G	H	I	J	K	L
CC Value	0.1824	0.9714	0.9798	0.1715	0.9389	0.9107

It is worth mentioning that there are some existing feature-based ultrasound image processing approaches that can be compared with the proposed approach in this chapter. Here, several most recently published approaches, which are most related to our proposed approach, are listed in the following. Harris et al. proposed a feature-based method to track respiratory liver motion using 4D ultrasound [181], yet its performance was only assessed on relative short sequences, which poses a special challenge for this method to apply on long US sequences due to its iterative nature to accumulate errors, which has been identified as a significant drawback to US tracking at low volume rates and fixed searching region. De Luca et al. proposed a learning-based method for robust tracking in 2D ultrasound sequences for image guidance applications [182]. Their method was based on a scale-adaptive block-matching and temporal realignment driven by the image appearance learned from an initial training phase, and liver vessel tracking of 9 volunteers under free breathing was performed. However, the average processing time to track

vessel motion was about 100 ms per frame (range [30, 350] ms), and without learning process (training phase), the error of their results increased significantly when compared to our proposed method. In addition, Kubota et al. proposed a feature-based method for tracking organ motion on diagnostic ultrasound images, based on a large number of feature points controlled under a region of interest (ROI), and an error correction algorithm [183]. This proposed method was tested on the gallbladder of subject A and a liver vein in subject B under normal respiration, and a series of CC (correlation coefficient) values were calculated between the center of the tracked ROI and ground truth manually annotated by a clinician. The results showed that the CC curve on subject A was stable, however, on subject B was vibrated extensively, because the amounts of deformation or change in the cross-section position of the target on subject B were relatively larger than the size of the ROI, which means the results were greatly affected by selection of feature points and range of ROI. Furthermore, we have also looked into the feature-based processing method applied in the prostate surgery (prostatectomy). Abdouni et al. proposed a deformable tracking algorithm for monitoring the motion of the target volume on 2D US images based on Speeded-Up Robust Features (SURF), which were a series of salient points in this study [184]. However, this algorithm suffered from limitations, such as the results were also greatly based on the selection of feature points, which was quite unpredictable, and the calculation time was too large to be implemented in real-time. Finally, a recently published review paper (De Luca et al.) pointed out that the main challenge of feature tracking is to identify image structures that can be reliably tracked [185]. Weak echoes, poor SNR (Signal-to-noise Ratio), signal

dropouts, artifacts, and incomplete boundaries make this task especially difficult for US image tracking, yet only very few of published works have progressed to clinical practice. Our proposed method, being technically easy to be integrated to biopsy system with satisfying accuracy, is definitely capable of being applied to clinical practice when compared to existing methods.

The significance of applying the feature-based respiratory signal extraction algorithm is to achieve fast and accurate motion estimation in 2D US, and finally help the clinicians to locate the target in real-time. It is also quite useful to determine the breathing phase of the subject, such that building a subject-specific liver model becomes possible.

2.5 Limitations

The validation of this work was based on the results from EM sensor placed on the abdomen of the subjects, so it is true that we took only 1D result at one location as reference of this work, even though the movements of umbilicus position on the other two directions can be neglected when compared to the movement in the AP direction during human respiration [100, 112]. Since a strictly ground-truth respiratory signal is in general not available, we believe we will find better approaches to be applied as the reference in the future study. For example, acquiring data on our developing dynamic liver phantom (details in chapter 4) or other dynamic phantoms with known motions, and evaluate the accuracy of the proposed method.

2.6 Conclusion

A fast and robust method has been proposed to identify the respiratory motion of the liver based on 2D US image sequence. Using the adaptive searching strategy, the method is able to extract the respiratory signal from an image sequence of 256 image frames in 5 seconds. The experiments also demonstrate that our method can produce accurate and robust results, comparable to those of the EM tracking system. It will be of great help for the US-guided robot to have a build-in respiratory motion tracking system, resulting in more compact and flexible design at relatively low cost.

CHAPTER 3. SUBJECT-SPECIFIC AND RESPIRATION-CORRECTED 4D ULTRASOUND LIVER MODEL

This Chapter illustrates the details of a novel approach for generating sequences of subject-specific and respiration-corrected 3D ultrasound images from multiple robotic-assisted-swept 2D US image sequences, to help clinicians improve diagnostic efficiency. The motion differences between subjects are quantitatively observed.

The following work was accepted to be published in: ***C Li****, J Wu, J Wu, A Gogna, BS Tan, J Liu, H Yu, 'Subject-specific and Respiration-corrected 4D Liver Model from Real-time Ultrasound Image Sequences,' Computer Methods in Biomechanics and Biomedical Engineering.*

3.1 Introduction

Respiratory liver motion and deformation, which is mainly in the form of translation along the human SI (superior-inferior) axis [18, 19] is an inevitable issue in clinical practice for the treatment of liver tumors [20, 21]. Such motion causes difficulties in both imaging and locating the target (tumor) area and can even possibly fail the treatment. To overcome this problem and provide adequate information for clinicians, numerous research articles have been published over the years, on respiratory organ motion study, using 4D (i.e. 3D+time) liver models [18, 22-27, 102, 103]. However, these techniques all share the problem that establishing a 4D motion model (pre- or intra-operatively) using either MR or CT datasets is too time-consuming and costly [104], or make strong assumptions about the regularity of respiratory motion based on statistical data, and thus ignore the variations of the breathing pattern among different subjects or patients. Consequently, traditional 4D liver model methods have significant limitations regarding their practical value in clinical applications, which require both time- and cost-effective and absolutely accurate delivery, for each patient.

To bridge this gap, our technical motivation is to enable the transfer of clinically useful 4D liver information from MRI/CT to ultrasound, because ultrasound imaging is safe, cheap, flexible, non-invasive to the patient, and particularly attractive for integrating to other complicated medical (i.e. robotic-assisted) systems [95]. Considering the fact that a dedicated 3D ultrasound probe is still expensive and also has a limited field of view [87], freehand or robotic-assisted-swept 3D ultrasound [85, 86] seems a better

choice. With the addition of respiration-corrected techniques to ensure the acquired 2D images are at the same respiratory phase, the creation of a series of 3D images (4D ultrasound) that can capture the state of a moving organ during respiration is quite promising.

It is also worth mentioning that in clinical practice, techniques to physically or physiologically ease the breathing-induced liver motion issue in a 'straightforward' way, such as respiratory gating [105], anesthesia with jet ventilation [106], and – most widely-used – active breathing control (i.e. breathing holding) [107, 108], are often preferred and conventionally adopted [109]. Nevertheless, these methods either add extra cost or psychological burden to the patient, or are only suitable for the few patients who can actively cooperate. Concerning the breath-holding method, for example, it is too much to expect patients to hold their breath when examination is longer than 20 seconds [110, 111]. In these cases, treatment protocols that allow patients to breathe freely during the whole procedure are still desirable.

Motivated by both technical and clinical needs, we propose a novel method to build subject-specific 4D liver models solely from multiple robotic-assisted-swept 2D ultrasound image sequences in this study. The experimental results were evaluated by quantitative metrics. In addition, we analyzed the motion data from generated 4D models, to indicate the differences between subjects during respiration. With a prior knowledge of subject-specific liver motion in the free-breathing 4D model, the diagnostic efficiency and delivery of the treatment can be improved.

3.2 System Overview

The hardware system used in this study consisted of 1) an ultrasound (US) imaging system for image acquisition, 2) a robotic-assisted probe holder for scanning control, and 3) an electromagnetic (EM) tracking system for respiratory signal recording. Figure 3.1 shows the schematic diagram of the system overview.

The US imaging system used was Terason t3000 (Burlington, USA) [139] with a 5C2 curved transducer. The frequencies and focusing depth varied from 2.0 MHz to 5.0MHz and from 16 to 19cm, respectively. The US image resolution was 640 × 480 pixels, and the temporal resolution was about 10 FPS. The pixel size of the image was about 0.37 × 0.37mm when the focusing depth was 17 cm, and correspondingly varied under different depth settings.

In order to avoid the tremor of human hands, a robotic-assisted probe holder connected to a robotic arm was designed to clamp the probe and help to scan the liver with optimum stability, to acquire US images of different scanning angles under human respiration. The holder also guaranteed that the probe was applied with sufficient skin pressure to maintain the location and orientation of the US image. The expected scanning angles were actuated by a geared motor (Faulhaber DC-Micromotor 0615, Schönaich, Germany), and recorded by an encoder embedded in the motor. The motor was connected to a computer using Ethernet (via a network cable). The tilting was capable of covering an angle of up to 86º. The remote center-of-motion (RCM) for tilt was placed at the surface of the US transducer.

An NDI (Ontario, Canada) Aurora Electromagnetic (EM) tracking system was used to track an EM sensor placed on the umbilicus of the volunteers, because researches have shown that the motion of sensors attached to human abdomen and that of inner organs, such as liver, are greatly correlated – thus internal liver motion can be evaluated using a skin surrogate motion signal [100, 112]. In addition, De Groote et al. [113] placed tracking markers on the abdomen and found that the largest abdominal skin displacement was at the umbilicus. Therefore, in this study, we put the EM sensor at this particular anatomical position. The dominant motion direction of the tracked sensor on the umbilicus was applied as the ground truth respiratory signal, to indentify the respiratory phase of the subject, and further provide valid reference for clinicians to manually annotate the liver boundary or landmarks on the US image sequences.

For the software system, a customized imaging tool was developed based on our in house software platform MIUE [114]. Through this tool, the operator can send commands to drive the motor to tilt the US probe at a predefined angular interval to sweep the liver region. For each scanning angle, an image sequence is acquired to cover several breathing cycles. Since the scanning can be precisely controlled, the relative position and orientation of each 2D image sequence can be known accurately, which is used for 3D image reconstruction from 2D image sequences in a group-wise strategy.

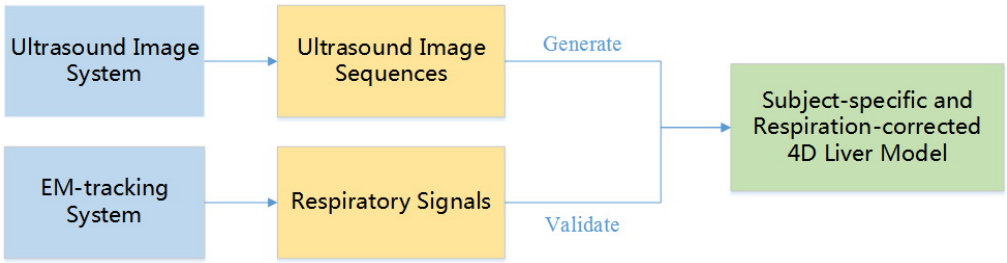

Figure 3.1 Schematic diagram of system overview

3.3 Experimental Setup

Four healthy volunteers (average age 33, with normal BMI: Body Mass Index, Table 3.1) were recruited for the experiments. The volunteers were asked to lie on a bench bed in the supine position (Figure 3.2) in a quiet room. Soft pillows were prepared for the comfort of the volunteers. Each volunteer was given enough time to calm down and breathe calmly before image acquisition.

Table 3.1 Profile of four volunteers.

Subject Number	Gender	Age	Weight/Kg	Height/cm	BMI
1	M	27	72	172	24
2	M	32	65	168	23
3	M	25	75	182	23
4	M	49	61	168	22

At the beginning of the experiment, the US probe was covered in ultrasound gel and held by the clinician to flexibly scan the liver at inter-rib intervals of the right chest to refrain from obstruction of ribs, so that clear images of the liver boundaries and/or vessels could be observed. Then, the US probe was

mounted onto the probe holder with its position and orientation close to that previously selected manually, and ultrasound images were acquired by robotically scanning the livers of the volunteers as predescribed. For each volunteer, p = 48 image sequences were acquired by regularly tilting the US probe with a total angle of 30.84˚ and a total acquisition time of about 8-9 minutes. Each image sequence contained 128 frame images, and approximately lasted 3-4 respiratory cycles. All the acquired US images and corresponding EM positioning data were transferred to the computer for further analysis.

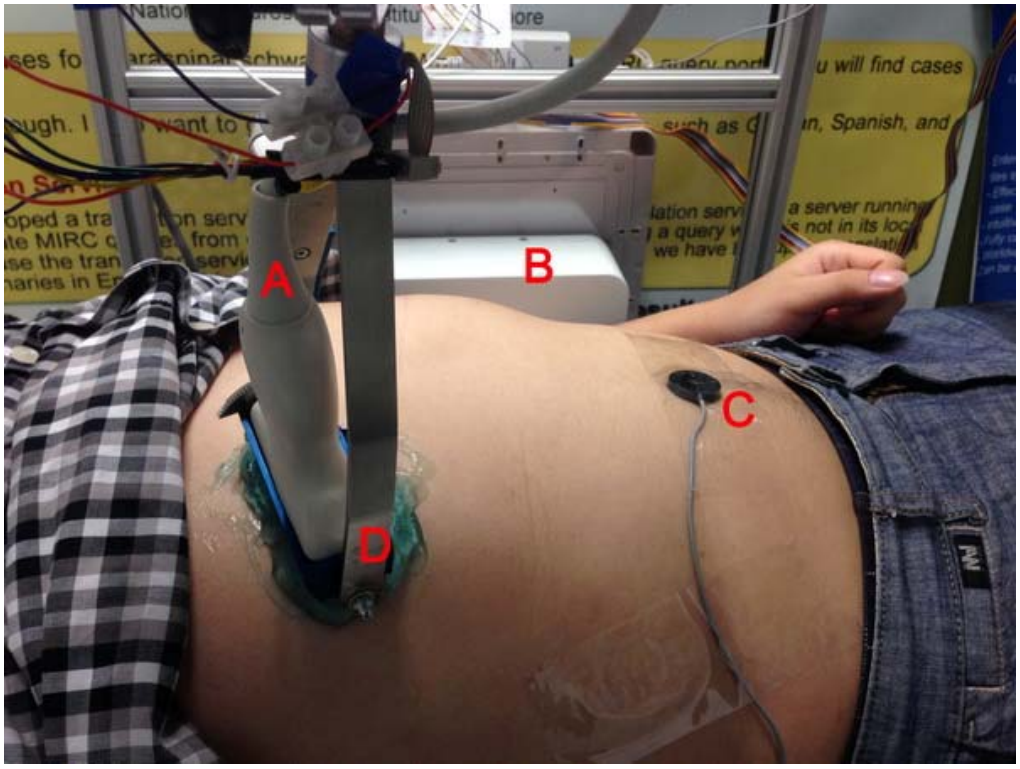

Figure 3.2 Experimental setup. A: 2D US probe; B: NDI EM tracking device; C: EM sensor on the umbilicus of volunteer tracked by B; D: Probe holder.

3.4 Generation of the Liver Model

The processing flow chart of generating the liver model from the real-time ultrasound image is shown in Figure 3.3. The basic idea is to detect the specific respiratory phase of a series of 2D images from multiple 2D image sequences with different scanning angle, and then combine these detected 2D images into a respiration-corrected 3D image, which captures the moving liver at a specific breathing phase, ranging from end of expiration (*EE*) to end of inspiration (*EI*) [116]. The assumption made in this approach is that the physiological motion of the liver is smooth over time; thus, in theory, each reconstructed 3D US image captures the shape of the liver at a specific breathing phase. For a more detailed description and explanation of the respiratory signal detection, please refer to our previous works [115, 116].

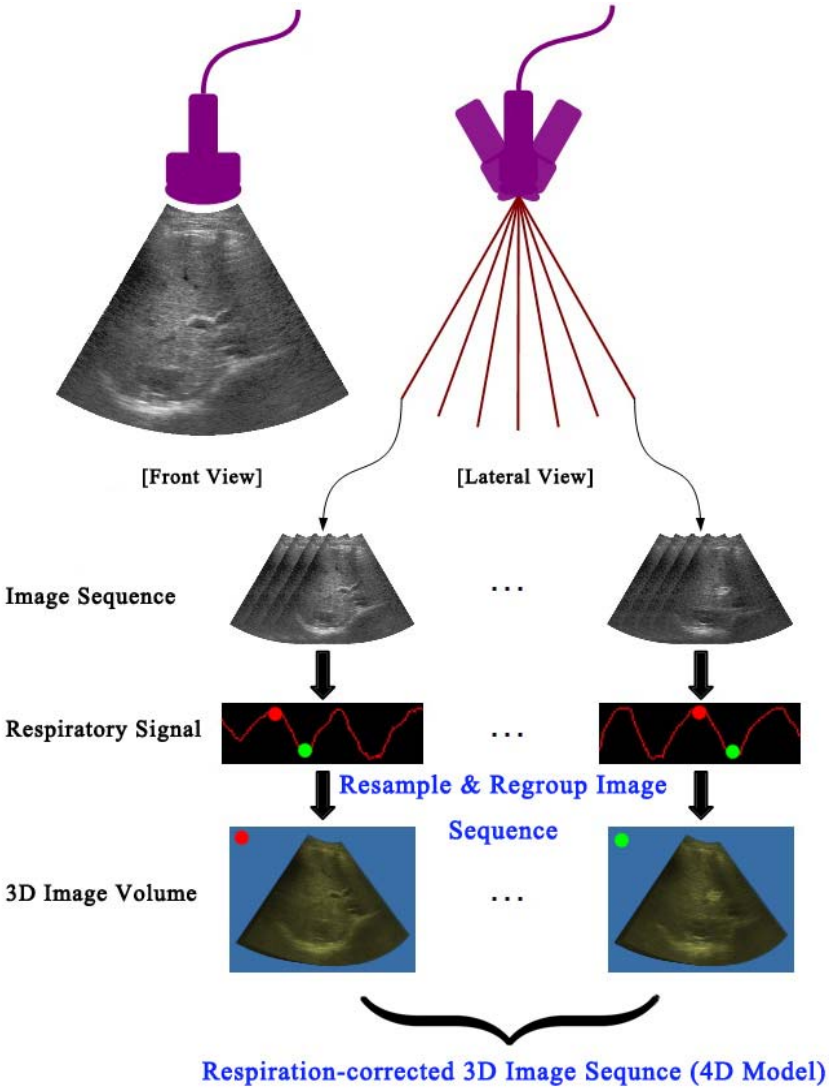

Figure 3.3 Overall processing flow of 4D ultrasound imaging using a 2D ultrasound probe, and a robotic arm enabling tilt-scanning of the probe. A series of 3D images is created to capture the moving liver from EE to EI.

We assumed that each of 2D image sequences (S_i) was acquired at a specific scanning angle θ_i . In total I = 48 2D image sequences were acquired. We firstly detected and extracted the respiratory signal from each frame of S_i [115, 116]. The extracted respiratory signal was 1-dimensional, representing the principal pattern of the liver motion within the US imaging plane. In particular, all *EE* and *EI* frames could be found by calculating the local maximums and minimums within the extracted respiratory signal.

Although human respiration is generally quasi-periodic, *all EEs and EIs* found in the detected respiratory signals still showed relatively great differences due to differences in breathing depth. In order to create a smooth 3D image sequence covering a half respiratory cycle, we searched successive *EE* and *EI* pairs, and labeled one pair EE_i and EI_i, which was closest to the averages of the detected *EEs* and *EIs*. In terms of calculation, the time point (i.e. frame number) at which detected *EEs* or *EIs* occur was used, quantified as a delay from a specific reference time point, which is the first frame of the image sequence (frame 1). The corresponding formulation is described as follow:

$$\left(EE_i, EI_i\right) = \left(EE_m, EI_m\right) if \left(\left|EE_m - EI_m\right| - \frac{1}{M}\sum_{j=1}^{M}\left|EE_j - EI_j\right| \right) is \min, \left(m \in M\right) \tag{3.1}$$

where M is the total number of successive *EE* and *EI* pairs in S_i.

For each S_i, and a corresponding pair of *EEi* and *EIi*, an image sub-sequence between *EEi* and *EIi* was selected out. *K* frames of images were resampled in this image sub-sequence in a linear interpolation way (K = 8 in this study). Then, the images at the same respiratory phase were regrouped into a new respiration-corrected image sequence (T_k = {T_1, T_2, … T_8}) according to their initial scanning angles from all the 48 sub-sequences. In other word, a total number of $I \times K = 48 \times 8 = 384$ images were regrouped in this step. Note each T_k contains 48 respiration-corrected images corresponding to 48 initial scanning angles at the time point *k*.

Finally, we reconstructed each aligned image sequence (T_k) into a 3D image volume (V_k). Therefore, each V_k captured the shape of the liver at a specific

respiratory phase between *EE* and *EI*. Since the aligned images were acquired by regularly tilting the US probe, the reconstructed 3D image V_k contained a fan-shaped volume.

3.5 Evaluation

Since the dynamic 3D (4D) liver model was generated from the respiration-corrected 2D image sequences as described in the previous section, the evaluation was performed on randomly selected 2D image planes for efficiency of calculation. Theoretically, taking any of the scanning angle θ_i, and the relative 2D scanning plane P_i, which is the initial scanning plane at angle θ_i, and same as the scanning plane of S_i, as a reference, the cross-section of the specific structures (boundary/landmarks) of the dynamic 3D liver model on P_i should match the relative trajectories of the original 2D image sequence S_i. The matching error caused by linear interpolation and selection of *EE/EI* pairs when generating the liver model will be quantitatively evaluated.

For any 2D plane that was selected for evaluation, a coordinate system fixed on the center of the ultrasound image was established, as demonstrated in Figure 3.4. Let 2D images sequence Q_{ij} denote the cross-section of the dynamic 3D (4D) liver model on a randomly selected scanning plane at angle θ_i of subject *j*, in total $i = 3$ image sequences were randomly selected for each subject. Each Q_{ij} will be compared with its relative S_{ij}.

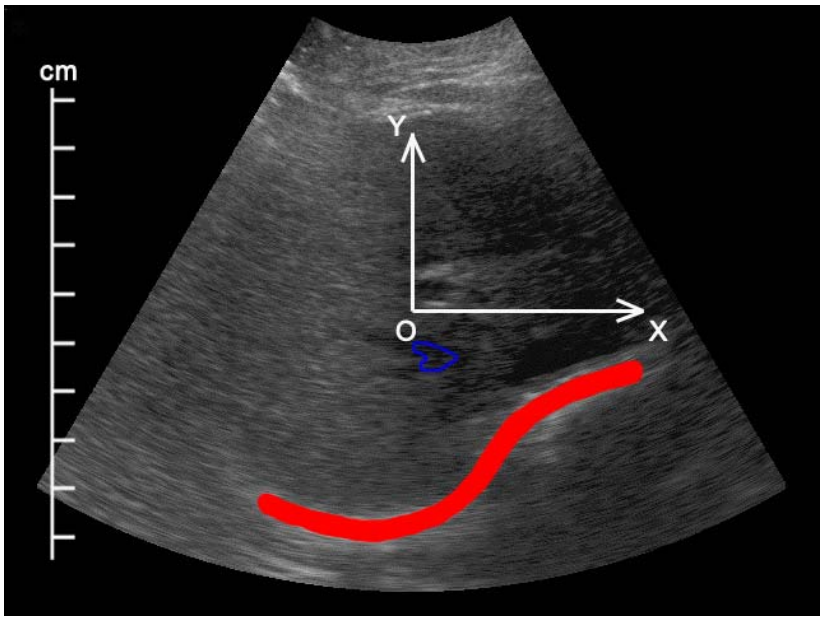

Figure 3.4 Establishment of the coordinate system on the 2D ultrasound image plane, and manual annotation of liver boundary (in red color) and an internal landmark (in blue color).

3.5.1 Manual annotations

Based on the replay of each selected US image sequence S_{ij} and relative signal from the EM tracking sensor, one clinician manually annotated (1) first frame (I_{EE}) of a half respiratory cycle on S_{ij}; (2) last frame (I_{EI}) of a half respiratory cycle on S_{ij}; (3) the area of liver boundary (B_{ij1}) on I_{EE}; and (4) the area of liver boundary (B_{ij2}) on I_{EI}. On the other hand, the clinician also annotated the areas of liver boundary C_{ij1} and C_{ij2}, on the first and last frames of Q_{ij}, respectively (Figure 3.4).

In addition, the clinician indicated a total of two well-defined in-plane anatomical landmarks, such as bifurcations of vessels in the liver, for each subject, in the first frames of Q_{ij} and relative S_{ij}, (Figure 3.4). Three engineers experienced in ultrasound imaging research manually annotated the rest of the landmarks in the remaining frames of S_{ij}, using the annotation done by the

clinician in the first frame as an aid. Note that the clinician and all engineers were asked to use a brush tool with width of 20 pixels during the manually annotation of the liver boundary for the calculation of the overlap ratio. Finally, the clinician reviewed the results to ensure anatomical accuracy. The MIUE platform [114] was used for the manual annotations. The positions of relative landmarks on Q_{ij}, were automatically obtained using the same method [115, 116], based on the annotation from the clinician in the first frame of Q_{ij},.

3.5.2 Evaluation measures

The identified liver boundaries were used for consistent validation of the generated liver model during a half respiratory cycle. All the annotated B_{ij1} and B_{ij2} were taken as ground truth. All the C_{ij1} and C_{ij2} were quantitatively compared with relative B_{ij1} and B_{ij2} by calculating the overlap ratio defined within the [0.5, 1] interval. The extreme values 0.5 and 1 denote the worst case where two boundaries can not match at all, and the best case where two boundaries can match perfectly, respectively.

$$O_{ij} = \frac{\#\left(B_{ij} \cap C_{ij} + \frac{1}{2}\left(\left(B_{ij} \setminus C_{ij}\right) + \left(C_{ij} \setminus B_{ij}\right)\right)\right)}{\#\left(B_{ij} \cup C_{ij}\right)} \tag{3.2}$$

where # denotes the number of pixels, and \ is the minus operator. For example, A\B is the set of all object pixels belonging to A but not B.

The pinpointed landmarks were used to evaluate the accuracy of the generated liver model. Let L_{nkt} denote the position of the landmark n at frame t of its relative sequence placed by engineer k, and M_{nt} denote the position of

the relative landmark on Q_{ij}. The mean $L_{nt} = \frac{1}{k}\sum_{i=1}^{k} L_{nti}$ of the k = 3 engineers was taken as a gold standard. The overall distance error of landmark n was calculated as follows:

$$L_n = \frac{1}{t}\sum_{i=1}^{t} \left| L_{ni} - M_{ni} \right| \tag{3.3}$$

The standard deviation was also calculated

$$\sigma_n = \left(\frac{1}{t}\sum_{i=1}^{t} \left| L_{ni} - M_{ni} - L_n \right|^2 \right)^{1/2} \tag{3.4}$$

We took into account that the landmark trajectories between engineers could be significantly different in some cases, especially when the landmark area was affected by noise and was therefore not very clear. To measure the inter-observer variability, we defined a function

$$IO_n = \left(\frac{1}{kt}\sum_{i=1}^{t}\sum_{j=1}^{k} \left| L_{ni} - L_{nij} \right|^2 \right)^{1/2} \tag{3.5}$$

If a landmark moved out of the field of view, those frames were omitted from evaluation.

3.6 Motion Analysis

In clinical practice, liver interventions such as biopsy and ablation have always been guided by intra-operative 2D US images in real-time, so it is important to analyze the motion of the liver boundary and internal landmarks

in the specific 2D US image plane, and also to compare the individual differences between subjects, to provide clinicians with useful pre-operative information.

Since the coverage range of the fan-shaped scan could vary slightly between each subject, we chose to use the same 2D plane P_r, which can be found and uniquely identified in each subject's one of forty-eight scanning plane P_i, as the reference plane. Specifically, P_r was perpendicular to the coronal plane of the subject. When the probe sweeps the fan-shape area, there is a moment (at scanning angle r) that the probe is perpendicular to the coronal plane of the subject, and this probe plane is P_r. Actually P_r is perpendicular but not necessarily orthogonal to the coronal plane. Similarly, manual annotation of the liver boundary and one internal landmark for each subject were ascertained by the clinician and three engineers on the P_r, during a half respiratory cycle.

After annotation, it is possible to measure the magnitude, degree, and direction of displacement of the liver boundary, as well as displacement of the internal landmarks. Specifically, the displacement, velocity, and acceleration of the liver boundary and internal landmarks on the P_r of each subject were calculated to show the physiological change during a half respiratory cycle.

3.7 Results

3.7.1 4D liver model

Three 3D volumes of the generated liver model of subject 1, at three different respiratory phases (*EE*, *EI*, and the middle phase between them), are shown in Figure 3.5. From this figure, the dynamic changes of the respiration-

corrected model at different respiratory phases can be observed. For each volume, three orthogonal views of the US image are also shown for visual comparison.

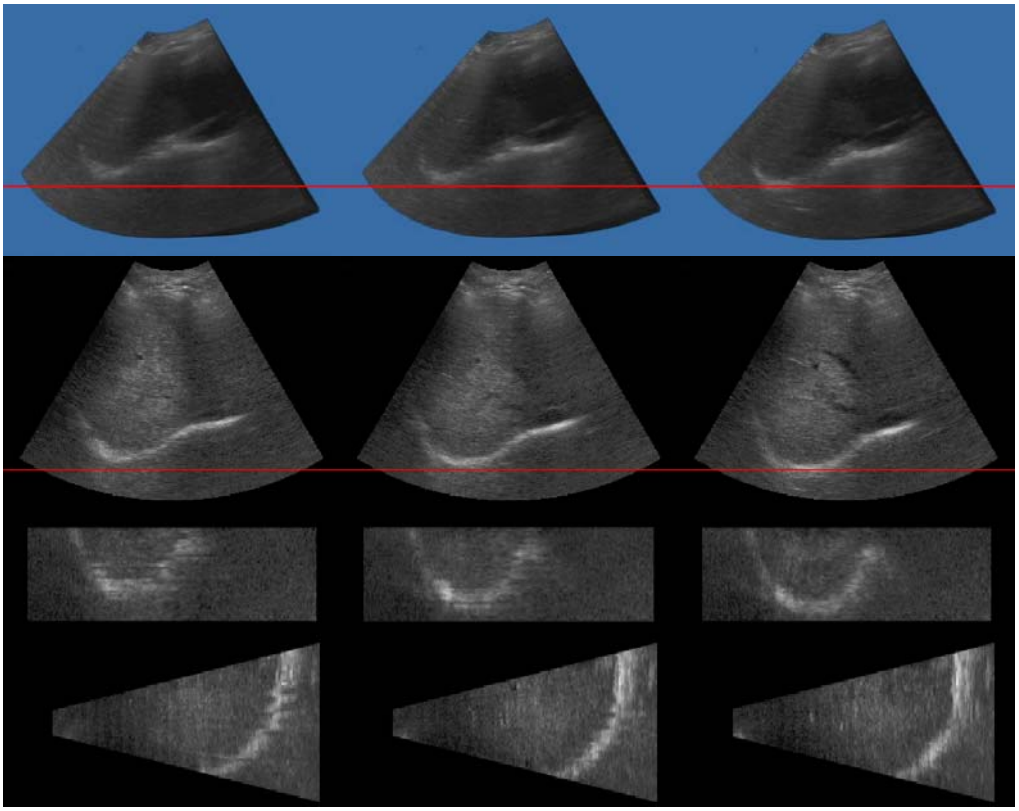

Figure 3.5 Three volumes are reconstructed at three different respiratory phases (left: EE, middle: Middle phase, right: EI). Three orthogonal views of the US volumes are shown

3.7.2 Accuracy of the liver model

Table 3.2 shows the results of the overlap ratios O_{ij1} and O_{ij2} of the liver boundary at *EE* frame and *EI* frame of a half respiratory cycle, respectively. The values of O_{ij1} and O_{ij2} ranged from 0.81 to 0.95, and 0.77 to 0.94, and the mean values of O_{ij1} and O_{ij2} were 0.90 and 0.89, respectively.

For each landmark, time points t = 8, and in total N = 8 landmarks (two for each subject) were indicated by the clinician in 16 selected image sequences

for the four subjects and calculated in equation (3.3). Table 3.3 shows the results of measures of the pinpointed landmarks, and relative inter-observer errors for each subject. The mean values of L_n and I_{On} were 2.44 and 0.40, respectively. The standard deviations of eight landmarks ranged from 0.32 to 0.66.

Figure 3.6 shows the individual landmark trajectories manually annotated by the three engineers, for four landmarks (n = 1, 3, 5, 7) in a half respiratory cycle. Three different colors represent the annotations of the three engineers. From this figure, we can see that the differences between the engineers can not be neglected.

Table 3.2 Overlap of liver boundary at EE and EI of half respiratory cycle.

Subject (j)	1			2		
Image seq *(i)*	1	2	3	1	2	3
O_{ij1} *(EE)*	0.90	0.85	0.92	0.86	0.94	0.93
O_{ij2} *(EI)*	0.93	0.88	0.87	0.89	0.90	0.93
Subject (j)	3			4		
Image seq *(i)*	1	2	3	1	2	3
O_{ij1} *(EE)*	0.88	0.95	0.92	0.91	0.81	0.87
O_{ij2} *(EI)*	0.82	0.91	0.94	0.89	0.77	0.89

Table 3.3 Matching error of eight landmarks.

Subject (j)	1		2		3		4	
Landmark (n)	1	2	3	4	5	6	7	8
L_n (mm)	2.38	2.76	2.42	2.25	2.78	3.20	1.68	2.06

IO_n (mm)	0.31	0.64	0.27	0.50	0.44	0.36	0.31	0.33
σ_n	0.54	0.50	0.49	0.61	0.65	0.66	0.47	0.32

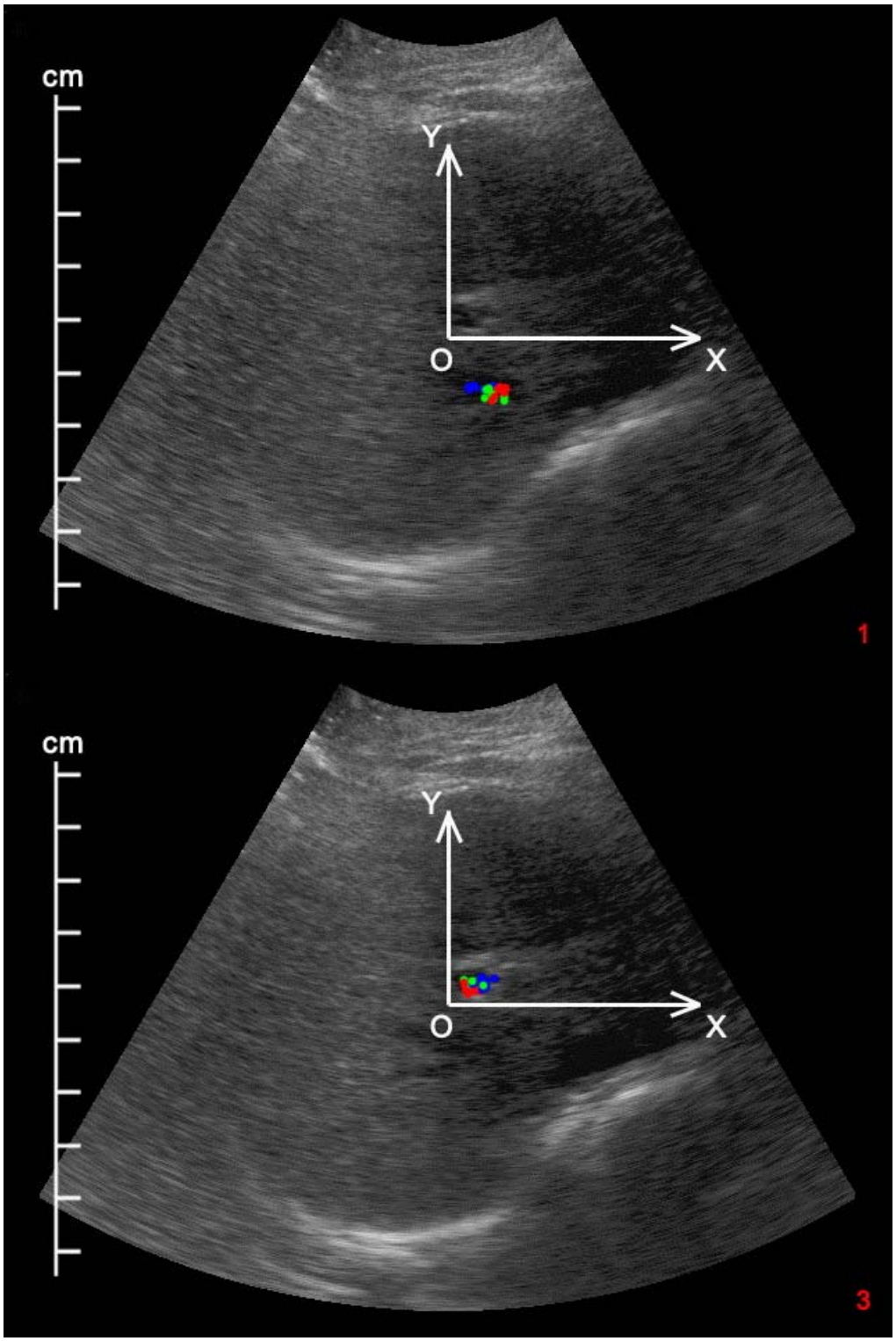

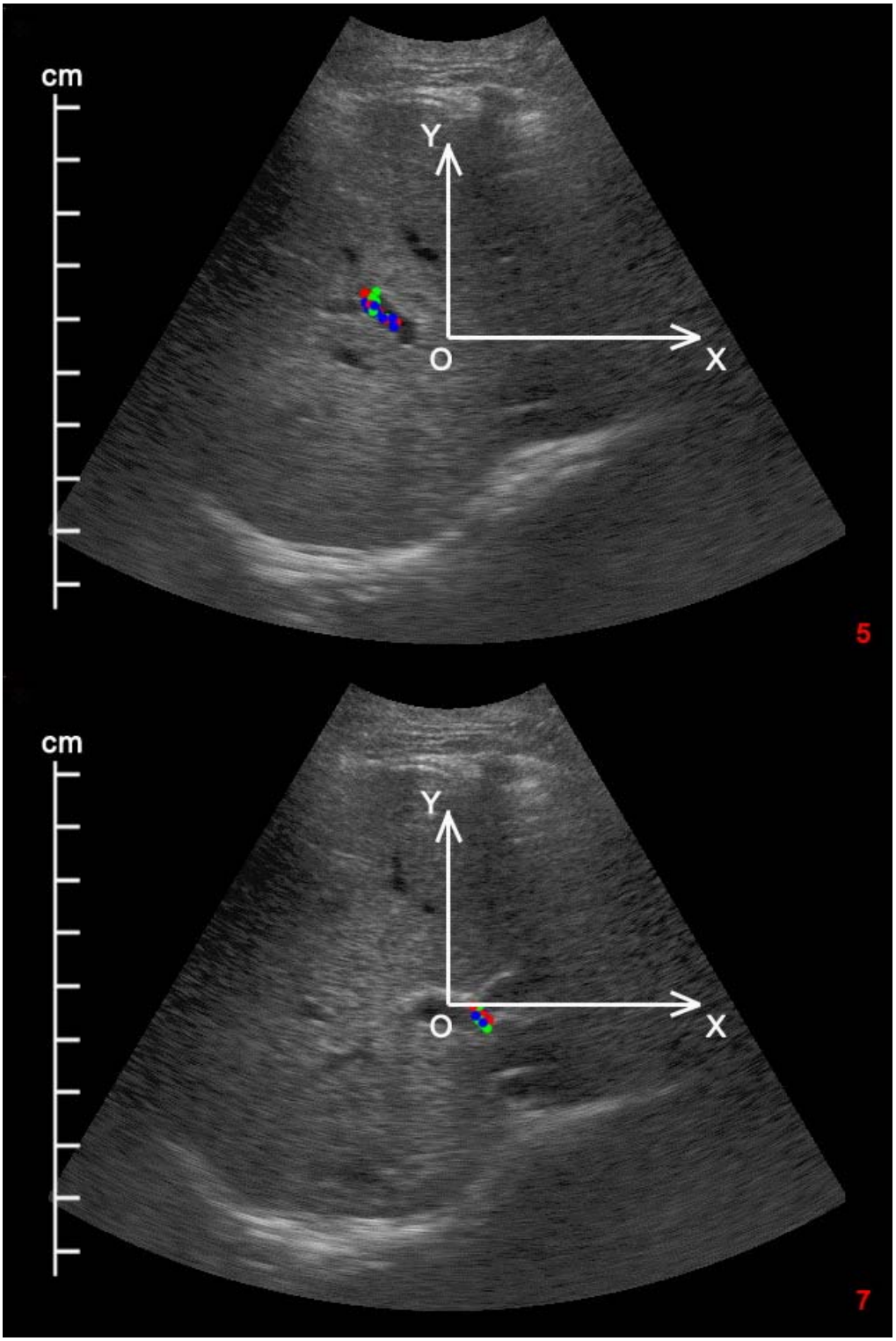

Figure 3.6 Individual landmark trajectories as annotated by three engineers (presented in three different colors) of four landmarks (n = 1, 3, 5, 7)

3.7.3 Motion analysis

In this study, the outlines of the liver boundaries, and the position of landmarks, were overlaid, on a frame-by-frame basis on P_r during a half respiratory cycle, in order to characterize the sequential history of liver movement. Figure 3.7(A, B) shows the annotation of the liver boundaries during a half respiratory cycle for subjects 1 and 3, respectively. The displacement of the liver boundary from *EE* to *EI* is shown in the figure, using a color map format. The overlaid trajectories also depict a difference of degree in liver displacement between two subjects during a half respiratory cycle. Similarly, Figure 3.7(C, D) shows the annotation of the position of the landmarks of the same two subjects, at the same half respiratory cycle. The displacement of the landmarks from *EE* to *EI* is shown in the figure by again using a color map format.

In order to quantitatively analyze the subject-specific liver motion, the movement of the liver boundary point which was farthest from the X axis was chosen to describe the displacement in Y direction, and this is shown in Figure 3.8 for each subject. Similarly, the displacement of the landmark in Y and X directions was also measured for each subject, and this is shown in Figure 3.9 and Figure 3.10, respectively. Between *EE* and *EI*, the liver boundary of subject 3 showed the biggest displacement in negative Y direction (12.9 mm), while subject 4 showed the smallest (6.3 mm). The analysis of the velocity of the liver boundary of the four subjects in Figure 3.8 shows the tendency for the velocity to reach maximum value in negative Y direction at the middle phase between the *EE* and *EI*. A similar tendency was also observed, as shown in Figure 3.9 and Figure 3.10, for the landmarks for the four subjects in both

negative Y and positive X directions. The scale of Figures 3.9 and 3.10 are intentionally kept the same as Figure 3.8.

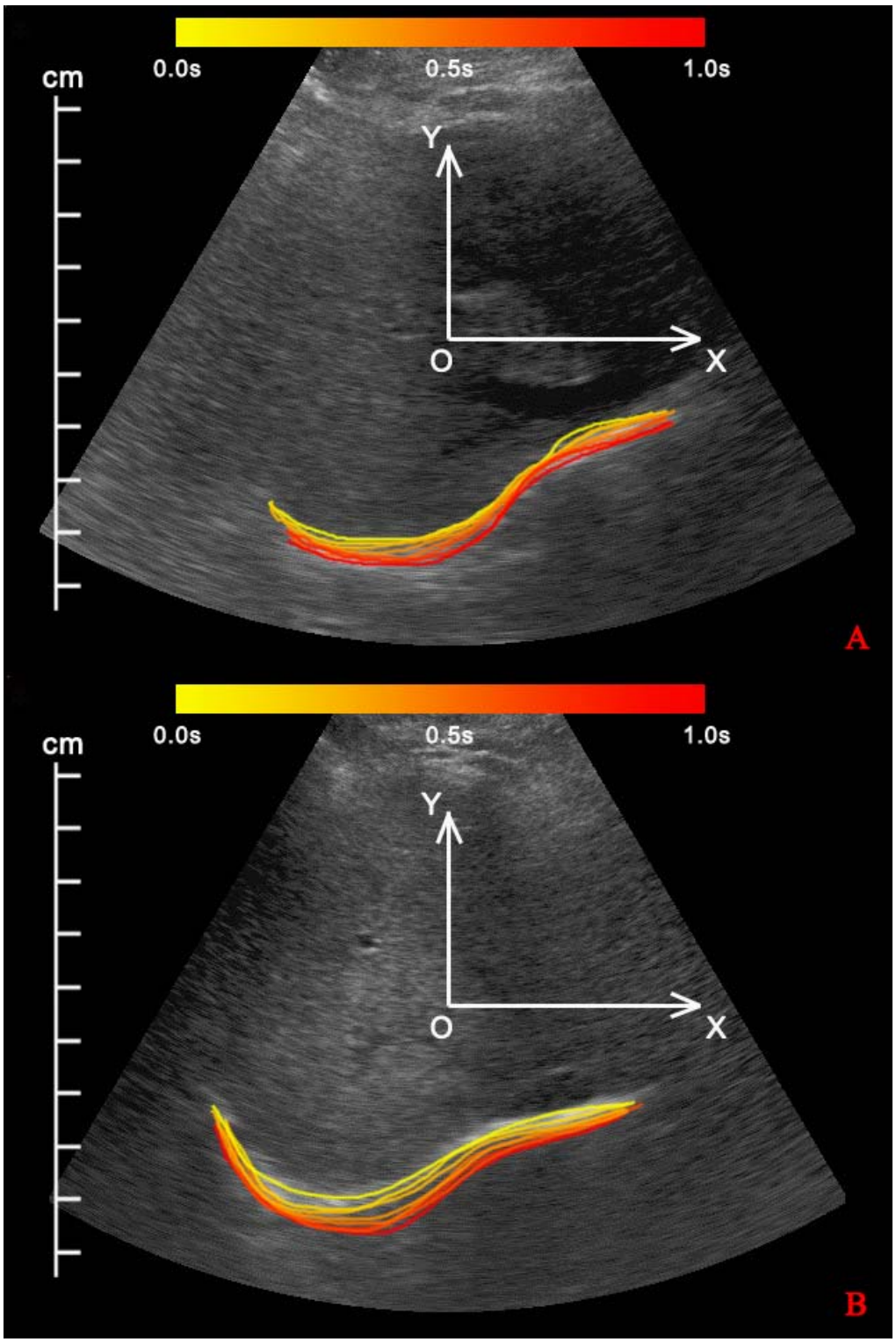

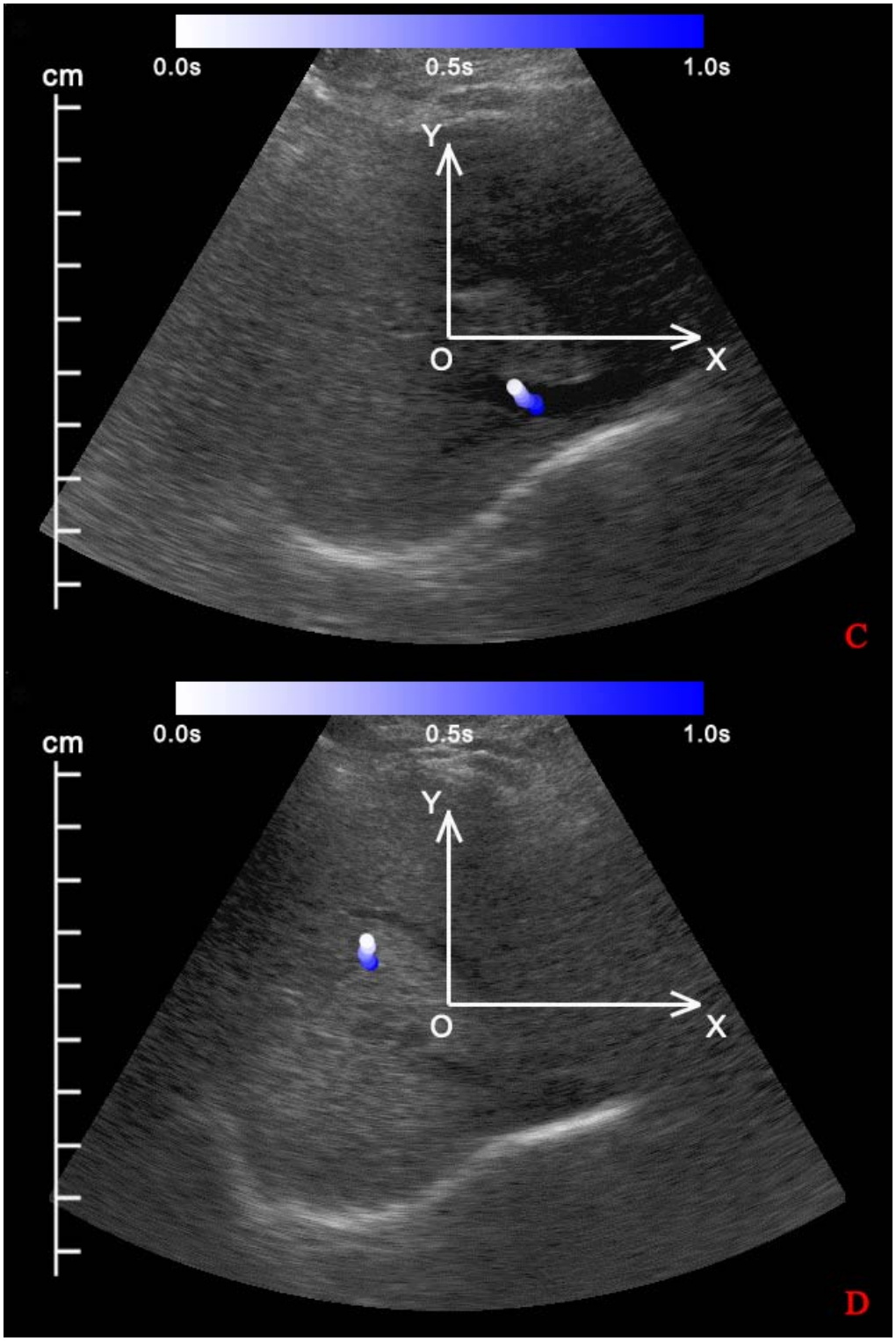

Figure 3.7 The overlay of the liver boundary (A, B) and internal landmarks (C, D) of the two subjects 1(A, C) & 3(B, D). The scale is shown on the left side of each image. The timing of the movement is shown in the color map style at the top. The coordinate system, fixed on the center of the image, is shown in white.

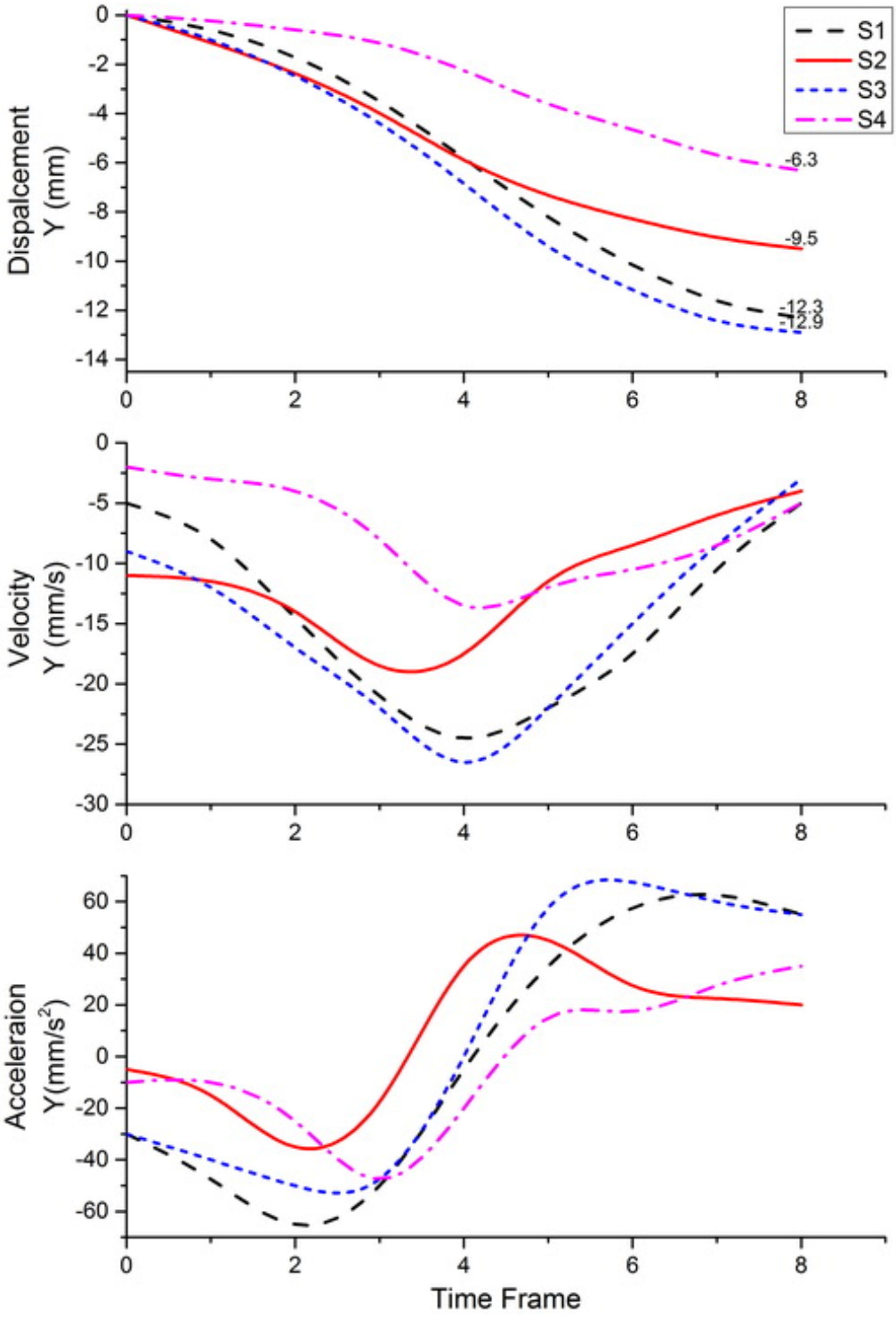

Figure 3.8 The displacement, velocity, and acceleration in Y direction of the liver boundary for the four subjects in Pr. S denotes subject. The figure was plotted in a black dash line, solid red line, short dash blue line, and dash dot pink line, for subjects 1 to 4, respectively.

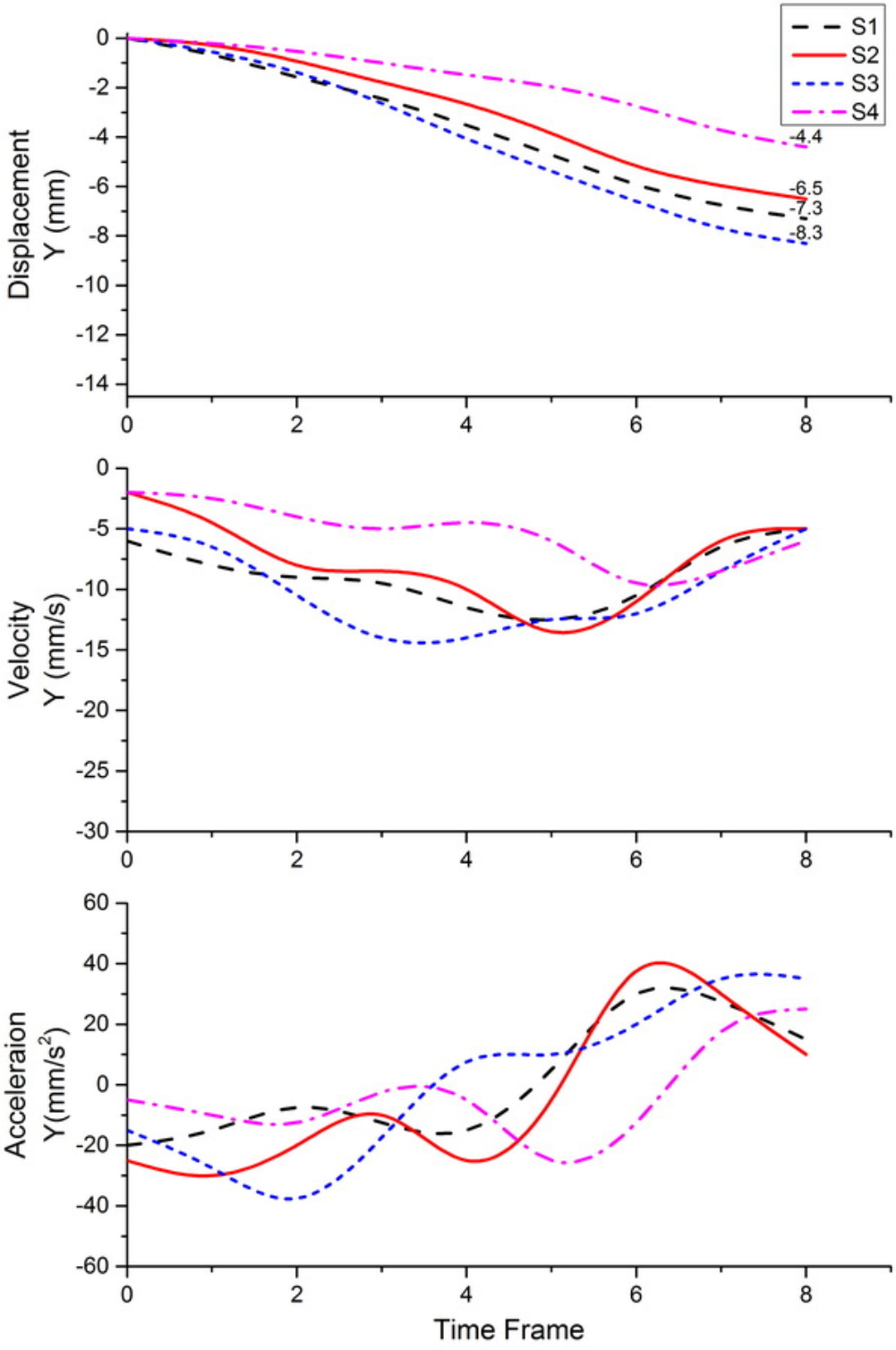

Figure 3.9 The displacement, velocity, and acceleration in Y direction of the landmarks for the four subjects in Pr. S denotes subject. The figure was plotted in a black dash line, solid red line, short dash blue line, and dash dot pink line for subjects 1 to 4, respectively. The scale is intentionally kept the same as in Figure 3.8.

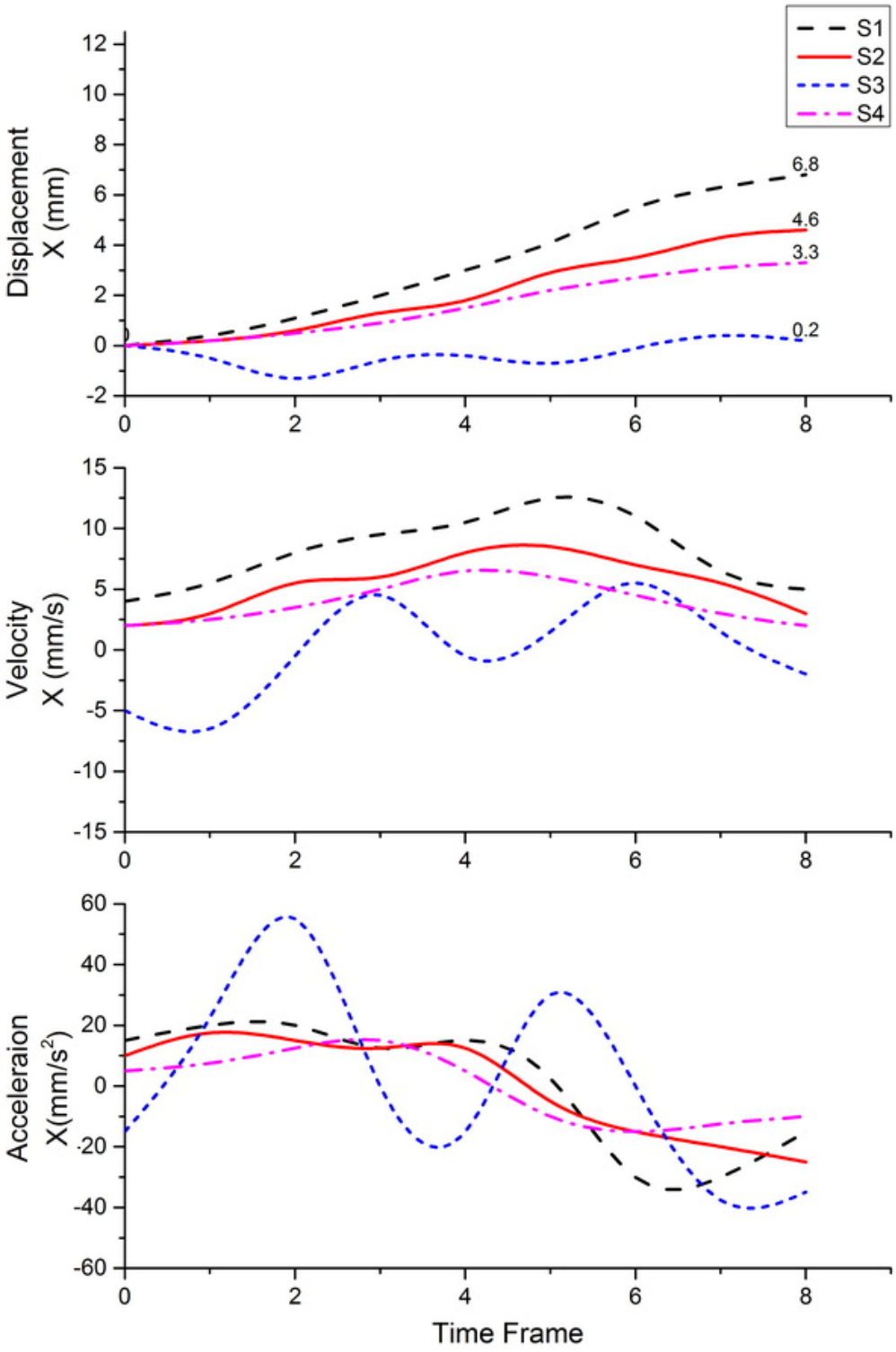

Figure 3.10 The displacement, velocity, and acceleration in X direction of the landmarks for the four subjects in Pr. S denotes subject. The figure was plotted in a black dash line, solid red line, short dash blue line, and dash dot pink line for subjects 1 to 4, respectively. The scale is intentionally kept the same as in Figure 3.8.

3.8 Discussion

In this study, we have explained the process flow of the proposed method, qualitatively demonstrated its feasibility by creating a sequence of respiration-aligned 3D images, quantitatively evaluated the accuracy of generated models, and analyzed the motion of specific anatomical structures based on the models between subjects. Compared to the previously published 4D liver model approach using a 3D ultrasound probe, our proposed method is capable of generating a 4D liver model at low cost and with higher resolution, as well as offering a solution to the problem of the limited field of view of the 3D ultrasound probe. It is also worth mentioning that our fan-shape reconstructed liver model covers an angle of about 31 degrees of the liver area, because we set the probe holder to cover this range of angle only. During the image acquisition step, we placed the US probe between the ribs of the subjects (Figure 3.2), and the field of view was also affected by the obstruction of the human ribs. Theoretically, we can obtain larger field of view by applying our proposed method, if we change the setting of the probe holder to cover a larger range of liver area when we scan the liver.

The use of robotic arm greatly helps us to acquire stable US images of different scanning angles under human respiration. During the experiment, we have tried several settings for the robotic-assisted scanning, and we think what we applied in this study currently provides an optimum balance between image acquisition/model building, and get a representative sample of motion.

The values of the overlap ratio O_{ij} for the liver boundaries at *EE* and *EI* of the four subjects show that there is no significant mismatch between the generated model and the ground truth. Since the calculation of the overlap

ratio was on a randomly selected 2D image plane, the choice of the plane itself would affect the result of the overlap ratio – particularly where, for example, the liver boundary area was not as clear on the selected image plane as on other planes, thus making the manual annotation more difficult and less accurate. The matching error of the landmarks L_n is in an acceptable range for clinical application. The value of L_n was affected by the error of manual annotation, choice of image plane, and the accuracy of the accuracy of respiratory signal extraction method on the landmark tracking. In this study, we purposely did not pick extreme landmarks, to ensure the accuracy of respiratory signal extraction method, so that the evaluation of L_n would make sense.

The X-Y Cartesian coordinate system used to measure the displacement of liver structures, is clinically useful and has good inter- and intra-tester reliability [117]. Based on the results of motion analysis, for all four subjects, the displacement and velocity of internal landmarks were both smaller than those of their relative liver boundaries during *EE* to *EI*. When the position of an internal landmark was closer to the boundary than other landmarks, its displacement from *EE* to *EI* was closer to that of its relative liver boundary.

In addition, the motion difference (displacement, velocity and acceleration) between subjects should not be omitted. We found there was a need to build a subject-specific model, because those differences were caused by the different speed or depth of the respiration of the subjects – which could be crucial to the success of biopsy, ablation, or other clinical applications. According to the feedback from the clinicians, subject-specific information on liver motion or deformation during respiration is a useful clue for them in helping determine

whether there is any tumor inside a patient's liver, or its possible position if this has been verified. In this study, the motion estimation of a 4D volume with 8 frames from *EE* to *EI*, took an average 2-3 minutes. Moreover, the observation of the motion data matches previously published results from other research groups [118, 119].

3.9 Limitations

Our proposed method in this chapter described an indirect way to generate subject-specific liver model from series of 2D US images sequences, however, it should be noted that 3D US transducers have already existed in the market, with capability of scanning real time 3D US image [186], such that technically speaking, generate 4D subject-specific model directly from 3D US images could be possible. Although 3D transducers and related speckle tracking techniques also suffer from image quality issue [87, 186], we think the clinical use of 3D transducer will be more and enough, with the steady increase of its visibility in the study field. In US-guided liver research area, currently the 3D US transducer cannot cover the whole right liver at one single scan, so usually multiple 3D images are assembled together for reconstructing the whole right liver area. In fact this strategy is very similar to our proposed method. So far, we believe our proposed method still has its clinical values as described in this chapter.

3.10 Conclusion

In this chapter, we have proposed a subject-specific 4D ultrasound imaging method, based solely on real-time robotic-assisted-swept 2D ultrasound to

visualize and analyze liver motion. This method detects ultrasound images with the same respiratory phase, from different 2D image sequences acquired with different sweeping angles, and resamples them to create respiration-corrected 3D image volumes. The methodology used illustrates that we were able to capture liver motion at a specific respiratory phase. By applying this method, we found that the motion of the liver between various scan subjects can be quite different. This method is currently used as a preoperative tool for making a subject-specific liver model, to improve diagnostic and therapeutic efficiency in clinical practice. Finally, it will also enable US-guided surgical robots to utilize a built-in respiratory signal tracking system, resulting in more flexible design at lower cost.

CHAPTER 4. PHANTOM STUDY - DYNAMIC LIVER PHANTOM: DESIGN, VALIDATION, AND TEST FOR US BIOPSY SYSTEM

Phantoms that can simulate the dynamic motion of liver tissue are always strongly needed. Chapter 4 describes the design concepts, and the mechanical design of a novel dynamic phantom. The capability of the phantom for generating stable and repeatable movement cycles to simulate human respiration, and test the biopsy system, is verified.

Parts of the following results were first published in: ***C Li****, SP Ang, J Liu, H Yu, 'A Dynamic Liver Phantom for Ultrasound Image Guided Biopsy', 15th International Conference on Biomedical Engineering (ICBME), Springer International Publishing, 2014: 152-155.*

4.1 Introduction

For the last several decades, liver biopsy has been considered the gold standard for obtaining histological diagnosis, and as such is widely applied in hospitals all over the world. However, to date, this minimally invasive procedure, which requires accurate needle placement under ultrasound guidance to effectively target the lesion, is still difficult, mainly because of the problem of liver motion induced by human respiration [115]. Human liver is neither rigid nor directly accessible, so testing objects that are able to simulate the dynamic motion of the liver are keenly needed and of vital importance for the related researches, as well as hands-on practice training for clinicians. Unfortunately, living subjects or cadavers, though most suitable for use, are not always available, or are extremely expensive. In most cases, researchers must make use of liver phantoms to evaluate the effectiveness and performance of imaging and surgical devices, thereby tuning the performance of such devices before they go for clinical trials. These phantoms reduce reliance on living subjects and cadavers for such purposes, at the same time reducing the potential harmful effects of such devices on living subjects.

To date, most of the liver phantoms on the market or in the research field have been static ones [120-133], and commercialized versions are expensive. Higher-quality static phantoms with removable organs can cost up to USD$15,000 [134]. The cost of dynamic phantoms can often be higher due to the addition of mechanical parts, such as actuators to drive the periodical movement [135]. Moreover, it is hard to accurately replicate the movement of the liver based on real patient data in dynamic phantoms, which requires

extremely accurate calculation of the respiratory cycle and control of the actuator, thus hugely increasing the design and fabrication cost. In fact, the liver does not generate motion itself, but sustains an induced motion from the respiratory cycle. Hence, most dynamic liver phantoms employ a one-dimensional linear motion generator, which pushes against a synthetic liver, such as the one developed by Cleary [123] with its magnetic tracking system that follows the movement of internal organs. However, most phantoms are adapted for MRI or CT systems [120-133]. Therefore, there is a strong need for a phantom that can both simulate the dynamic motion of liver tissue and which is also technically practical for the US image guided system.

Motivated by this need, we propose a novel dynamic liver phantom to be applied in ultrasound image-guided liver biopsy study.

4.2 Supporting Data and Design Concepts

4.2.1 Supporting data

The liver is located in the upper part of the abdomen, and has a dimension of 210-225mm in width, 150-175mm in height, and 100-125mm in depth [135]. Most of the motion experienced by the liver is actually induced by other organs, such as the diaphragm, which is in close proximity. According to research by Xi et al. [118], the mean mobility of the liver is 1.3±0.5mm in the left-right (LR) direction, 1.2±1.0mm in the anterior-posterior (AP) direction, and 10.1±3.9mm in the cardio-caudal (CC) direction; liver movement in the CC direction is very close to that of the diaphragm (Figure 4.1). Xi et al. also states that even though the movements of the diaphragm and liver are not

perfectly aligned, the determination of the safe border of the liver tumor can be determined by using diaphragmatic movement.

Item	LR (mm)	AP (mm)	CC (mm)
Diaphragm	–	–	10.3 ± 4.0
Liver	1.3 ± 0.5	1.2 ± 1.0	10.1 ± 3.9
Left kidney	0.8 ± 0.4	2.1 ± 1.7	9.3 ± 2.9
Right kidney	0.8 ± 0.6	1.7 ± 1.5	9.6 ± 4.1
Pancreas	2.3 ± 1.0	2.2 ± 1.3	7.6 ± 3.0
Spleen	1.2 ± 0.8	1.1 ± 1.4	10.6 ± 3.3
Para-aortic lymph nodes	1.7 ± 0.6	1.8 ± 0.5	5.7 ± 1.8

Figure 4.1 Liver movement in the CC direction is very close to that of the diaphragm [118]

This observation is further corroborated by the research of Rubin et al. [137]. In their research, liver tumor positions in the exhale and inhale stages were tracked using 4-Dimensional Computed Tomography (4DCT) scan; the results showed that the main movements of the liver tumors were in the CC direction and also in the AP direction, with negligible movement in the LR position. According to their results, during the inhale phase, the liver tumor moved down and in anterior direction, which was in lieu with the motion of the diaphragm, which moves down during the inhale phase, squeezing the liver. Due to conservation of volume, the tumor also has to move downwards and forwards, There were no, or negligible, changes in the position of the tumor in the LR direction.

4.2.2 Design concepts

First of all, our phantom needs to be ultrasound-compatible, which requires putting either gelatin liver models or porcine livers in liquid or ultrasound gel

without air bubbles or gaps, for ultrasound scanning inside the phantom. Second, in comparison with commercially available dynamic phantoms [135], our phantom is designed to be modular and able to accommodate different sizes of liver; hence, this is a one-model-fits-all design, which makes it more cost effective. Given the modular design, any part damaged during usage can be replaced easily, with no need to replace the whole phantom, thus greatly reducing the overall cost of running the phantom experiments. Third, most phantoms are opaque, meaning if there is any problem inside, it is difficult to rectify, since it is hard to visualize the error. Our phantom, being made entirely of acrylic, is transparent, and can be easily validated with visual cues, making visual observation of liver movement easier. Lastly, some phantoms can only use one type of setting. This phantom, being modular in design, is capable of changing speed and stroke length for both extension and retraction, and adjusts according to the shape of the liver.

4.3 Mechanical Design of the Phantom

Figure 4.2 shows the design of a chest-like shaped phantom. It consists of a linear servo actuator for respiratory motion generation and an ultrasound-compatible compartment that can hold either gelatin liver models or porcine livers for testing.

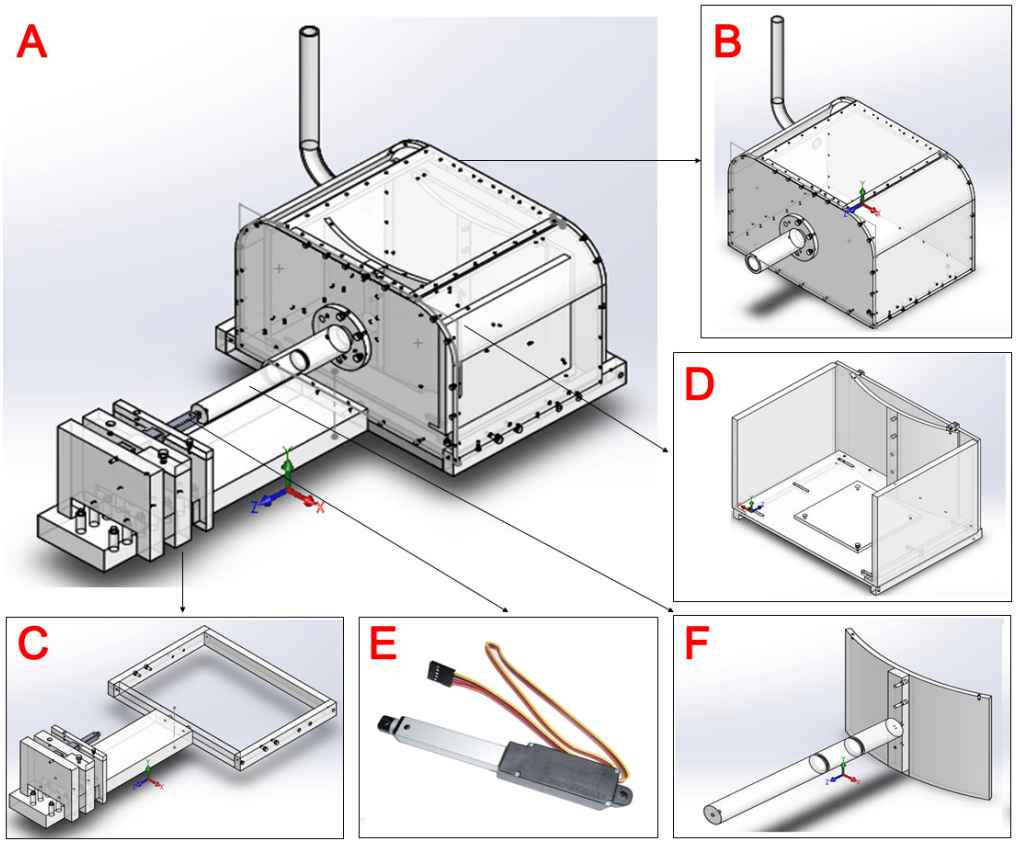

Figure 4.2 Design of the phantom

The chest-like case (Figure 4.2.B) is made of the water-proof material acrylic, with a dimension of 330mm measured from left to right, 220mm measured in the CC direction, and 200mm measured in the AP direction. The edge of the box has a radius of 60mm as a design to represent the chest. The box is filled with distilled water to allow easy transmission of the ultrasound wave into the liver. Excess water is displaced through a water displacement tube located on the side of the box. Everything is joined together via nylon screws, to prevent disturbance of the ultrasound image.

The actuator holder (Figure 4.2.C) is designed to hold the actuator in place. The actuator is connected to an actuating assembly, which includes a rod and a pushing plate which acts like the diaphragm (Figure 4.2.F). The actuator also has another stabilizer, to stabilize its front part. The position of the actuator

holder can be adjusted forwards or backwards, using screws at its base to accommodate necessary changes. The actuator is held in place by the clamping action of the top and bottom piece, and also via an M4 screw at the back of the actuator. The whole base is secured to the main phantom through another frame, which has screws at the side to prevent the phantom from toppling over during actuation.

Inside the case, there is a sponge holder (Figure 4.2.D), designed to hold a sponge in place to simulate the soft tissues below the liver, such as for example, the stomach or right kidney. This is because the liver needs support at the other side of the diaphragm. The sponge was chosen to simulate such soft tissues because of its elasticity; it will not exert too much force on the liver when pushed against. Acrylic plates are used to secure down the sponge, since they have a tendency to float on water. During the usage of the phantom, the sponges will be fully soaked in distilled water before putting them into the phantom, to avoid air bubbles being trapped inside, and to reduce the likelihood of floating.

The actuator chosen for the design is the Firgelli L16 actuator [138] with a 63:1 gearing option (Figure 4.2.E), selected for its capabilities at an affordable price. At 10mm/s, it is able to produce a force of 76 N in the actuating direction. As the actuating assembly is only about 1kg in weight, the actuator is able to produce an excess of about 66 N to overcome the resistant force of the liver itself, and also the friction produced by the O-ring in preventing water leakage from the hole. If the force required to resist the friction from the O-rings themselves is very low, the actuator is capable of producing speeds as

high as 15mm/s at a load of 38N, to simulate different breathing conditions. Speeds can go up to 20mm/s.

Figure 4.3 below shows the prototype of our phantom.

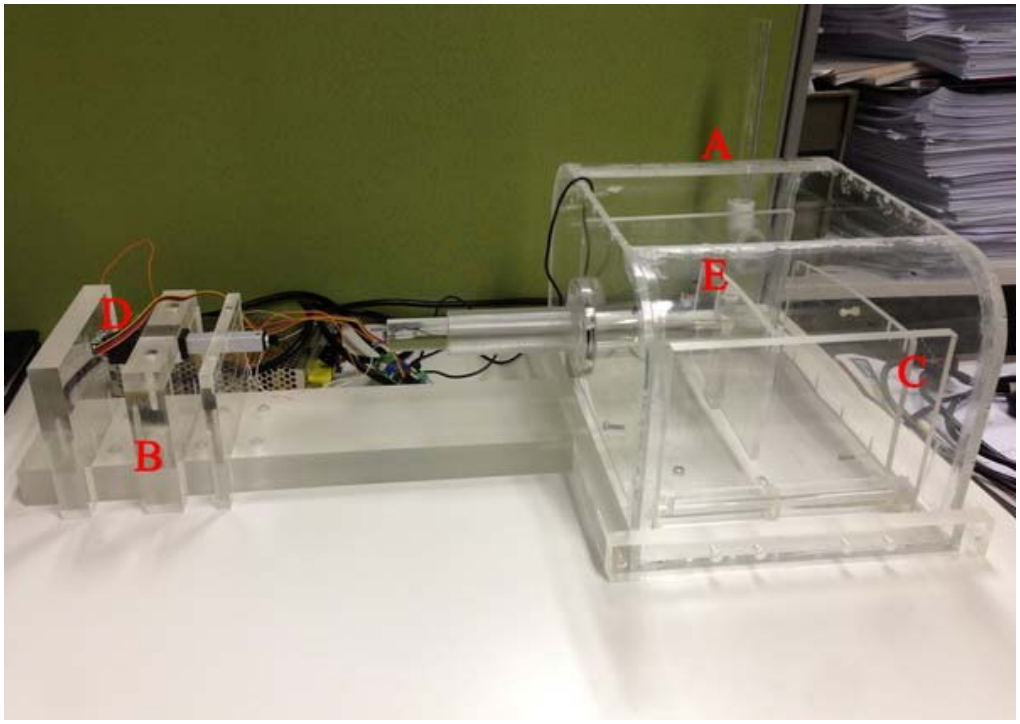

Figure 4.3 Prototype of the phantom. A: chest-like case; B: actuator holder; C: sponge holder; D: Firgelli L16 actuator; E: pushing plate.

4.4 Phantom Control

In the human body, the diaphragm displays a different moving speed during the phases of respiration. During the inhalation phase, the diaphragm will move faster, down against the liver; while during the exhalation phase, the diaphragm will move more slowly, up away from the liver. Hence, in order to display such a trait in the liver phantom, the actuator needs to have a different actuation speed during extension and retraction. We wrote a new customized program for the phantom using Labview, which allows different retraction and

extension speeds, and also allows variable extension and retraction limits. Figure 4.4 below shows the customized Labview program for the actuator.

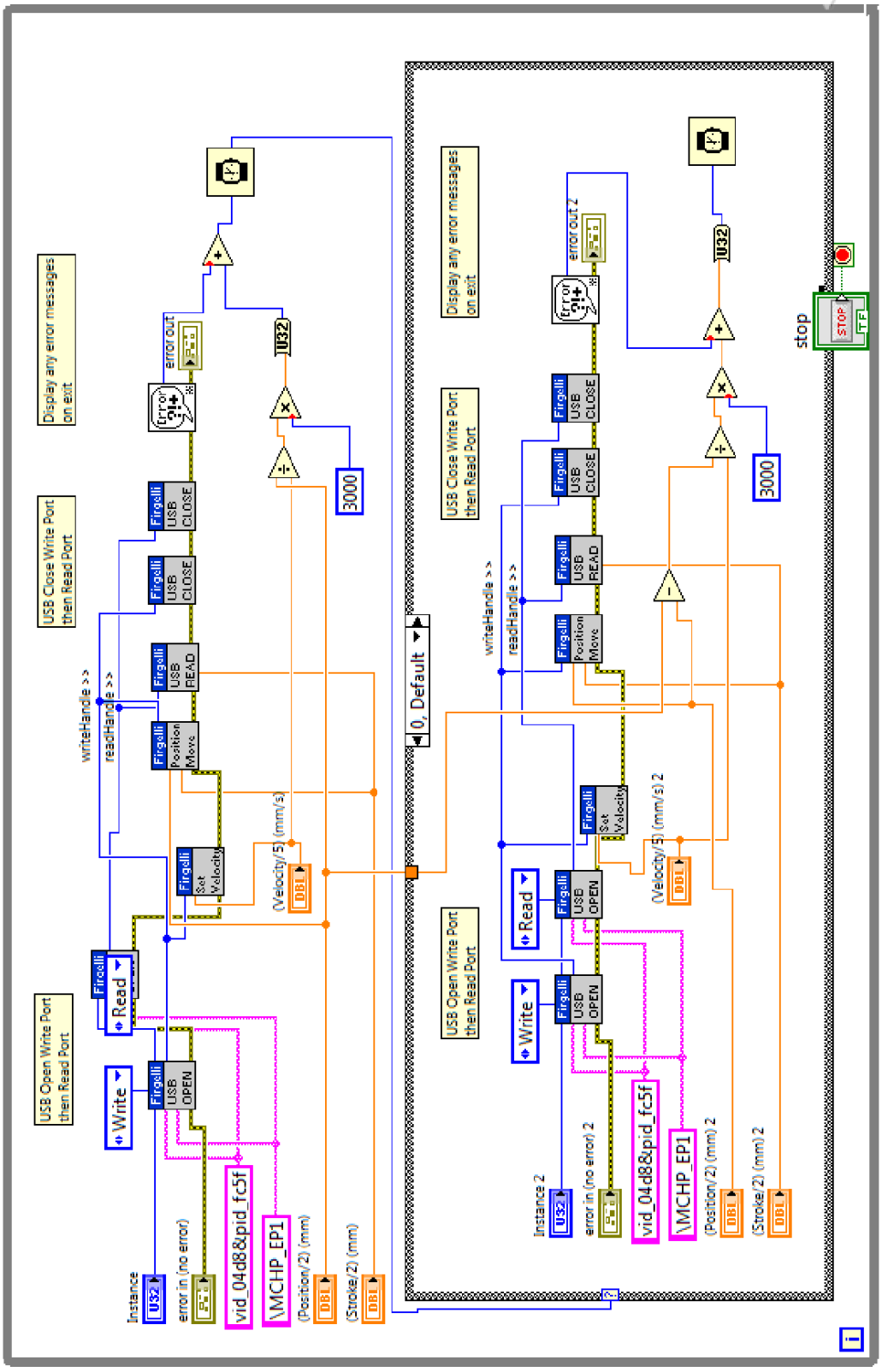

Figure 4.4 Customized Labview program for the actuator

4.5 Experiments

4.5.1 Validation

Experiments were conducted to test the effects of actuation against the liver on the distance moved by the liver in the 3 different directions X, Y, and Z (Figure 4.5), during repeated cycles. This was achieved by placing tracing markers, which, in this study, were steel bolts, on the surface of the porcine liver (Figure 4.6), and tracking the distance moved by the markers in relation to a starting point O. The steel bolts were chosen for ease of detection from the real-time ultrasound images, their distinct shape and small size.

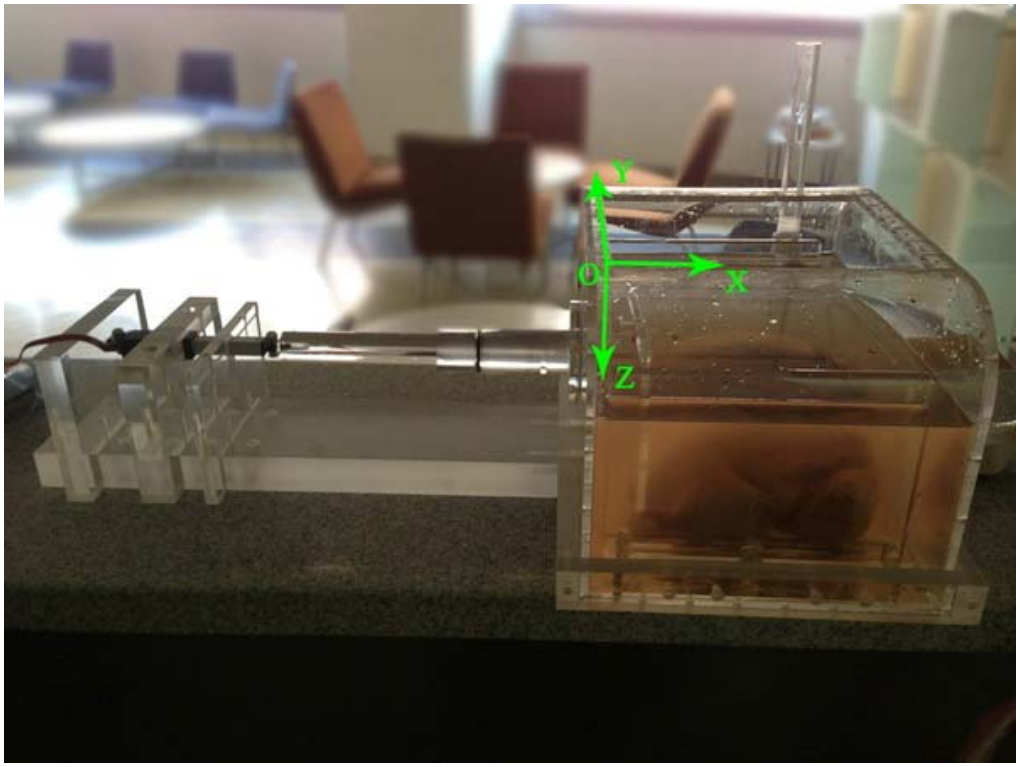

Figure 4.5 Coordinates definition of the phantom

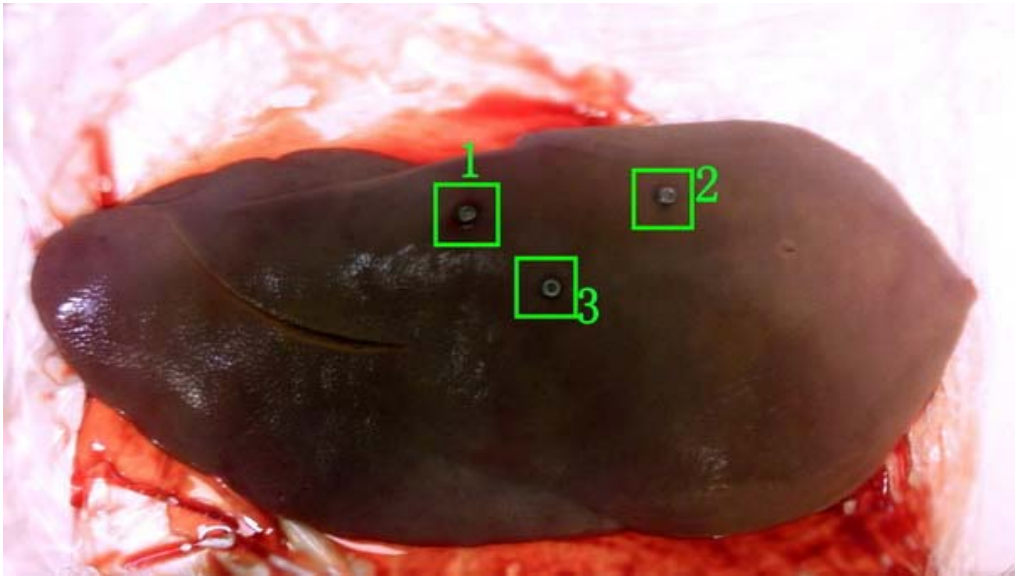

Figure 4.6 Placement of 3 steel bolts on the surface of porcine liver

During the experiment, the actuator was moved forward in steps of 5mm up to 20mm in the X direction, and retracted back in steps of 5mm to the start position. The 20mm limit was chosen since liver movement will proceed up to a limit of about 14mm in the CC direction [127]. A buffer of 5mm was given for extreme cases. Measurements were taken in steps of 5mm due to the impracticality of using a 2D ultrasound probe (Terason t3000 scanner with a 5C2 transducer; image size: 640 × 480 pixels, pixel size: about 0.37 × 0.37 mm, temporal resolution: about 10 FPS) [139] to track the motion. The cycles repeated 10 times in the forward direction (positive X direction), and the same in the retraction direction (negative X direction) to generate more data and ensure that the results were consistent. Figure 4.7 shows the movement of the pushing plate from the start position (A, 0mm) to the maximum position (B, 20mm) in the X direction. During the experiment, we held the ultrasound probe vertically above the water level and tried to acquire a clear ultrasound image with the marker captured. When the real-time ultrasound image caught the marker at a fixed location (Figure 4.8), we recorded the position of the

ultrasound probe, and then calculated the position of the marker based on the ultrasound image.

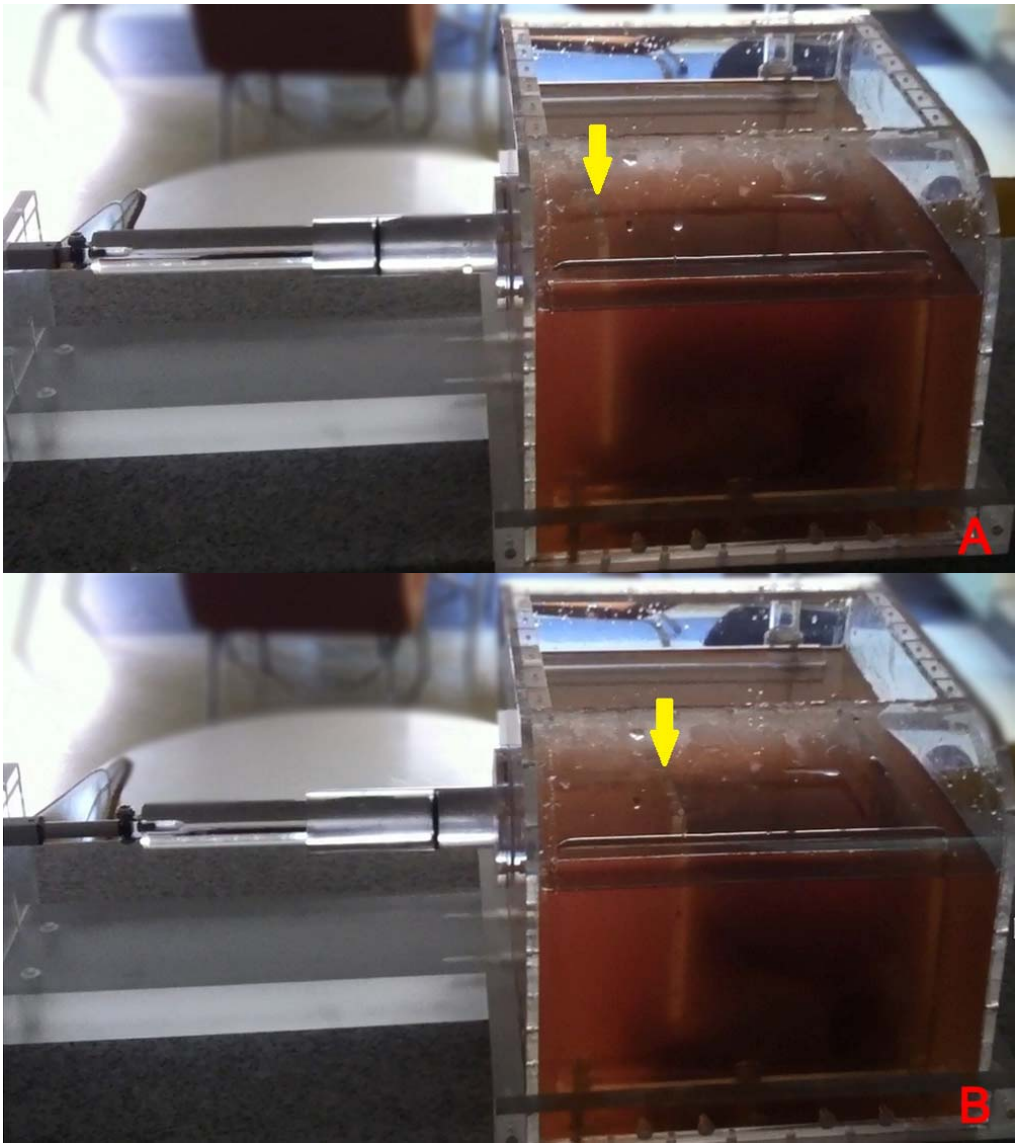

Figure 4.7 Movement of the pushing plate from the start position (A, 0mm) to the maximum position (B, 20mm) in the X direction

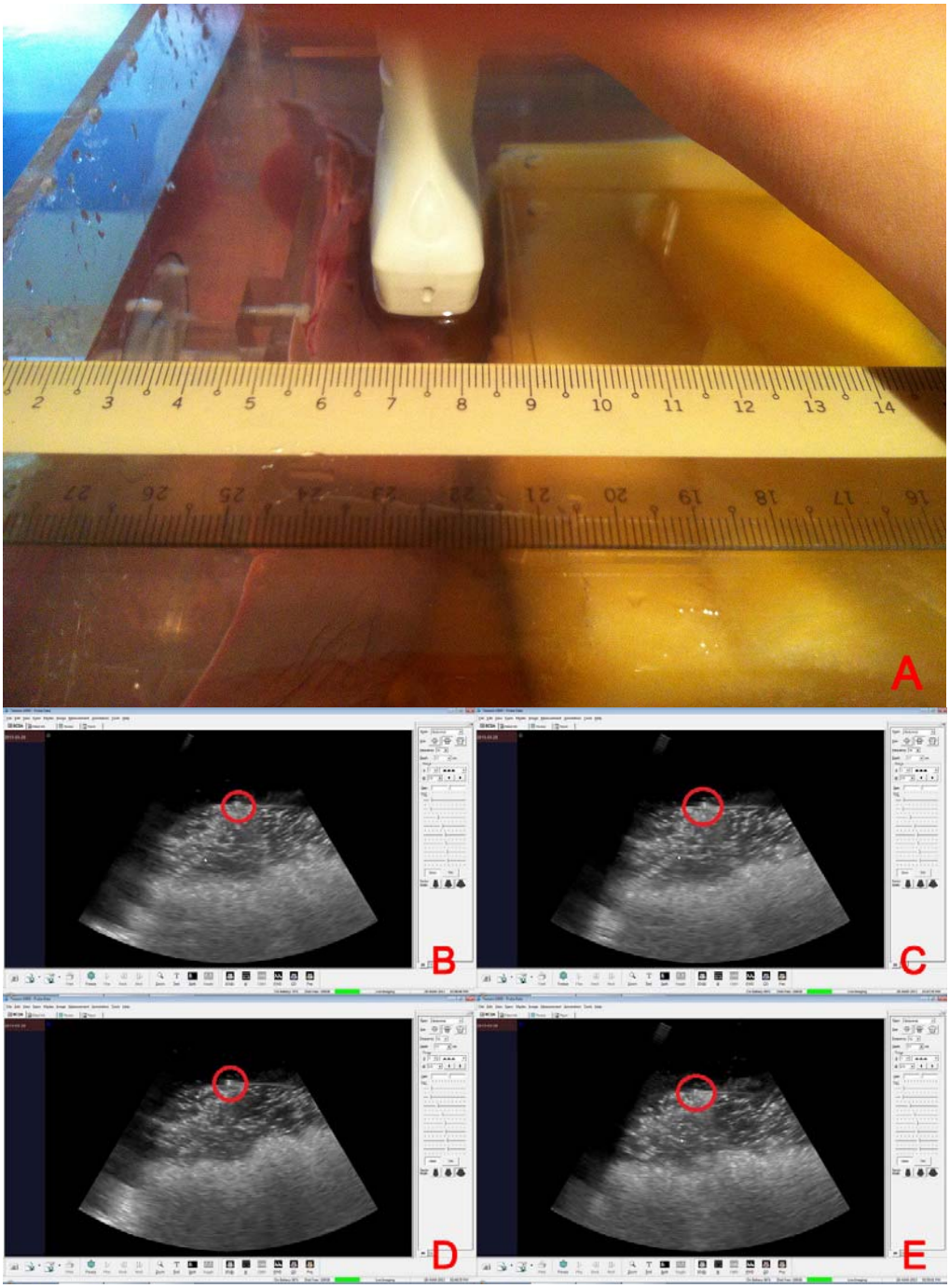

Figure 4.8 Detection of the position of markers using Terason t3000 ultrasound probe (A), and real-time US image of the marker (in red circle, B-E).

4.5.2 Biopsy test on the phantom

The purpose of this experiment was to test if this dynamic phantom is suitable for biopsy study. To simulate a tumor as a biopsy target inside a

porcine liver, an agar-based mixture [140] was prepared and injected into 6 porcine livers at 3-4 sites, with varying ‘tumor’ sizes, ranging from 2 to 4cm (mean 3cm) in diameter, using an 18-gauge syringe at room temperature. In total, 20 sites were created. The details of our novel method to create simulated tumors inside porcine livers, and its validation in ex-vivo and in-vivo experiments, will be discussed in the next Chapter.

The porcine liver with injected simulated tumors was placed in the phantom. In order to simulate real biopsy conditions, the actuator was moved forwards to 15mm directly in the X direction at speed of 10mm/s, retracted back to the start point at same speed, and held in this position for 5 seconds, until the start of the next cycle. This cycle was repeated to ensure the stability of the phantom, as it would have to go through many cycles before the actual biopsy was performed. The 15mm stroke length was chosen to simulate the condition of the liver at the end of the inhale (*EI*) phase. The 5 seconds of stasis at the start position (0mm) was set to simulate the interval between two respiratory cycles in healthy individuals. The same ultrasound probe and probe holder that connected to a robotic arm, as described in Chapters 2 and 3, were used for ultrasound image guidance and needle insertion assistance. A standard biopsy needle was used for all sampling trials. In this experiment, the clinician performed the biopsy during the 5-second static period of the phantom, after the ultrasound image of the simulated tumor was revealed and confirmed on the computer screen at the start position (0mm). Once the clinician started to insert the biopsy needle, the phantom stopped the set cycle movement and remained stationary. Only one biopsy attempt was applied for each injected tumor. All specimens were analyzed carefully after each attempted biopsy. A

detailed description of the biopsy procedure in this experiment will be given in the next Chapter.

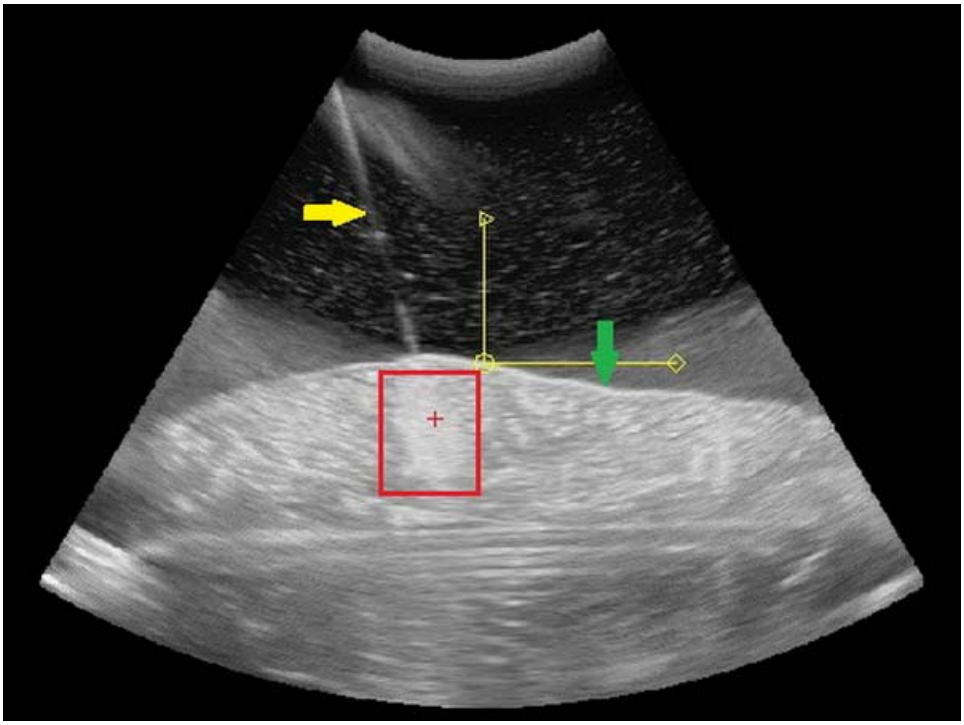

Figure 4.9 Targeting of the injected simulated tumor. Red rectangle: target; yellow arrow: trajectory of biopsy needle; green arrow: boundary of porcine liver.

4.6 Results and Discussion

4.6.1 Validation

The results collected for the positions of the markers are shown in Table 4.1. Avg denotes the average position out of the 10 measures in 10 different cycles, while S.D. denotes the standard deviation of the positions measured for the 10 sample sizes. Figure 4.10 shows the side view of the pathways of 3 markers as averages.

Table 4.1 Average position reading of 10 cycles for 3 markers (unit: mm)

		0mm			5mm			10mm			15mm			20mm		
		X	Y	Z	X	Y	Z	X	Y	Z	X	Y	Z	X	Y	Z
1	Avg.	76.07	45.14	54.14	80.55	44.85	53.25	85.35	44.80	52.35	89.80	44.40	50.45	93.50	44.42	47.17
	S.D.	0.78	0.83	2.18	0.57	1.10	1.57	0.74	1.08	0.63	0.56	0.92	0.61	0.50	1.10	0.75
2	Avg.	72.50	132.57	44.71	77.20	132.60	42.50	81.65	132.10	40.20	85.30	132.20	38.70	89.92	131.50	37.67
	S.D.	0.89	1.18	0.70	1.44	1.11	0.92	1.16	1.30	0.87	1.03	1.54	0.46	1.17	1.89	0.75
3	Avg.	81.43	86.14	55.21	85.70	86.90	54.15	89.95	86.80	52.55	93.50	86.90	51.70	97.17	86.83	48.67
	S.D.	0.56	0.64	0.80	0.64	0.70	0.71	0.76	0.75	0.79	0.50	0.54	1.05	0.69	0.69	1.25

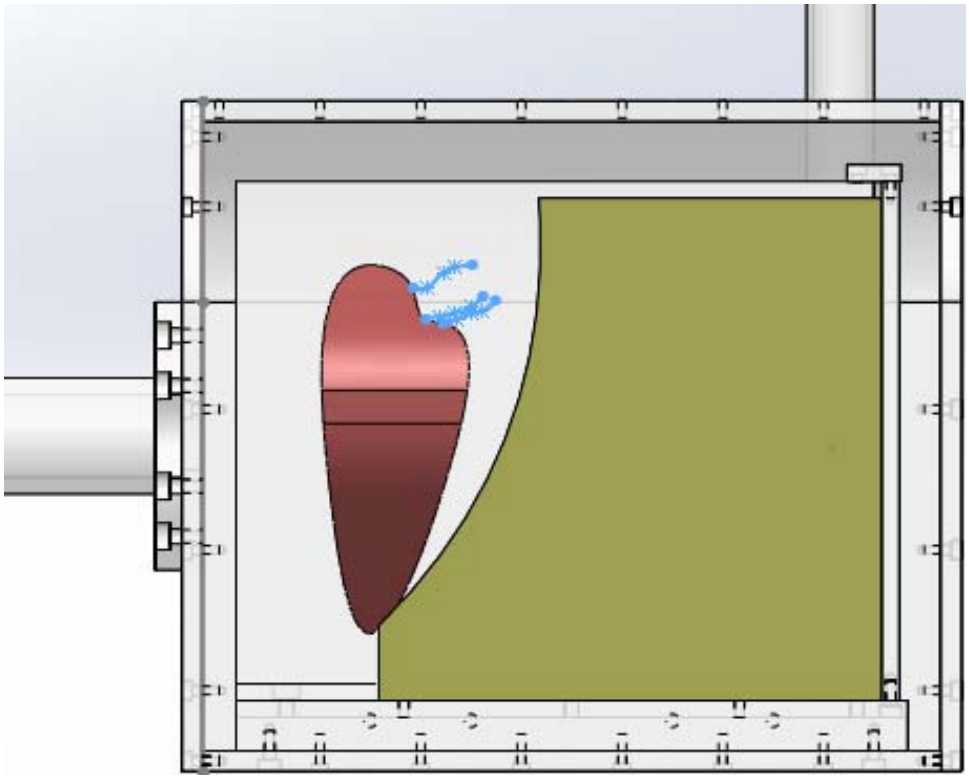

Figure 4.10 The side view of the pathways of 3 markers as averages

The distances moved by the points in the X direction were in lieu of the distance being pushed by the actuator. For the start position, the average changes in distance in the X direction were closer to 5mm, which was the distance the actuator was required to provide. From 10mm to 20mm, the distance moved by the markers decreased slightly, to near 4mm. This was because, when the distance moved by the marker hit 10mm, it was slightly

resisted by the sponge, hence hindering further movement of the marker in the X direction. The marker also moved upwards with increasing actuation in the negative Z direction, because when the liver's movement was impeded by the sponge from moving forward, the surface of the liver had to move up due to conservation of volume. There were negligible changes in the Y direction, since the average movement in this direction was between -0.8mm to 0.8 mm, and there was no regular pattern in the direction of the deformation in the Y direction. Changes due to conservation of volume could have been the cause of changes in the Y direction, but since the liver is irregular in shape, the directions varied.

Distance positions recorded were accurate, as most of the standard deviations of the distance measured were below 1mm, which was the lowest division of the ruler used. The distance moved by the markers, for all 3 markers, was also consistent in all 3 directions, since most of the standard deviations of all the distance travelled for all the points were less than 1mm, while the rest were near 1mm.

4.6.2 Biopsy test on the phantom

For the biopsy test experiments on the phantom, each biopsy attempt was either described as a success (the biopsy being successful in obtaining the simulated tumor, which was white in color) or as a failure (the biopsy only obtained a liver tissue sample). The clinician visually checked the biopsied sample tissues on the white tissue paper carefully. The results showed that the clinician successfully hit the simulated tumor in 15 out of 20 attempts (75%).

Figure 4.11 shows a successful and an unsuccessful biopsy attempt. Figure 4.12 shows a visual check of the injected simulated tumor.

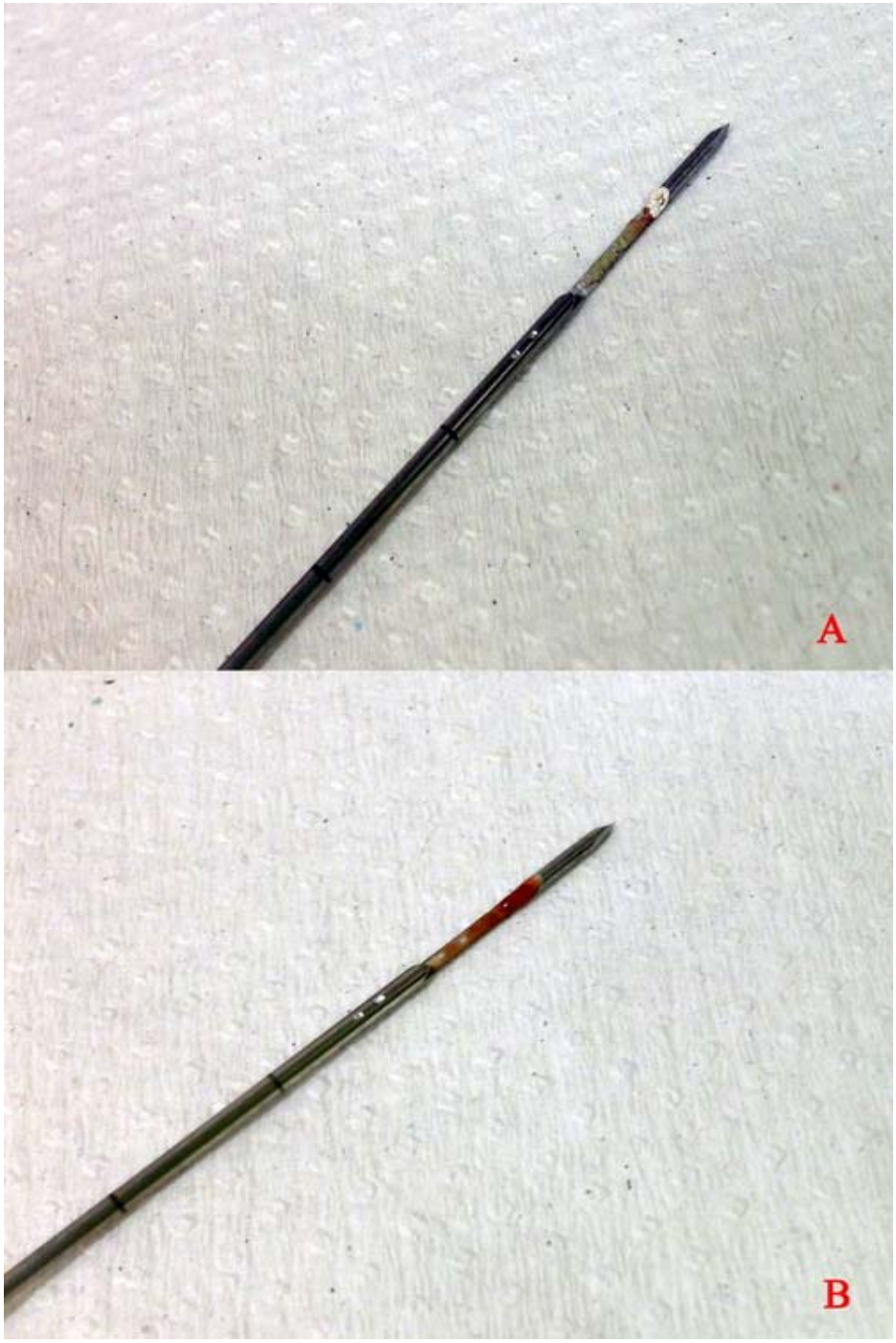

Figure 4.11 A successful (A) and an unsuccessful (B) biopsy attempt, respectively

Figure 4.12 Visual check on injected simulated tumor

It is obvious that targeting and delivering the biopsy on the moving porcine liver in the dynamic phantom is more difficult than on the static phantoms. For the unsuccessful biopsy attempts in this experiment, the possible reasons for failure can be listed as follows. First, the main reason could be the relatively low ultrasound image quality on the target (agar-based simulated tumor) area. In fact, the US image of the metal bolts in the experiment to validate the phantom was much clearer than that of the agar-based simulated tumors. Motivated by this issue, we developed a novel technique to create simulated tumors inside the liver that can be clearly seen under an US image (the details are in the next Chapter). Second, due to the setting of the phantom and its movement pattern, the clinician chose to perform the biopsy during the 5-second static period, as previously described. Though 5 seconds is longer than the normal human respiratory interval (usually 2-3 seconds for healthy individuals under normal conditions [141]), this time was still quite short for the insertion of the biopsy needle – even if the target was identified on the US

image. In addition, 5 seconds was not enough time to both locate the target on the US image and insert the needle. An ideal situation would be the clinician locating the simulated tumor in the first interval, and inserting the needle in the next. However, this would require the simulated tumor to appear in the same US image plane in two consecutive intervals, whereas unfortunately, this did not happen every time. Third, the error caused by manual manipulation of the biopsy needle cannot be neglected, since the porcine liver was not fixed tightly inside the phantom. Motivated by this problem, we designed a needle holder in our biopsy system to eliminate this error as far as possible. Lastly, since the porcine liver was submerged in water in the phantom, we noticed that the water wave caused by the movement of the pushing plate could push on the porcine liver, thus leading to minor deformations in it during its 5-second static period. Sometimes this deformation made the target move out of the US image plane, such that the attempt became more difficult.

Finally, it is worth mentioning that without the use of phantom, the validation of the biopsy system becomes weak. During the experiment, the clinicians asked us to set the phantom as described in section 4.5.2, and performed the biopsy at the start position during the 5-second static period of the phantom. The only reason that we did not apply the feature-based tracking algorithm described in chapter 2 in the experiment is that the motion provided by the phantom was well known and totally visible to the clinicians, such that they could freely adjust the US probe at the start position, and located the target in the real-time US image without applying the motion tracking algorithm during the static period of the phantom. In other word, theoretically we could integrate the motion tracking algorithm in the system, and in terms

of techniques, our proposed image processing algorithms and phantom prototyping are actually connected with each other. It was clinicians' choice that simplified the image processing in this phantom experiment.

4.7 Limitations

It is worth mentioning that in terms of phantom design, there are several shortcomings of our phantom that could be improved in the future: (1) better shaped of sponge or other similar materials that simulates the area contacting the bottom of the liver more accurately, can be used; (2) the shape of the pushing plate can also be improved to a curve shape, which is more close to the shape of human diaphragm, to simulate the pushing movement better; (3) we hope to produce a liver organ model whose shape, material and ultrasound properties are close to the real human liver, and can be repeatedly scanned, injected, and inserted, such that the dynamic phantom could provide better simulation of the human liver motion.

4.8 Conclusion

The results shown in this study correspond to the results of the 4DCT scan as conducted by Rubin et al. [137], which was described in the last part of section 4.2.1, whereby the significant distance moved by the tumor was in the X direction, or the CC direction, in the case of this experiment. The experiments conducted in this study and by Rubin et al. [137] also showed little change in the LR directions for the marker or the injected tumor. In the AP direction, both the marker and the liver tumor moved in the anterior direction during the inhalation phase. Hence, we can conclude that the results

obtained by this experiment are conclusive and therefore, the phantom is stable and suitable for use as a liver motion simulator. Given that it is systematically stable, the phantom designed by us has provided a solution to ease the complications experienced by researchers and clinicians, by giving them a phantom which simulates the respiratory motions of the liver that were more readily available and affordable to purchase, as compared to the commercial phantoms. Costs have been reduced by the modular design of the phantom, and also by its capacity for being adapted to different tumor scanning methods; the latter facility also serves to standardize all the results given by different scanning methods, reducing the potential discrepancies that might surface with usage of different phantoms for different systems.

During the experiment, our dynamic phantom simulated some difficulties that could happen in real biopsy practice. The efficiency and accuracy of our image-guided and processing algorithms, as well as the biopsy planning, were well evaluated. Regarding the hardware aspect, the usefulness of the probe holder, robotic arm, and whole biopsy system, were also put to the test. Through the phantom experiment, the clinicians also provided us some practical advice on the image processing procedures. This information will prove very valuable for us in improving the performance of our system.

In summary, the novelties of this work are listed as follows: (1) the design of this dynamic liver phantom is novel, and it is capable of providing stable and repeatable movement cycles under different settings [123, 134-135]; (2) this phantom is adapted for US systems, while most of the existed phantoms were designed for CT or MR system [120-135]; (3) Cost effective in comparison with commercially available dynamic phantoms [123, 134-135].

CHAPTER 5. EXPERIMENTAL STUDY - CREATION OF SIMULATED TUMORS FOR REAL-TIME ULTRASOUND IMAGE-GUIDED LIVER BIOPSY

To solve the commonly seen problem that ideal testing is hard to ensure in an experimental biopsy study, this Chapter presents a novel method to create simulated tumors inside porcine livers ex-vivo and in-vivo, for US image-guided biopsy. The performance of our proposed method is evaluated by comparing it to the more widely used approaches.

Parts of the following work was accepted to be published in: ***C Li****, JY Teo, J Wu, A Gogna, BS Tan, LL Ooi, J Liu, H Yu, 'Creation of Clinically-differential Tumor Mimic Model Using Vaseline-based Materials with Barium Sulfate for the Validation of Real-time Ultrasound Image-guided Liver Biopsy System,' Biomedical Engineering: Applications, Basis and Communications.*

Parts of the following results were first published in: ***C Li****, JY Teo, J Wu, J Liu, LL Ooi, H Yu, 'Ultrasound Image Guided Biopsy on Vaseline-based Mimic Porcine Liver Tumors', 11th Anniversary Asian Conference on Computer Aided Surgery (ACCAS), 2015.*

5.1 Introduction

The accurate diagnosis of solid liver lesions is a key factor in determining appropriate treatment. For the last several decades, liver biopsy has been considered the gold standard for obtaining histological diagnosis [37]. This is a minimally invasive procedure, which requires accurate needle placement under ultrasound guidance to effectively target the lesion. Competency with ultrasound-guided biopsy requires hands-on practice, so we developed a dedicated intelligent robot to assist clinicians in the performance of liver biopsy. However, whilst undertaking the validation of our system, we found that the ideal testing model (liver tissue with an intraparenchymal target) was very hard to obtain. To overcome this problem, several kinds of tumor model have been previously described, such as VX2 carcinoma [142-146], canine transmissible venereal tumor model [147, 148], a solution combining gelatin and agar [149], and an agar-based mixture tumor model [140, 141, 150-153]. However, these approaches present limitations in terms of cost, tumor size, extravasation, convenience in acquiring materials, the amount of time and effort required to produce the model, and most importantly, the inevitably low image quality of the target (simulated tumor) area. For these reasons we found it necessary to develop an easy, safe, and controllable way to simulate the presence of tumors within the liver, so that the clinician can locate the target precisely and easily. The purpose of this study was to develop a technique for the easy creation of solid tumor models of different sizes, that could be used in the validation of ultrasound image-guided liver biopsy systems and other applications, and evaluate its performance by comparison with the most widely used approaches.

5.2 Creation of Simulated Liver Tumors

Two kinds of injectable model were prepared to simulate liver tumors. Their performances as possible targets for biopsy were tested in both ex-vivo and live animal (in-vivo) experiments.

5.2.1 Agar-based tumor model

An agar-based mixture has been previously described as an injectable sonographically visible model, in various studies in the literature [140, 141, 150-153]. The mixture was prepared by combining 10 g of agar powder, and 10 ml of glycerol, with enough distilled water to make up a 200 ml volume (Figure 5.1). The mixture was then heated to 80 ℃ using a hot water bath to bring its components into solution. Once the heating was complete, 5 ml of green coloring was added. Figure 5.2 shows the condition of the mixture under different temperatures. Note that the mixture must be maintained at a temperature above around 45 ℃ in a hot water bath to prevent solidification of the agar prior to injection.

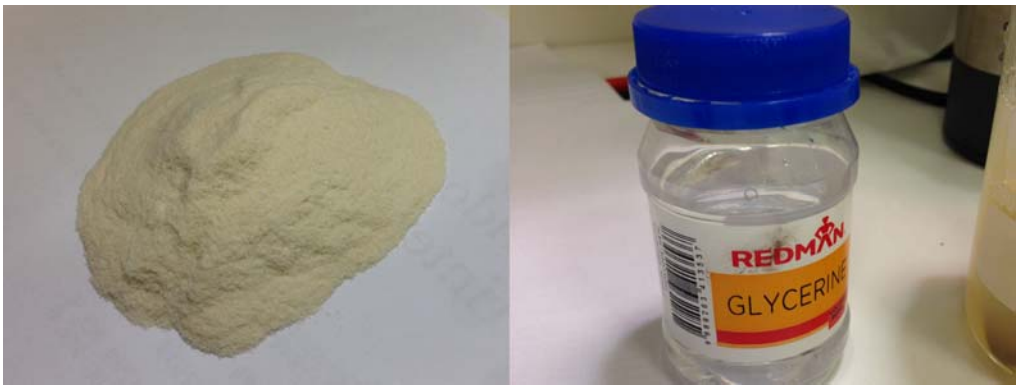

Figure 5.1 Materials for agar-based tumor model: agar powder (left) and glycerol (right).

Figure 5.2 Condition of the agar-based mixture: liquid when heated to greater than 50 ^{o} Centigrade (left); solid at room temperature (26 ^{o} Centigrade, right).

5.2.2 Vaseline-based tumor model

The Vaseline-based mixture was prepared by combining 10 g of Vaseline jelly with 10 ml of glycerol. The mixture was then heated in a hot water bath to bring its components into solution (Figure 5.3). Coloured dye can also be added if desired. Note that the mixture maintains its semi-fluid form even at room temperature, which makes handling of the material less demanding.

In addition, 5 g of barium sulfate was added to the simulated tumor mixture (Figure 5.4). The comparison of ultrasound image quality on the simulated tumors with/without barium sulfate is given in section 5.4.

Figure 5.3 Making the Vaseline-based tumor model: Vaseline jelly (left); hot water bath (right).

Figure 5.4 Addition of clinical barium sulfate to the Vaseline-based mixture

5.3 Experiments

5.3.1 Ex-vivo experiment

In the ex-vivo experiment, we injected both kinds of simulated tumor model into porcine livers with an 18-gauge syringe for tumor implantation. All the porcine livers were obtained from the market on the same day as the ex-vivo experiment.

The Vaseline-based mixture was injected at room temperature into each porcine liver at 2-3 sites, with volumes of 2 ml, 3 ml, 5 ml, 8 ml and 10 ml (2 sites each volume. The detailed relationship between injection volume and simulated tumor size is shown in Table 5.1, in section 5.4). Similarly, the agar-based mixture was injected at 45-50 ℃. We created 1) 10 sites for the Vaseline-based mixture with barium sulfate, on 4 randomly selected porcine livers, 2) 10 sites for the Vaseline-based mixture without barium sulfate, on 4

randomly selected porcine livers, and 3) 10 sites for the agar-based mixture, on 4 randomly selected porcine livers. Then the porcine liver with the simulated tumors in-situ was placed in a transparent plastic box immersed in water as previously described, for targeting. Figure 5.5 shows implantation of the Vaseline-based simulated tumor material into a porcine liver using an 18-gauge syringe.

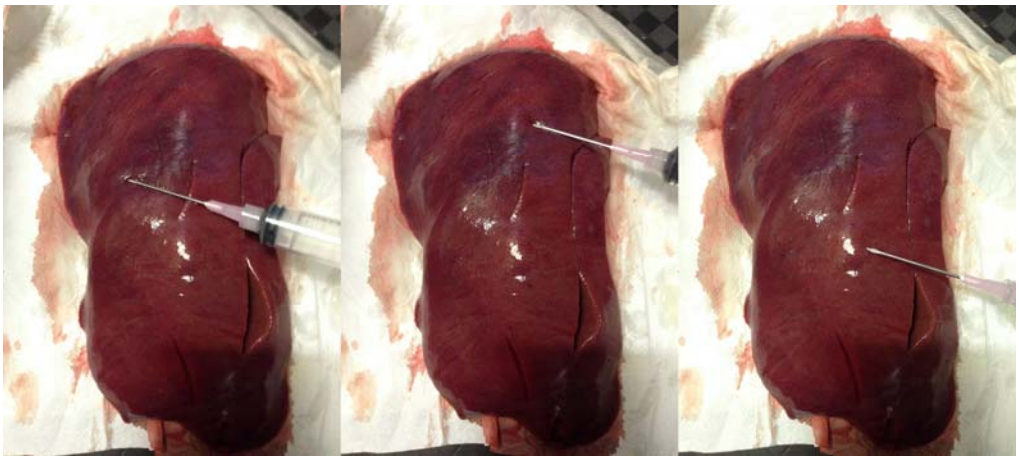

Figure 5.5 Injection of Vaseline-based simulated tumor model in ex-vivo experiment

5.3.2 Live animal (in-vivo) experiment

Because of the physiological and anatomical similarities between pigs and human beings, one micropig (45 kg) was used in a live animal experiment. After overnight fasting, anesthesia was induced by intramuscular administration of atropine (0.05mg/kg) followed by xylazil (2.5mg/kg) and ketamine (10mg/kg). Then, the micropig was intubated using an appropriate size cuffed endotracheal tube connected to a ventilator, and the deep anesthesia was maintained additionally by inhalation of 5-10% of isoflurane. During the experiment, the micropig was fixed with its legs by ropes on an

operating table in the supine position, and monitored with oxygen saturation (SpO2) (Figure 5.6).

Figure 5.6 Preparation of the micropig for in-vivo experiment.

Before implantation of the simulated tumor, the abdominal area of the micropig was shaved and scrubbed with iodine- and alcohol-soaked gauzes. The injection was guided by real-time ultrasound to locate the liver area (Figure 5.7). Since the skin and subcutaneous tissue of a micropig is much thicker than that of a human being, the injection point on the skin of the micropig needed to be cut by a surgical knife to ease the injection. The clinician injected the micropig with the Vaseline-based mixture with barium sulfate in a total of three sites (5 ml each). The Vaseline-based mixture with barium sulfate was stained with bromophenol blue for easier visual checking.

Figure 5.7 Injection of Vaseline-based simulated tumor model in live animal (in-vivo) experiment.

5.3.3 Targeting of simulated lesion

For both the ex-vivo and in-vivo experiments, the targeting procedures were similar. The ultrasound probe was connected to the robotic arm, and real-time ultrasound images were obtained and processed on self-developed software platform MIUE [114] during the procedure. In order to avoid the issue of the tremor of human hands, a probe holder was designed to clamp the probe and help to scan the liver with optimum stability. The anticipated scanning angles were actuated by a geared motor (Faulhaber DC-Micromotor 0615, Schönaich, Germany). The motor was connected to a computer using Ethernet (via a network cable). A needle holder was designed to fix the biopsy needle in the same plane as the US probe, but the needle angle was adjustable within this

plane. A standard biopsy needle was used for all sampling trials. The setup of ex-vivo and in-vivo experiments can be seen in Figure 5.8.

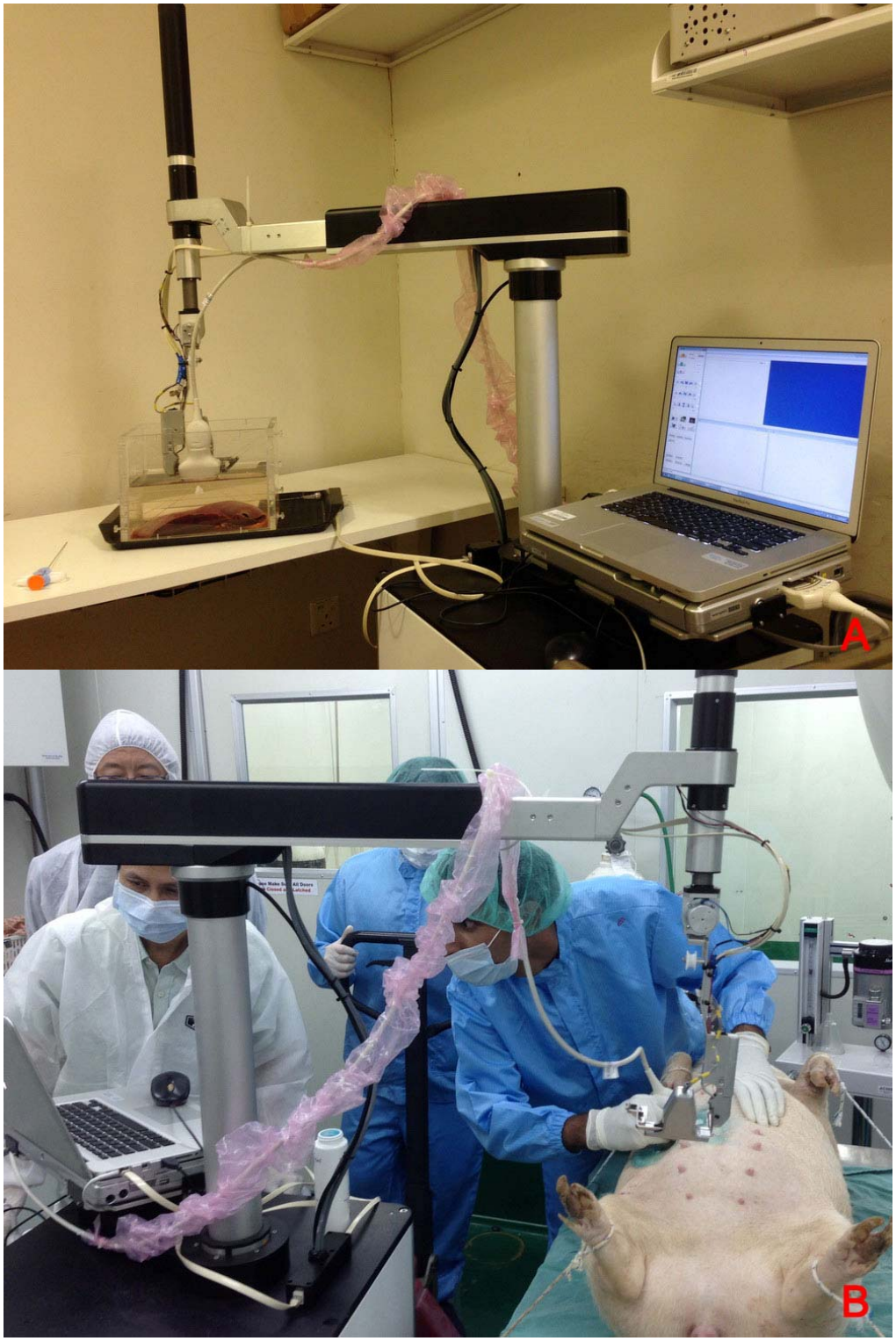

Figure 5.8 Setup of the ex-vivo (A) and in-vivo (B) experiments.

The tumors were located using real-time ultrasound. A Terason t3000 scanner with a 5C2 transducer was used for acquiring US images (image size: 640 × 480 pixels, pixel size: about 0.37 × 0.37 mm, temporal resolution: about 10 FPS) [139]. The lesion to be targeted was selected using the robotic arm.

For each biopsy attempt, a one-time fan scan of the ultrasound probe was applied to cover the biopsy area. After that, a 3D ultrasound image model for ex-vivo experiment, or a respiration-correction 4D model for in-vivo experiment, viewable in any angle by zooming in/out, rotation, and via translation tools, which was built in MIUE, was used by the clinician to locate the tumor in the pre-operative stage, and select the biopsy plane. The probe then automatically moved to the biopsy plane under the guidance of the robotic arm. From that point, real-time ultrasound images, containing the image of the injected simulated tumor, which is tracked by the motion tracking algorithm described in chapter 2 for the in-vivo experiment, and the trajectory of the needle, were continuously shown on the screen for needle guidance.

Once the clinician located the simulated tumor on the computer and selected the orientation of the biopsy needle in the 2D image plane, the biopsy procedure was guided and accomplished by the needle holder. Note that before delivering the biopsy in this in-vivo experiment, we still needed to cut the abdominal skin of the micropig at the biopsy point selected by the clinician, to ease the insertion of the biopsy needle. Without this additional action, the biopsy needle would have been bent, due to the thrust force (Figure 5.9). Figure 5.10 depicts the biopsy procedure in the ex-vivo and in-vivo experiments. Only one biopsy attempt was made for each injection area. All

specimens were analyzed carefully after each attempted biopsy, to ascertain whether or not they were successful.

Figure 5.9 Biopsy attempt without cutting the abdominal skin of the micropig. The red circle shows the bending of the biopsy needle during insertion

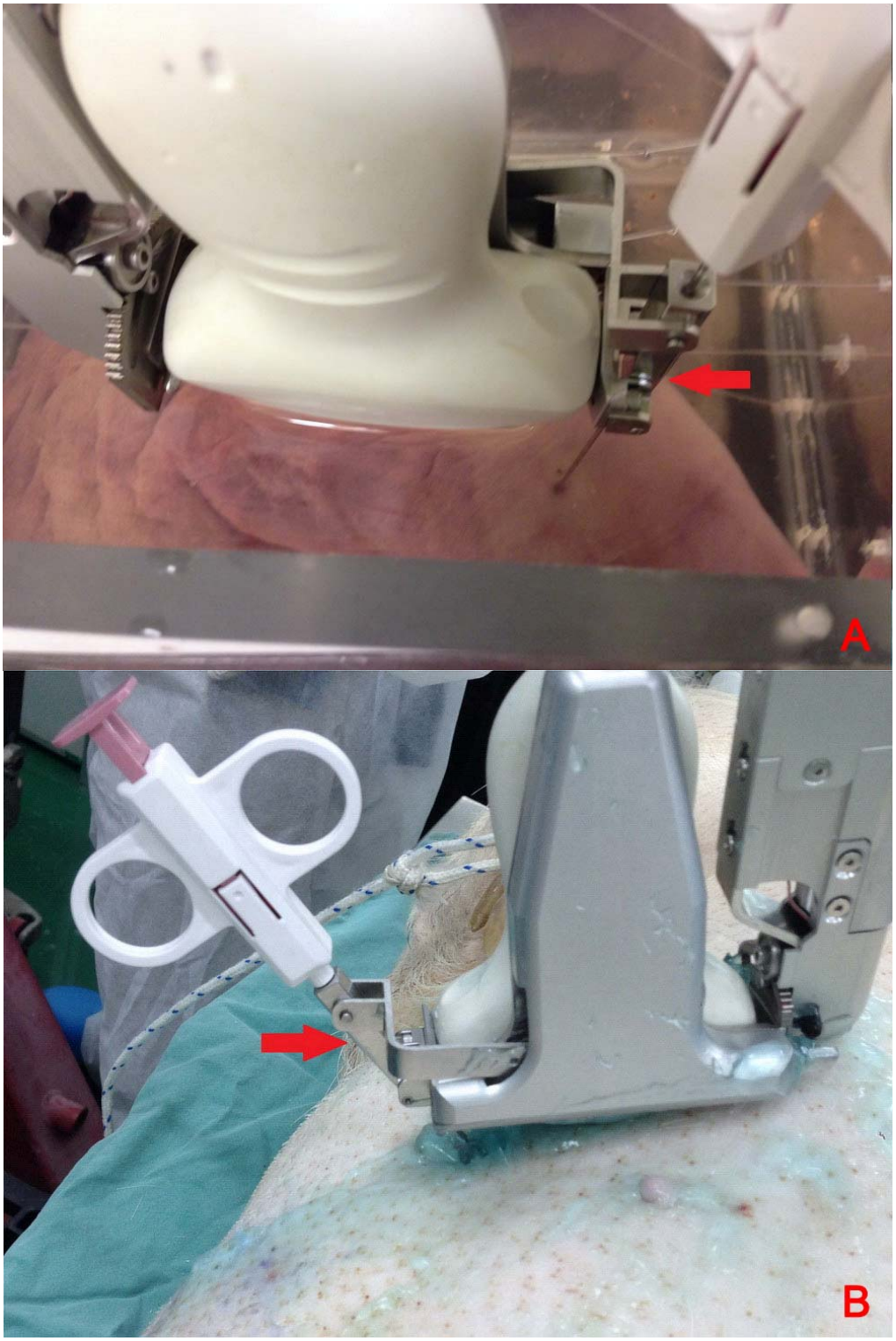

Figure 5.10 Delivering the biopsy with the needle holder. A: ex-vivo experiment; B: in-vivo experiment. Red arrows: the needle holder.

Euthanasia of the micropig was carried out after the in-vivo experiment. This was done via intravenous injection of pentobarbital (150mg/kg). This

method is humane, practical, and suitable for micropigs. The liver was then extracted for further investigation.

5.4 Results

5.4.1 Results of biopsies

Each biopsy attempt was either described as a success (meaning the clinician successfully obtained a simulated tumor sample, which appeared in a green/white/blue color in the biopsy needle) or a failure (the clinician only obtained a liver tissue sample in the biopsy needle). In the ex-vivo experiment, for the Vaseline-based simulated tumors with barium sulfate, the clinician successfully obtained simulated tumor samples in all 10 attempts (10/10); for the Vaseline-based simulated tumors without barium sulfate, the clinician successfully hit the simulated tumors in 7 attempts (7/10); and for the agar-based simulated tumor, the clinician successfully hit the simulated tumor in 6 attempts (6/10). In the in-vivo experiment, the clinician obtained the simulated tumor in 2 attempts (2/3). Figure 5.11 shows the visual appearance of the injected simulated tumors after the ex-vivo and in-vivo experiments. Figure 5.12 shows the proof of visual checks on three successful biopsy attempts from the ex-vivo and in-vivo experiments.

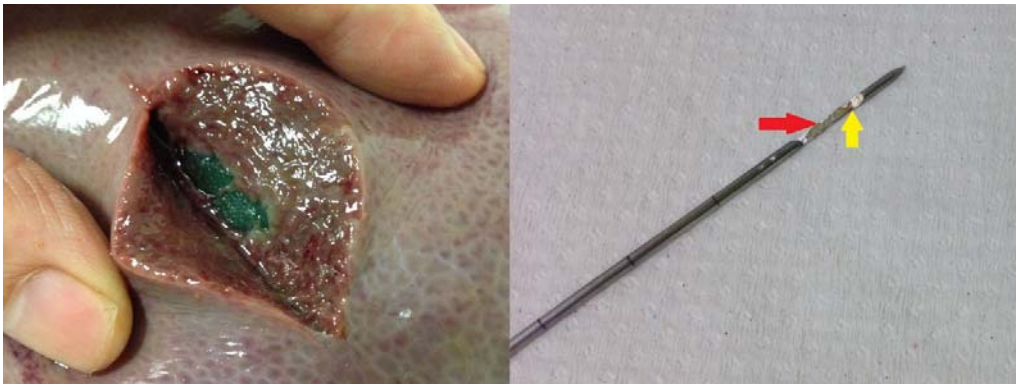

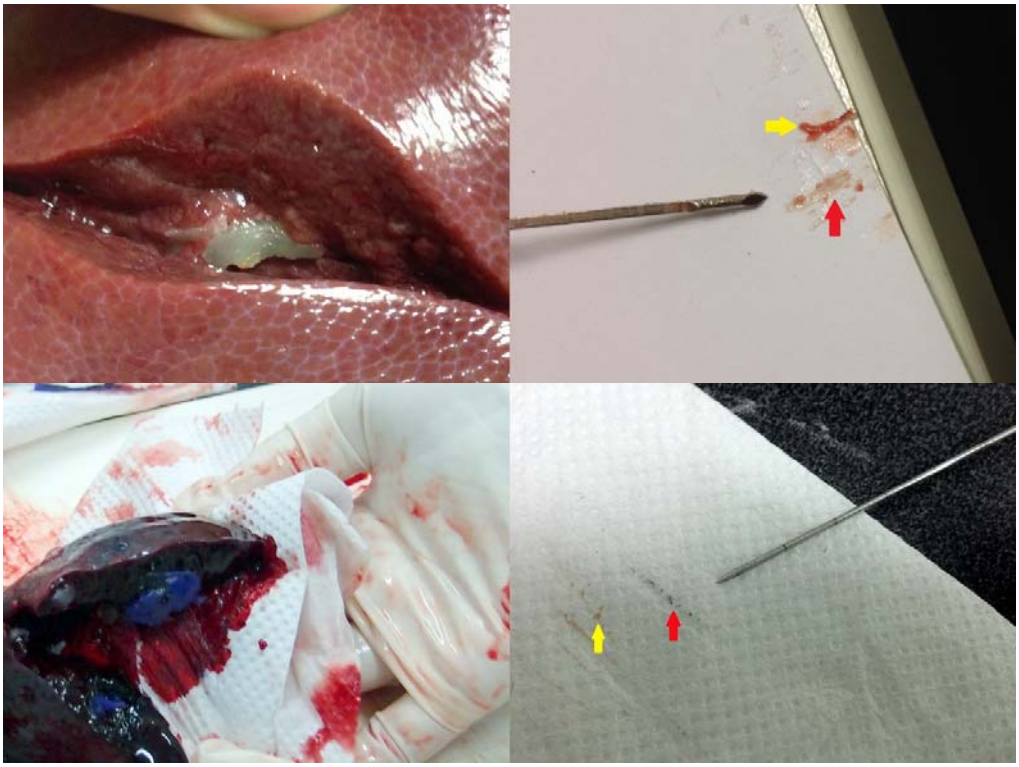

Figure 5.11 View on gross pathology of injected simulated tumors (left column), and successful biopsy attempts on injected simulated tumors (right column). Top row: an agar-based simulated tumor; Middle and bottom row: Vaseline-based simulated tumors with barium sulfate, in ex-vivo and in-vivo experiment, respectively.

5.4.2 Comparison of ultrasound image of the target area

Tumor location and planned targeting are key to a successful biopsy attempt, and these are clearly affected by the ultrasound image of the simulated tumor area.

During the biopsy procedure, we observed a ‘shadow’ phenomenon with the images of the Vaseline-based simulated tumors with barium sulfate, which assisted the clinician in determining tumor location. Based on the results of the experiments, the position above the top of the ‘shadow’ area could be confirmed as the location of the simulated tumor (target). Figures 5.12 and

5.13 show this phenomenon and the real-time ultrasound image comparison between simulated tumors with and without barium sulfate.

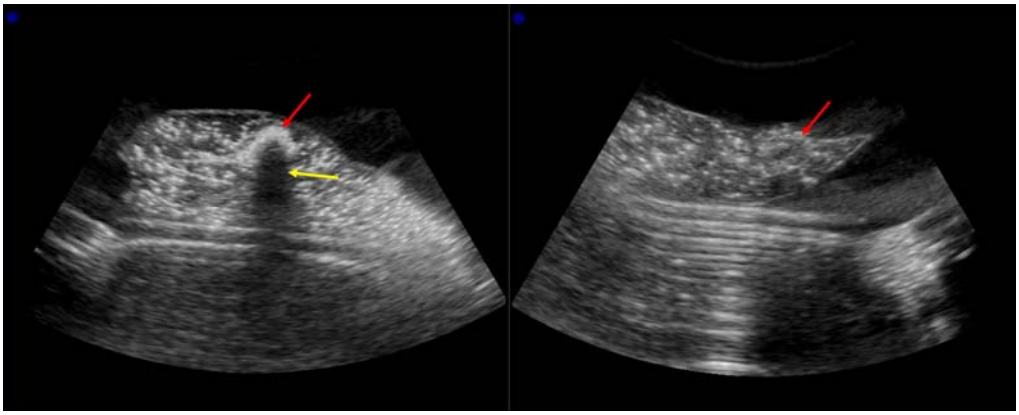

Figure 5.12 Comparison between real-time ultrasound images of simulated tumors with/without barium sulfate. Left: Vaseline-based simulated tumor with barium sulfate; right: agar-based simulated tumor. Red arrow: location of target; Yellow arrow: 'shadow' phenomenon.

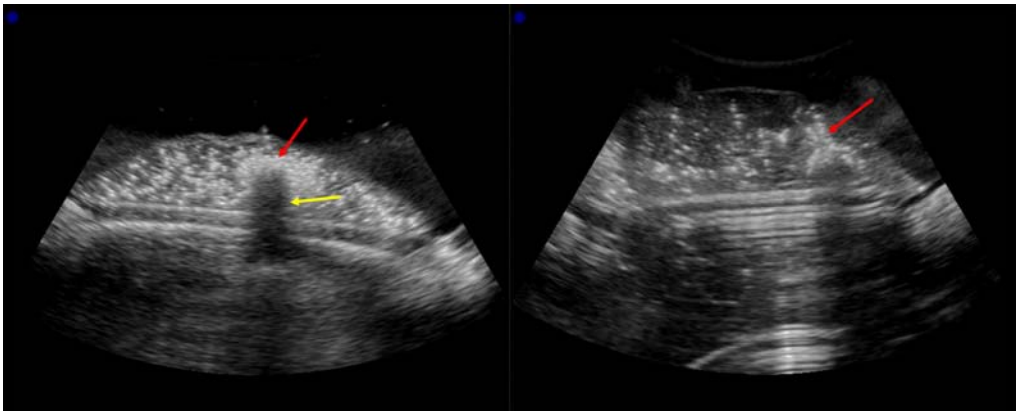

Figure 5.13 Comparison between real-time ultrasound images of simulated tumors with/without barium sulfate. Left: Vaseline-based simulated tumor with barium sulfate; right: Vaseline-based simulated tumor without barium sulfate. Red arrow: location of target; Yellow arrow: 'shadow' phenomenon.

5.4.3 Quantitative analysis of the injection

The size of the simulated tumors is related to the amount of mixture injected. After biopsy, the porcine livers were bisected and the diameter of the simulated tumors was measured. Table 5.1 shows the volumes of injected

material used, and the resultant tumors' diameter. Note that the simulated tumors were not perfectly spherical, but more elliptical in appearance.

Table 5.1 Average tumor size from the injected mixtures.

Number of injections	Volume of injection (ml)	Average simulated tumor size (diameter / cm)
6	2	1.61
6	3	1.85
6	5	2.20
6	8	2.57
6	10	2.78

Moreover, for the Vaseline-based simulated tumors with barium sulfate, the amount of injected material and the size of the simulated tumor were also related to the size of the 'shadow', as discussed above. This is illustrated in Figure 5.14.

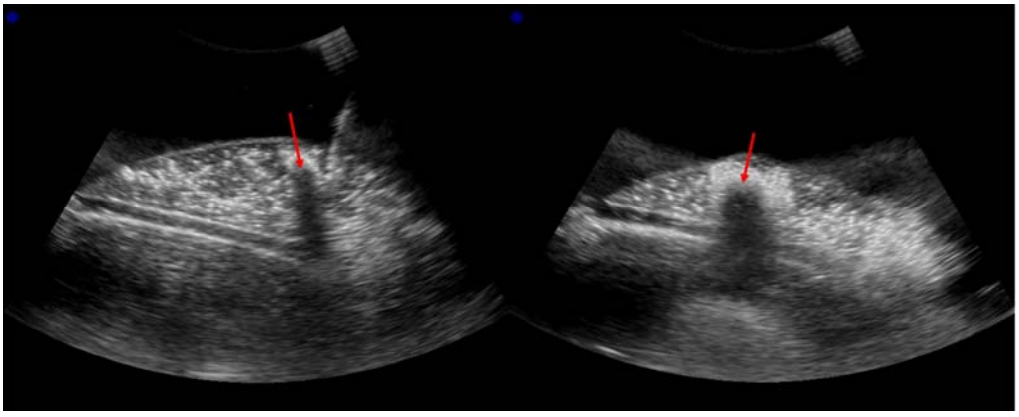

Figure 5.14 Comparison of the 'shadow' size for different amounts of injected material. Left: 3 ml of mixture injected; right: 10 ml of mixture injected.

5.5 Discussion

In the ex-vivo experiment, failed biopsy attempts were more commonly from the smallest, 2 ml or 3 ml injections, so it is obvious that bigger size in the injected simulated tumors facilitates biopsy. Since the porcine livers were not fixed in the plastic box, when the biopsy needle touched the surface of the livers or during the insertion process, the deformation of liver tissue or displacement of simulated tumors could occur, which could possibly affect or fail the biopsy trial. According to the results of the ex-vivo experiments, the highest successful biopsy rate (100%) on our proposed Vaseline-based material suggests the most useful image aid of the simulated tumor area, which also matches the feedback from the clinician.

It is worth noticing that we only observed the ‘shadow’ phenomenon from the images of Vaseline-based simulated tumor with barium sulfate, so we think it has nothing to do with the air bubbles, otherwise we should have observed it from the images of Vaseline-based simulated tumor without barium sulfate or agar-based simulated tumor too. The possible reason for this ‘shadow’ phenomenon could have been the mixture of barium and Vaseline, which could be the source of attenuation on US image in this case.

Biopsy in live animals (in-vivo) is much more difficult than ex-vivo biopsy, for a variety of reasons – and this was apparent in this particular case. First, the image quality of the liver and target areas is usually considerably poorer than those acquired ex-vivo. Second, there is a higher requirement for the fast and accurate insertion of the biopsy needle. With the micropig, we had to ensure it penetrated through the thick skin and subcutaneous tissue of the

animal within the pre-selected path. The deformation of liver tissue and displacement of simulated tumors caused by the biopsy needle are still harder to detect on the ultrasound image than in ex-vivo, during the insertion process. Third, the periodic respiration of the micropig under ventilator resulted in the deformation of the liver area, making both injection of the simulated tumors and insertion of the biopsy needle, more difficult. The successful biopsy rate in the live animal experiment with our proposed Vaseline-based simulated tumors with barium sulfate as targets was 66.7% (2/3). After the liver was extracted from the micropig's carcass, we found that the clinician had injected one out of the three mixtures into the animal's spleen instead of its liver. This is the reason that led to the failed attempt in the in-vivo experiment.

This study evaluated the utility of various mixtures to simulate intrahepatic tumors, and demonstrated that these can be used for targeting studies, because the clinicians can successfully locate the target in the experiment precisely and easily, under the same routine they performed to locate real tumors in real medical applications in the hospital everyday. The ultrasound properties of our proposed material are similar to those of real tumor tissues. During preparation of the tumor mixture, it is critical to maintain the mixture in a liquid or semi-fluid state prior to injection, and to ensure the mixture can solidify after injection to form a discrete tumor. From both the ex-vivo and in-vivo experiments, we have proved that the Vaseline-based simulated tumor can maintain its size and position after injection. The Vaseline-based model has the following advantages when compared to the more widely-used agar-based model: (1) There is less requirement for temperature control; (2) The average time for the preparation of the Vaseline-based mixture is 6-8 minutes at most,

while preparing the same amount of agar-based mixture takes 15-20 minutes; (3) The agar-based mixture must be injected above about 45 ℃; the Vaseline-based mixture can be injected at room temperature. This is important because live animal experiments require fast injection of the simulated tumor, when the clinician finds a suitable site via the real-time ultrasound under animal respiration. Unfortunately, temperature control of the mixtures takes time, and makes the injection more difficult in the case of agar-based material; (4) The Vaseline-based mixture is much easier to inject, as it is less viscous, and minimal pressure needs to be applied. On the other hand, the agar-based mixture is viscous and solidifies rapidly when the needle makes contact with the cold water or porcine liver tissue, making the injection process more laborious and less controlled; (5) Since our ex-vivo simulated tumor was originally developed as a tool to validate our robotic biopsy system, ensuring that the ultrasound image of the simulated tumor is adequate for real-time biopsy is essential. We have demonstrated that the so-called 'shadow' phenomenon can be seen on the real-time ultrasound images of Vaseline-based simulated tumors with barium sulfate. This is helpful for the clinician in accurately localizing the biopsy target. More importantly, even when the real-time ultrasound image quality of the simulated tumor itself was not satisfactory, in some attempts in the ex-vivo and in-vivo experiments, as is often seen in clinical applications, this method (locating the target by the 'shadow') still worked.

For the above reasons, we assert the more widely-used agar-based simulated tumor is less suitable than our proposed Vaseline-based simulated tumor here

for both ex-vivo and live animal (in-vivo) experiments. The materials used in our study are easily prepared and can be bought at low cost. All the materials are non-toxic.

Finally, the live animal experiment described in this chapter is a great example to show how the techniques we proposed in this thesis work together to help the clinicians perform the biopsy. Specifically, first of all, the clinicians injected simulated liver tumor inside the liver of the animal to create the biopsy target (chapter 5). Next, we applied fan-shape scan on the biopsy area under the control of probe holder, and generated a respiration-corrected 4D animal liver model for the clinicians to locate the tumor in the pre-operative stage, and selected the biopsy plane (chapter 3). After that, real-time ultrasound images, containing the image of the injected simulated tumor, which was tracked by the motion tracking algorithm, and the trajectory of the needle, were continuously shown on the screen for needle guidance (chapter 2). Finally, the biopsy procedure, which had been experienced by the clinicians in the phantom experiment before, was guided and accomplished by the needle holder (chapter 4). As mentioned in the chapter 1, respiratory liver motion is a complicated issue to be solved, and works should be done in multiple aspects, such that we have developed several related techniques, and described them in various chapters. From this experiment, the connectivity of various chapters is clearly shown.

5.6 Limitations

For the limitation of this proposed work, it is worth mentioning that the biological properties of the proposed Vaseline-based mixture materials are far

from those of real tumor tissue, so proof the functionality of our developing guidance system on the proposed Vaseline-based mixture material via the ex-vivo and in-vivo experiments does not guarantee its outcome in real medical biopsy, if the real liver lesions (targets) appear not as clear. However, it is not our goal to create a kind of simulated tumor mixture whose biological properties have to be similar to those of real tumors. In fact, our goal is to develop a practical and easy way to create simulated (injectable) tumor inside liver, which is visually similar to real tumors, and make sure it can be most easily located in ultrasound image. We need solid evidence to prove a successful or unsuccessful biopsy attempt, such that we know whether our tracking algorithm is accurate enough to guide the biopsy, or whether the mechanical module of the biopsy system is precise enough to guide the biopsy needle. The basic requirement for this simulated target is that it must be visually differentiable in US image, and we have proved that the proposed Vaseline-based mixture material with barium sulfate provides the best visual guidance during biopsy when compared to other selected materials. Whether it biologically being similar to the real tumors or not, is none of our concern in this chapter.

5.7 Conclusion

The described Vaseline-based mixture is a novel approach to creating solid intrahepatic simulated tumors. When compared with the more widely-used agar-based method, it offers various advantages. This model offers a valuable adjunct in the development and assessment of novel, minimally invasive surgical techniques.

CHAPTER 6. SUPPLEMENTARY WORK: A QUANTITATIVE EVALUATION FUNCTION FOR 3D TREE-LIKE STRUCTURE SEGMENTATIONS IN LIVER IMAGES

The analysis of vascular structure from volumetric datasets plays a crucial role in many medical applications. This Chapter describes a supplementary work, on quantitative evaluation of vascular segmentations in liver images. The significance of this work is discussed.

The following was first published in: ***C Li****, J Wu, Y Chi, J Liu, Q Tian, H Yu, 'A quantitative evaluation function for 3D tree-like structure segmentations in liver images,' Computer Methods in Biomechanics and Biomedical Engineering: Imaging & Visualization, pp. 1-9, 2014.*

6.1 Introduction

Nowadays, an accurate analysis of human organ vascular system in volumetric image data is gaining increasing importance for a wide variety of medical applications. Precise knowledge of the morphology and structure of human organ vascular system allows for quantitative diagnosis, surgical planning, surgical navigation and outcome assessment, as well as for monitoring of the progression of vascular diseases [154].

Although many algorithms have been designed for vessel segmentations in different organs such as liver [155-165] and lung [166-171], there has been no clear investigation about evaluating the effectiveness of these algorithms, especially in 3D situations. In most cases, the evaluation section of vessel segmentations in any organ has not been emphasized, or the quality of the results is only manually assessed by the specialists, which sometimes is too subjective. Without clear evaluating rules of various segmentation results, researchers will have difficulties in improving their segmentation algorithms. Moreover, keeping consistent high quality of manual evaluation on large scale of segmentation results is always impossible due to time and energy limitation of human being, so it is important to find an effective and generally applicable method to achieve automatic evaluation on various tree-like structure segmentation data.

In order to investigate automatic evaluation algorithms for such purpose, we have also looked into the retinal vessel segmentation area, where most of the evaluation methods are only suitable for 2D cases, but the evaluation issue is much more emphasized [172-175]. To our best knowledge, the evaluation of

these vessel segmentation algorithms has been conducted by using general pixel (2D) based measures (or known as binary image similarity measures) such as the accuracy (Acc), sensitivity (Se), specificity (Sp), or on the other hand, by using distance based measures (in 2D) like mean squared error distance (MSE), Hausdorff distance (H) [176], and figure-of-merit (FOM) [177]. However, pixel(2D)/voxel(3D) based measures only make use of the number of correctly and incorrectly classified pixels/voxels, while distance based measures utilize the position of mis-segmented pixels, but most of them are not suitable in 3D cases due to the limitation of the method itself or huge computing cost. Moreover, most of those methods are used without taking into account the subjects' properties of structure or topology, which in this case is the 3D tree-like structure of the liver vessels. For the methods that have taken into account subjects' properties of structure or topology, they are all dealing with the 2D segmentation cases, thus none of them are very suitable for the evaluation of vessel segmentations in 3D situations. Gegúndez-Arias proposed a function for quality evaluation of retinal vessel segmentations (2D) [174], which used three independent metrics to describe the retinal vessel features and assess the overall quality of segmentation results based on the value of these three metrics. But directly applying their method into 3D cases will face difficulties such as 2D-based theoretic limitations and huge computational cost from morphological operators on the 3D vessel trees volume. Inspired by their approach, we developed four independent metrics, and made them suitable in 3D situations by providing more efficient calculations. Generally speaking, one quantitative function to achieve the evaluation of overall qualities of segmentation results is not always possible,

and we believe the design of several independent metrics to evaluate their respective properties of the segmentation results is necessary and a proper way to accomplish this task.

In this study, we propose a quantitative evaluation function enables general vascular segmentation assessment based on its tree-like structure. Specifically, four independent metrics focusing on the connectivity, overall shape/correctness, skeleton structure, and branches structure error of the tested 3D volume make this function sensitive to tree-like structure features. On the other hand, this is a general evaluation method suitable for any algorithms aiming at 3D tree-like structure segmentations in liver images with large scale of testing data. Moreover, it may be regarded as a helpful guideline for improving or adjusting the performance of 3D tree-like structure segmentation algorithms, especially for those involved with parameters, because larger function value suggests better parameters settings of the algorithms.

6.2 Description of QEF

This QEF is based on four independent metrics aiming at evaluating four different aspects of vascular tree features of segmentation results with respect to their corresponding ground truth. The selected features can be considered as key factors of any tree-like structure.

Figure 6.1 below shows how this QEF works. The input of the evaluation function is the segmented data by any segmentation algorithm to be valuated, and the output is the result of QEF

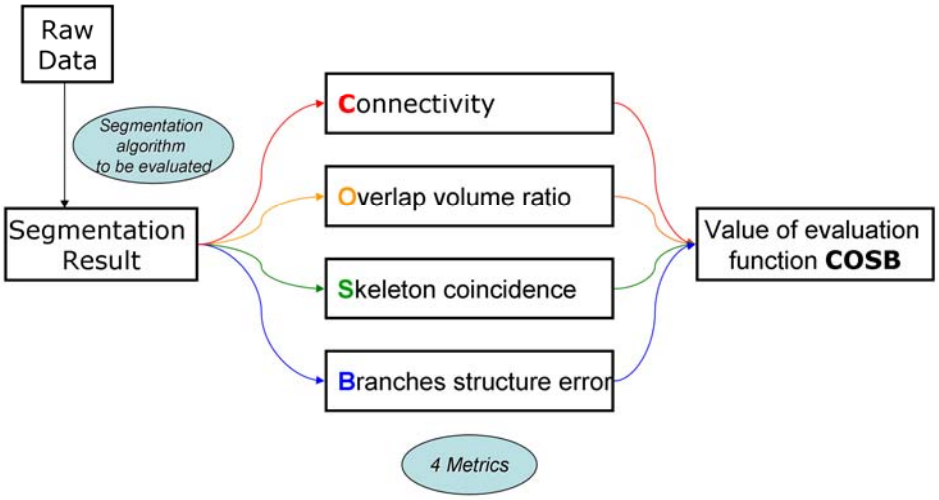

Figure 6.1 Flow-chart to show how this quantitative evaluation function works.

Here, denoting S as the segmentation result to be evaluated, and S_g as the reference segmentation ground truth, these four metrics are defined within the [0, 1] interval as follows.

- Connectivity (C): This metric assesses the fragmentation degree between segmentation result and reference segmentation ground truth. Since the vascular tree should be a connected structure, proper vascular segmentation is expected to have only few connected components (ignore the capillary network, ideally two for the liver veins: one for portal vein tree, the other for hepatic vein tree). This metric compares the number of connected components in S and S_g with regard to the total number of segmented voxels in S_g [174].

  Mathematically, it is defined as

$$C(S, S_g) = 1 - \min\left\{1, \frac{|*C(S_g) - *C(S)|}{\# S_g}\right\} \quad (6.1)$$

where min is the minimum function, $*C(S_g)$ and $*C(S)$ stand for the number of connected components in S_g and S, respectively, and $\# S_g$ denotes the cardinality of S_g. For the purpose of simplicity, segmentation is referred to the set of vessel voxels exclusively, which means the set of background voxels is excluded.

- Overlap Volume Ratio (O): The calculation of the overlap ratio between segmentation result and reference segmentation ground truth is a direct and effective way to assess the quality of segmentation results. Obviously, higher overlap volume ratio indicates higher matching degree of the segmentation result and reference segmentation ground truth. This metric, based on the Jaccard coefficient [178], evaluates the overall shape/correctness of the segmentation result. It is defined as

$$O(S, S_g) = \frac{\#\left(S \cap S_g + \frac{1}{2}\left((S \setminus S_g) + (S_g \setminus S)\right)\right)}{\#(S \cup S_g)} \quad (6.2)$$

where \ is the intersection operator. For example, A\B is the set of all object voxels belonging to A but not B.

- Skeleton Coincidence (S): Skeleton represents the key structure of 3D volume. In some extreme cases as shown in Figure 6.2, the overlap volume ratio of two volumes could be high, but their skeletons could be significantly different. So it is necessary to identify this kind of

extreme cases by comparing the skeleton volume of S and S_g. This metric, partially based on Jaccard coefficient (Jaccard, 1901), measures the skeleton overlap volume ratio between segmentation result and reference segmentation ground truth. It is defined as

$$S(S, S_g) = \frac{\#\left(\left(sv(S) \cap S_g\right) \cup \left(S \cap sv(S_g)\right)\right)}{\#\left(sv(S) \cup sv(S_g)\right)} \tag{6.3}$$

where sv(A) represents the skeleton volume of A.

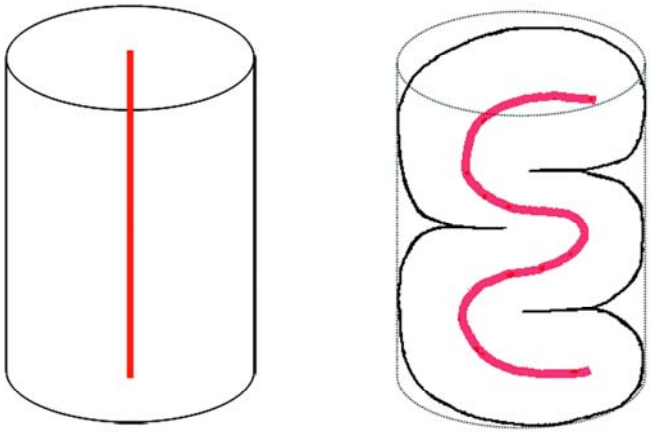

Figure 6.2 One example to showcase the situation where the overlap volume ratio of two volumes is high, but their skeletons are significantly different. Red line (with width) represents the skeleton of the volume.

- Branches Structure Error (B): This metric evaluates the structure error of each identified branch piece between segmentation result and reference segmentation ground truth at different branch level. For lower branch level branch pieces, the structure error contributes more to the total error calculation, because they are the main parts of the vessel tree and of important interest to clinicians. The metric is defined as

$$B(S,S_g)=1-\min\left\{1,\sum_i\sum_j\left(\frac{\left|DS_{ij}-DS_{gij}\right|}{2^{i-1}\times DS_{gij}}\right)\right\} \quad (6.4)$$

where DS and DS_g represent the diameter of branch piece of segmentation result and reference segmentation ground truth respectively; i is the branch level; j is the branch ID number of each branch at certain branch level. Note that when calculate this metric, the root points of the vessel trees need to be manually selected.

Figure 6.3 shows the branch level division and branch pieces of a typical tree-like structure.

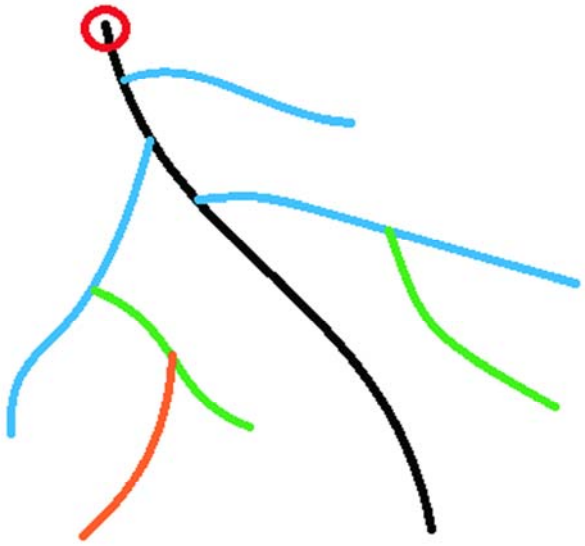

Figure 6.3 Branch level division of a typical tree-like structure: Red circle identify the root of this tree; Black color branch: level 1 (i=1); Blue color branch: level 2 (i=2); Green color branch: level 3 (i=3); Orange color branch: level 4 (i=4).

According to these four independent metrics, a function f is defined to be monotonically increasing as

$$x_i \geq y_i, i = 1,2,3,4 \Rightarrow f(x_1, x_2, x_3, x_4) \geq f(y_1, y_2, y_3, y_4) \quad (6.5)$$

where

$$f(C, O, S, B) = C \times O \times S \times B = COSB \in [0,1] \quad (6.6)$$

The product of these four independent metrics C, O, S and B was chosen here because it preserves equal weight of each metric in f. This definition indicates that those four metrics are equally important. The extreme f values 0 and 1 denote the worst and best segmentation results, respectively.

6.3 Validation of QEF

This subsection shows one example of how COSB performs on one set of liver vessel segmentation data. This example illustrates and highlights certain outstanding properties of our QEF, and can be considered to serve the purpose of verifying its validity as well. Here, the segmentation results have been visualized using MIUE [114].

The testing example used in this section, as shown in Figure 6.4 (A)-(D), are the segmentation results from same contrast enhanced CT-Scan data, while Figure 6.4(A) was generated by a medical imaging specialist with ten-years experiences using MIUE [114] and verified by a radiologist. Specifically, the medical imaging specialist generated an initial result by segmenting a CT volume using image processing techniques, e.g. thresholding. The radiologist compared the segmented result with the CT scan and gave the advices on how to improve the initial result. Accordingly, the medical imaging specialist revised it manually using image edit tools. The result was not revised until it

was accepted by the radiologist. The final verified result becomes the ground truth. Figure 6.4 (B)-(D) were generated using context-based voting algorithm [179] under different thresholds.

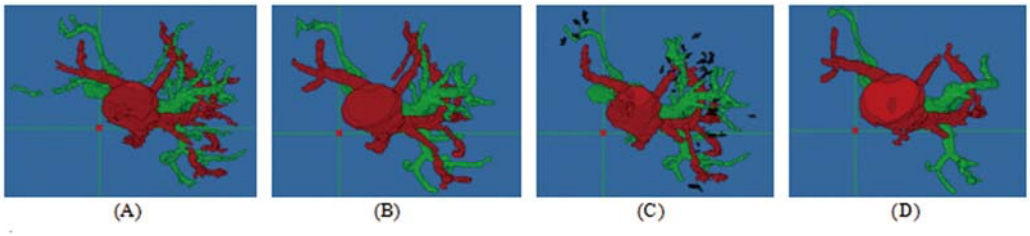

Figure 6.4 One example of segmentation results to show the properties of COSB and for its validation. (A): Reference-standard. (B)-(D): Segmentation results under different threshold setting. In red color: hepatic vein; green color: portal vein; black color in (C): ungrouped vessel pieces.

The metrics of C, O, S, B, and function f, expressed in (1)–(4), and (6), respectively, were calculated for volume (B), (C), and (D), taking volume (A) as reference segmentation ground truth. The values obtained are presented in Table 6.1, and show significantly differences between the tested segmented volumes. From the figure we can see that volume (B) is very similar to reference volume (A), since it has high matching degree of the hepatic and portal vein volume with the reference standard ground truth, so (B) got the biggest values in O, S and B among the three tested volume. In terms of vessel detection and extraction, the result of (B) and (C) are close to each other. However, we intentionally kept some ungrouped vessel pieces in (C), which results in (C)'s lower value in metric C (Connectivity) when compares with (B). On the other hand, although (D)'s property of connectivity is very nice (metric C=1), there are many portal and hepatic vessel branches missing in (D).

Those are key loss of a vessel segmentation result, and thus result in the lowest COSB value (0.42) for (D), because three (O, S and B) out of four measured features have been penalized. In this way, based on the value of COSB, we can evaluate the quality of 3D tree-like structure segmentation results quantitatively.

Table 6.1 Quality evaluation values for the vessel segmentation shown in Figure 6.3(B)-(D) taking (A) as reference standard ground truth

Segmented Volume	C	O	S	B	COSB
B	0.99	0.79	0.83	0.98	0.63
C	0.98	0.78	0.80	0.98	0.60
D	1	0.64	0.71	0.93	0.42

In addition, making use of this example, we can also obtain the connection between COSB values and human scored evaluation results. A group of 20 human observers (Scientists, post-docs, research engineers at Singapore Bio-Image Consortium (SBIC), Agency for Science, Technology and Research (A*STAR), Singapore, and graduate students from Department of Biomedical Engineering / Department of Electrical and Computer Engineering / School of Computing, National University of Singapore (NUS)) were asked to rank the quality of volume Figure 6.4 (B)–(D) with respect to the reference standard volume Figure 6.4 (A). Here we asked them to focus on the differences of volume. In the end, all the human observers evaluated volume (B) as the best segmentation, and volume (D) as the worst. This human observation result can

be explained by the facts that the segmentation of volume (B) preserves most of the vessel details visualized in reference standard volume (A) while, on the contrary, (D) keeps the least. On the other hand, although (C) was affected by the ungrouped vessel pieces, it was still considered more valuable than segmentation of volume (D) because the fact that there are key vessels missing in segmentation (D) degrades the visual perception of quality more than those ungrouped vessel pieces in (C). As shown by the values in Table 6.1, this human observation result matches the calculation of COSB results. Moreover, this session can be regarded as the training session for the following main experiments as well.

6.4 Experimental Results and Discussion

The example presented in the section of validation of QEF proves that the values of COSB on testing liver vessel segmentations have abilities to show good correlation with human quality perception. In this section, we calculate the value of COSB and other widely-used QEFs including sensitivity (Se), specificity (Sp), and accuracy (Acc) on real liver vessel segmentation datasets to compare their respective matching degree with human quality perception. Obviously, the function which provides the best correlation with human quality perception can be considered as the best evaluation function for this assessment task.

The procedure applied in this section can be summarized as follows. Eight liver vessel segmentation results generated using context-based voting algorithm [179] under optimized threshold were selected for the experiment. Same group of 20 human observers were asked to score the quality of liver

vessel segmentation results compared with their respective reference ground truth within the [0, 1] interval, where 0 and 1 denote the worst and best quality of the results, respectively. By doing this, human scores (HS) for the segmentation results representing subjective human quality perception can be obtained. Next, the values of COSB and other QEFs were calculated for the same segmentation results as well. Finally, all the values of QEFs and human scores were compared to measure the matching degree between them, and in this way, the correlation between the performance of subjective evaluation (provided by HS) and performance of objective evaluation (provided by QEFs) can be obtained.

Figure 6.5 shows the set of liver vessel segmentation results corresponding to their respective ground truth used for the experimentation. In the first and third columns ‘CT01-08_GT’ represent the ground truth generated by a medical imaging specialist with ten-years experiences using MIUE [114] and verified by a radiologist, while in the second and fourth columns ‘CT01-8_Rst’ represent their respectively segmentation results. According to the analysis of 20 human observers, the performance of the segmentation algorithm under different thresholds on the selected data can be briefly summarized as follow.

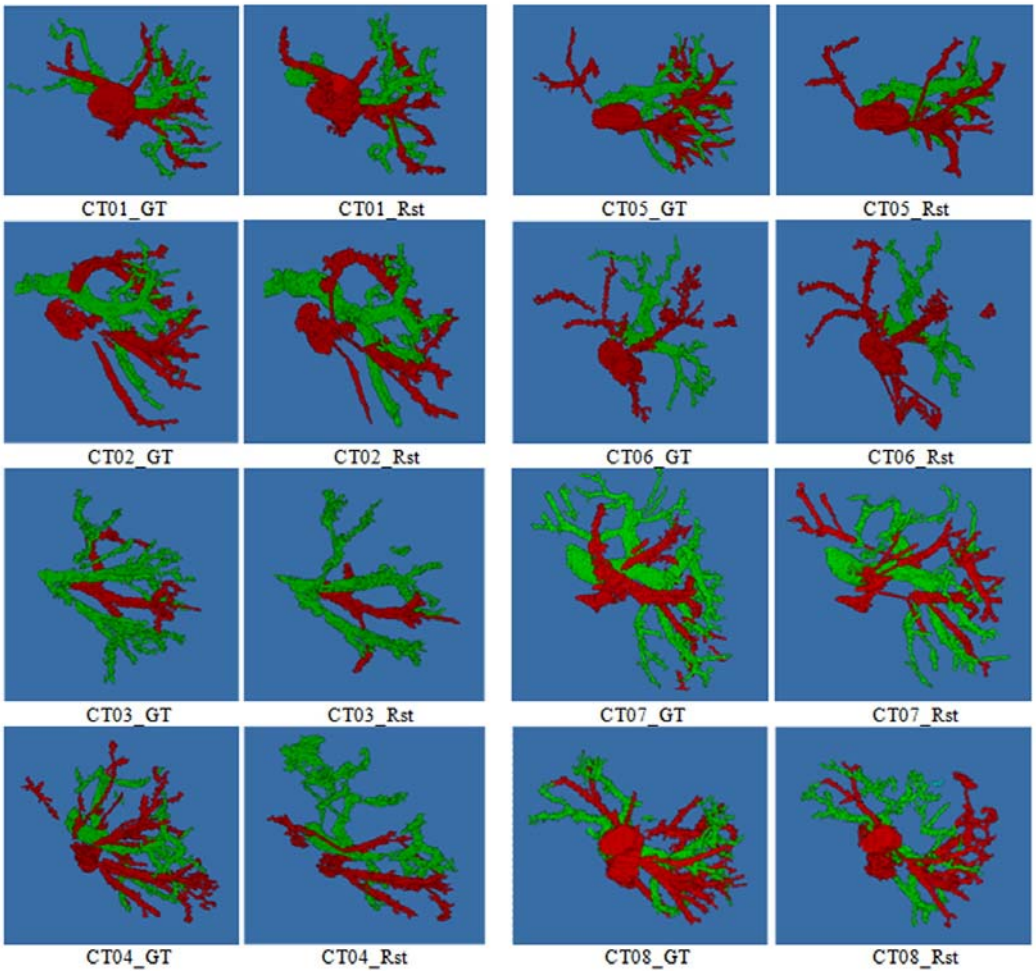

Figure 6.5 Eight groups of liver vessel segmentation results to test the performance of COSB and other commonly-used QEFs (Se, Sp, Acc). CT01-08_GT: Reference-standard ground truth. CT01-08_Rst: Segmentation results using context-based voting algorithm. In red color: hepatic vein; green color: portal vein.

CT01_Rst: performed very well in portal vein, but missed some vessel details at the tip-end. The segmentation algorithm grouped some hepatic vein as portal vein.

CT02_Rst: performed better in portal vein than in hepatic vein. Some missing vessel voxels observed near the hepatic vein tree root point area.

CT03_Rst: performed better in portal vein than in hepatic vein, but missed some vessel details at the tip-end of portal vein. The segmentation of the hepatic vein was not so good, because one of the main branches was missing.

CT04_Rst: performed poorly in both portal vein and hepatic vein. The segmentation algorithm failed to extract the proper vessel shape. When compared with the origin CT scan data, we found that the poor performance area was actually affected by the tumor.

CT05_Rst: missed some vessel details at the tip-end of both hepatic and portal vein. The middle upper area was affected by the tumor.

CT06_Rst: performed better in hepatic vein than in portal vein. Some vessel details at the tip-end of portal vein are missing. The middle lower area was affected by the tumor.

CT07_Rst: performed poorly in middle upper part of portal vein and hepatic vein, as well as the area near the hepatic vein tree root point. Some hepatic vein found in the upper left area was found being grouped wrongly.

CT08_Rst: did not perform well in the middle upper area of both portal vein and hepatic vein. The performance of lower area was better.

The results of the experiment are presented in Table 6.2. From the table we can see that the Se, Sp, Acc values of those eight tested data are quite close, and more importantly, without a clear order that can suggest the segmentation qualities of the data. In other words, if the doctors or medical image users only analyze the value of Se, Sp, or Acc, it is very hard for them to assess the qualities of segmentation results, or decide which segmentation result should be the best or the worst. On the other hand, the values of COSB show

significant differences between the eight groups of tested data. This table also shows the average value of the human scores (HS) given by the 20 human observers for each segmentation results in the last column. When comparing the COSB values with the average human scores (HS), we found they are highly matched. The calculation shows that the COSB values are very close to the HS values, and the average value of relative errors is only 7.3% over all the 8 datasets. However, the Sp or Acc values did not show much relevance to the average human scores. Note that the Se value also showed some correlation between the averaging human scores (HS), but the average value of relative errors is 20.5% over all the 8 datasets, which is much larger than COSB.

Table 6.2 Quality evaluation values for the vessel segmentation shown in Figure 6.4. [a] R: Resolution, D: Dimension, [b] Se: sensitivity, Sp: specificity, Acc: accuracy.

Segmented Volume	[b] Se	[b] Sp	[b] Acc	C	O	S	B	COSB	HS
CT01 [a] R:0.67×0.67×3.0 [a] D:512×512×61	0.78	0.99	0.98	0.99	0.82	0.87	0.96	0.68	0.71
CT02 R:0.59×0.59×3.0 D:512×512×83	0.71	0.98	0.98	0.98	0.78	0.85	0.94	0.61	0.65
CT03 R:0.71×0.71×3.0 D:512×512×64	0.74	0.99	0.98	0.99	0.76	0.71	0.97	0.52	0.54
CT04 R:0.67×0.67×3.0 D:512×512×55	0.56	0.98	0.96	0.97	0.71	0.72	0.90	0.45	0.40
CT05 R:0.62×0.62×3.0 D:512×512×54	0.64	0.99	0.98	0.98	0.75	0.76	0.95	0.53	0.58
CT06 R:0.61×0.61×3.0 D:512×512×44	0.72	0.98	0.97	0.97	0.75	0.80	0.94	0.55	0.63
CT07 R:0.69×0.69×1.5 D:512×512×136	0.74	0.99	0.98	0.98	0.81	0.82	0.95	0.62	0.59
CT08 R:0.77×0.77×1.5 D:512×512×280	0.79	0.99	0.97	0.97	0.80	0.84	0.94	0.61	0.67

The correlation between COSB, other QEFs and human scores denoting human quality evaluations can be also visually checked in Figure 6.6. From the figure we can see that the Acc (yellow) and Sp (brown) lines are far away from average HS (blue) line, and both COSB (pink) and Se (cyan) lines show correlation between average HS (blue) line, but COSB line is closer regarding to the overall trend.

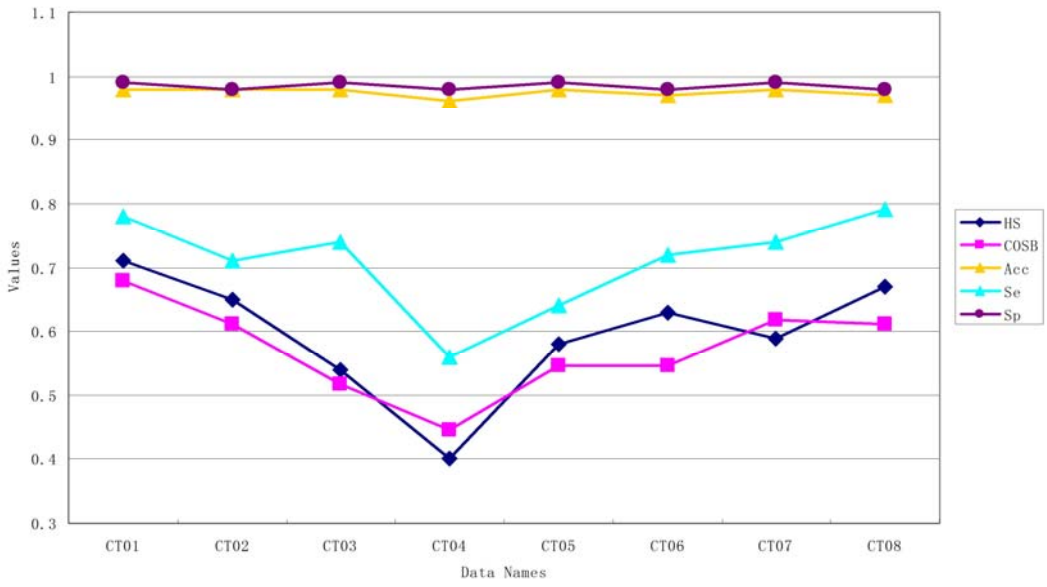

Figure 6.6 Averages of human scores (HS), Acc, Se, Sp and COSB values on eight groups of segmentation results.

Therefore, the analysis of the results in this experiment concludes that COSB provides the best correspondence with human perception when compared to the other remaining tested QEFs.

6.5 Limitations

Since this work was dealing with several patients' CT data, theoretically the real ground truth date set, which is the subject-specific liver vessel segmentations, is not available. Usually we can only make use of the manually segmented data set by the clinicians as the assumed ground truth. However, this assumed ground truth is only an approximate result due to technology limitations, operational errors, and time constraint. Although they are the best reference results we can get so far, there are still some methods to improve it. One possible way is to utilize liver vessel phantoms with known ground truth to valid a segmentation algorithm using our proposed evaluation function.

6.6 Conclusion

3D tree-like structure segmentation in human organs plays an important role in the diagnosis of organ tumors, surgical planning, surgical navigation, and other related medical applications, but only a few researchers have realized the problem of how we should evaluate the effectiveness of those numerous segmentation algorithms proposed over the past few years. In addition, in terms of US image guided biopsy application, it is also important to identify major blood vessels in liver before biopsy so that the biopsy need will not puncture them. So far, most evaluation functions have not considered the vasculature of human organs as tree-like structures with specific features, and have only been applicable to 2D situations. In this Chapter, we propose a quantitative evaluation function for 3D tree-like structure segmentations in liver images, with the purpose of overcoming the above-mentioned limitations of existing QEFs, and providing valid evaluation results. In section 6.3, this proposed function, evaluating the degree of connectivity, overlap volume ratio, skeleton coincidence, and branches structure error in a segmented volume with respect to its ground truth, has been proved to be sensitive to the structural changes in one series of segmented volume data, and to accurately reflect the quality of segmentation results with its value. From the results of all experiments in section 6.4, we conclude that COSB achieves the highest matching degree with human quality perception, when compared to other widely used quality evaluation functions, and thus is the most suitable quantitative evaluation function for 3D tree-like structure segmentations in liver images.

Although this proposed function was designed for quality evaluation in the case of segmentations in a specific 3D tree-like structure, it is very important to note that this method is independent with the segmentation algorithm applied, which means it is clearly result-oriented, focused only on the segmentation results; this means it has very high potential to be applied to any 3D segmentation algorithm evaluation. Moreover, we believe this quantitative evaluation function is also suitable for the segmentation evaluation task of other tree-like structures in the human body, such as lung vessels, bronchial vessels, cerebral blood vessels, and so on. Even for the cases to which this method may not be applicable, the applied concept of measuring descriptive features of specific structure may still be useful in designing other specialized QEFs. Furthermore, based on the different function values on the same set of data under different parameter(s) settings, COSB can suggest the best possible parameter(s) settings for optimization, as long as the segmentation algorithm applied is involved with the parameters. Finally, we think this proposed method is also a good approach for the evaluation of quality in 3D tree-like structure modeling.

In summary, the novelties of this work are listed as follows, when compare to the state of art: (1) the proposed quantitative method for evaluating the effectiveness of 3D vessel segmentation algorithms is novel [172-175]; (2) The design of evaluation metrics with consideration of vasculature of human organs as tree-like structures with specific features is novel [172-177]; (3) This proposed method is strictly result-oriented and suits for the evaluation of any tree-like structures segmentation algorithms [165-171].

CHAPTER 7. CONCLUSION AND RECOMMENDATIONS FOR FUTURE WORK

Conclusions and recommendation for future work are summarized in this Chapter.

7.1 Contributions

In this PhD project, we have developed several novel techniques for US image processing, phantom study, and experimental study parts to explore practical solutions for the respiratory liver motion issue, and hence to improve biopsy efficiency and accuracy, directly or indirectly.

First, a novel, fast, and robust respiratory signal extraction algorithm from real-time 2D ultrasound image sequences has been applied to identify the respiratory phase of the liver. This algorithm is able to extract the respiratory signal from an image sequence of 256 image frames in 5 seconds; the extracted respiratory motion near the liver boundaries and vessels area is highly consistent with the ground truth, revealing the fact that this method can also be applied in liver boundary or internal landmark tracking, by merely using a 2D ultrasound image. Considering the cost-effective requirement for most of the developing biopsy systems nowadays, our method provides a feasible solution for replacing extra commercial tracking devices. In addition, identification of the respiratory phase is useful and valuable, in enabling more complicated algorithms for further processing of the 2D US image data.

Second, a novel method for generating a subject-specific and respiration-corrected 4D ultrasound liver model has been developed. Since both the overlapping error of the liver boundary and the overall distance error of the pinpointed landmarks were within the acceptance range of clinical applications, it can be concluded that the sequences of respiration-corrected 3D image volume created by our method can precisely capture liver motion – meaning clinicians can utilize this preoperative subject-specific liver motion

information to improve diagnostic accuracy by predicting the existence, or possible position, of a tumor.

Third, a novel dynamic liver phantom, which can be applied as a liver motion simulator, has been designed for the development and validation of an image-guided biopsy system. This phantom is capable of providing stable and repeatable movement cycles under different sets of parameters, such as length of strike, and velocity of the pushing plate to simulate subject-specific respiration. With our dynamic phantom being used in experiments, some difficulties that could present themselves in the real situation of biopsy practice would very likely be reproduced and realized in advance by the researchers and engineers. This phantom not only reduces reliance on living subjects – thus avoiding the potential harm of testing devices on living subjects – but also makes it possible to conduct a large amount of tests, if needed.

In addition, a unique Vaseline-based technique for easy creation of simulated tumors of different sizes inside porcine livers has been proposed to obtain ideal testing subjects for US image-guided biopsy study. Our method offers various advantages when taking into account the time and effort required to produce a tumor model and apply it in experiments, and a successful biopsy rate on our proposed simulated tumor, when compared with the commonly used agar-based technique. All the materials needed for our method are non-toxic and can be bought at low cost. This technique offers a valuable adjunct in the development and assessment of biopsy devices and system.

In summary, the primary contributions of this thesis are listed as follows:

(1) An algorithm to extract the respiratory signal from real-time 2D US image sequences for the purpose of identifying the respiratory phase of the liver; (2) A method to generate a subject-specific and respiration-corrected 4D US liver model; (3) A dynamic liver phantom to validate an image-guide biopsy system; (4) A Vaseline-based technique for easy creation of injectable simulated tumors inside porcine livers to obtain ideal testing objects for US image-guided biopsy system at low cost .

It is also worth mentioning that with the application of above mentioned techniques, how they can help to improve the treatment of biopsy in an integrated manner. From the aspect of biopsy system design, the use of US probe arm (probe holder) helps pre-operative US image acquisition and real-time intra-operative planning and navigation as well, which, is linked to the techniques in (1) motion tracking and (2) 4D US imaging. On the other hand, the use of needle arm (needle holder) helps the clinicians to insert the biopsy needle in the experiments or during the treatment, which, is linked to techniques in (3) phantom test and (4) biopsy accuracy evaluation.

The overall solution is illustrated in Figure 7.1.

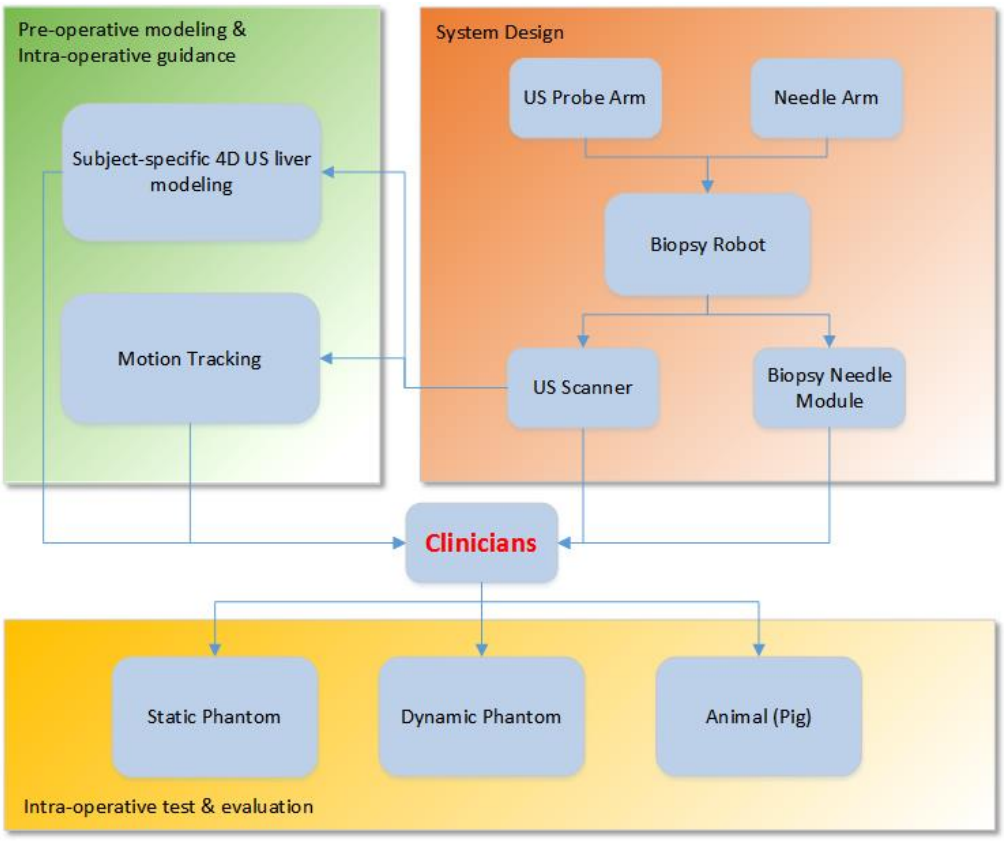

Figure 7.1 Solution with proposed techniques in an integrated manner

7.2 Recommendations for future work

The ultimate goal of this study is to provide a practical solution for the clinicians to handle the issue of respiratory liver motion, and thereby improve the efficiency of diagnose and accuracy of the biopsy treatment, by developing US-based tracking algorithm and US-image guided biopsy system, and applying them in an integrated way in the practice. It requires works to be done in multiple aspects to achieve this ultimate goal, and however, some of them are beyond this thesis, for example the design of the biopsy system. In this thesis, we have tried to solve the complicated liver motion problem in various directions, as predescribed. These efforts have been extensive, but are not exhaustive. Apart from the works I finished in the thesis, there are still

some future works to be done in each sub-project to get closer to the ultimate goal. The recommendations for future work are listed as follows.

In respiratory signal extraction, we plan to perform more detailed validation, on more subjects, with both normal and abnormal breathing patterns, and to further demonstrate the high relevance of special parts (such as the liver boundary and vessels) with respiration. We also plan to propose a robust method to automatically identify these special parts from intra-operative US images, and extract their respiratory signal as a valid surrogate. In addition, more kinds of searching algorithms could be applied to see if they can improve the searching efficiency.

In subject-specific liver modeling, since a strictly ground-truth respiratory signal is in general not available, the EM-tracked signal is instead applied as the reference for picking *EE/EI* pairs, thus generating ground truth image sequences for evaluation. Our next step is to acquire data on the dynamic liver phantom with known motion [180], and evaluate the accuracy of the suggested method. Further, the technique for easy creation of simulated tumors, together with the dynamic liver phantom, could provide a good testing subject to assess if the moving target can accurately be visualized using our proposed imaging and modeling method. In addition, we also plan to conduct more experiments on the patients, such that the subject-specific motion information of the real tumors can be observed and analyzed.

In phantom study, more experiments could be done to ascertain real liver deformation, and determine a regular pattern of this at predetermined locations. Deformation of the liver is irregular, or non-linear, due to the difference in the shape of the organ's different parts, as we can conclude from the paths of the

deformation of the liver provided by the 3 different markers. The experiment could be repeated with additional points closer to the 3 different positions used, to test if some of the areas have the same deformation pattern, especially those near to each other. From there, it could be possible to estimate the trend of a particular point or area of the liver.

In experimental study, more kinds of materials could be tried and tested to determine their capability and suitability for being the target of biopsy study. We are hoping to be able to explore and discover new combinations of materials that can be more easily produced and detected under US image. Moreover, since the biological properties of our proposed Vaseline-based mixture materials are far from those of real tumor tissue, when we explore the new materials, we could investigate their biological properties and sonomorphological characterizations as well, in the future work.

By applying these future works together in the future tests, the developing biopsy system can be better validated, until it achieves accurate biopsy under various conditions, and finally meets all the requirements for clinical trails, thereby reach the ultimate goal of this study.

BIOBLIOGRAPHY

1. World Health Organization (WHO), http://www.who.int/en/.
2. GC Farrell , M Arthur, D Christopher. Non-alcoholic Fatty Liver Disease: A Practical Guide. *John Wiley & Sons*, 2013.
3. AS Alghamdi, FM Sanai, M Ismail, et al. SASLT practice guidelines: Management of hepatitis C virus infection. *Saudi Journal of Gastroenterology*, 18.7: 1, 2012.
4. Source of figure: www.hivandhepatitis.com
5. AN Pedersen, S Korreman, H Nystrom, L Specht. Breathing adapted radiotherapy of breast cancer: reduction of cardiac and pulmonary doses using voluntary inspiration breath-hold. *Radiother. Oncol.*, 72(1):53-60, 2004.
6. C Nelson, G Starkschall, P Balter, MJ Fitzpatrick, JA Antolak, N Tolani, K Prado. Respiration-correlated treatment delivery using feedbackguided breath hold: A technical study. *Med. Phys*., 32(1):175-181, 2005.
7. R George, TD Chung, SS Vedam, V Ramakrishnan, R Mohan, E Weiss, PJ Keall. Audio-visual biofeedback for respiratory-gated radiotherapy: Impact of audio instruction and audio-visual biofeedback on respiratory-gated radiotherapy. Int. J. Radiat. *Oncol. Biol. Phys.*, 65(3):924-933, 2006.
8. S Jiang. Technical aspects of image-guided respiration-gated radiation therapy. *Medical Dosimetry*, 31(2):141-151, 2006.
9. H Shirato, S Shimizu, K Kitamura, R Onimaru. Organ motion in image-guided radiotherapy: lessons from real-time tumor-tracking radiotherapy. *Int. J. Clin. Oncol*., 12(1):8-16, 2007.
10. R Underberg, F Lagerwaard, B Slotman, J Cuijpers, S Senan. Benefit of respiration-gated stereotactic radiotherapy for stage I lung cancer: An analysis of 4DCT datasets. *Int. J. Radiat. Oncol. Biol. Phys.*, 62(2):554-560, 2005.
11. MJ Murphy. Tracking moving organs in real time. *Semin. Radiat. Oncol.*, 14(1):91-100, 2004.
12. JR McClelland, S Webb, D McQuaid, DM Binnie, and DJ Hawkes. Tracking 'diffierential organ motion' with a 'breathing' multileaf collimator: magnitude of problem assessed using 4D CT data and a motion-compensation strategy. *Phys. Med. Biol.*, 52(16):4805-26, 2007.
13. Y Kang, X Zhang, JY Chang, H Wang, X Wei, Z Liao, R Komaki, JD Cox, PA Balter, H Liu, XR Zhu, R Mohan, L Dong. 4D proton treatment planning strategy for mobile lung tumors. *Int. J. Radiat. Oncol. Biol. Phys.*, 67(3):906-914, 2007.

14. R Wagman, E Yorke, E Ford, P Giraud, G Mageras, B Minsky, K Rosenzweig. Respiratory gating for liver tumors: use in dose escalation. *Int. J. Radiat. Oncol. Biol. Phys.*, 55(3):659-668, 2003.

15. SS Vedam, VR Kini, PJ Keall, V Ramakrishnan, H Mostafavi, R Mohan. Quantifying the predictability of diaphragm motion during respiration with a noninvasive external marker. *Med. Phys.*, 30(4):505-513, 2003.

16. R George, SS Vedam, TD Chung, V Ramakrishnan, PJ Keall. The application of the sinusoidal model to lung cancer patient respiratory motion. *Med. Phys*., 32(9):2850-2861, 2005.

17. T Neicu, R Berbeco, J Wolfgang, and S Jiang. Synchronized moving aperture radiation therapy (SMART): improvement of breathing pattern reproducibility using respiratory coaching. *Phys. Med. Biol*., 51(3):617-636, 2006.

18. T Rohlfing, CR Maurer, Jr., WG O'Dell, and J Zhong. Modeling liver motion and deformation during the respiratory cycle using intensity-based nonrigid registration of gated MR images. *Med. Phys*., 31(3):427-432, 2004.

19. ED Brandner, A Wu, H Chen, D Heron, S Kalnicki, K Komanduri, K Gerszten, S Burton, I Ahmed, Z Shou. Abdominal organ motion measured using 4D CT. *Int J Radiat Oncol Biol Phys*, 65(2):554–560, 2006

20. M von Siebenthal, G Székely, AJ Lomax, PC Cattin. Systematic errors in respiratory gating due to intrafraction deformations of the liver. *Med. Phys*., 34(9): 3620-3629, 2007.

21. F Preiswerk, P Arnold, B Fasel, PC Cattin. Robust tumour tracking from 2D imaging using a population-based statistical motion model. *Mathematical Methods in Biomedical Image Analysis (MMBIA)*, 2012 IEEE Workshop on. IEEE, 209-214, 2012.

22. J Ehrhardt, R Werner, A Schmidt-Richberg, H Handels. Statistical Modeling of 4D Respiratory Lung Motion Using Diffeomorphic Image Registration. *Medical Imaging, IEEE Transactions on*, 30(2):251-265, 2011.

23. T He, Z Xue, W Xie, and STC Wong. Online 4-D CT Estimation for Patient-Specific Respiratory Motion Based on Real-Time Breathing Signals. *In Proc. MICCAI 2010*, pages 392-399. Springer, 2010.

24. A Hostettler, SA Nicolau, Y Rémond, et al. A real-time predictive simulation of abdominal viscera positions during quiet free breathing. *Progress in biophysics and molecular biology*, 103(2): 169-184, 2010.

25. M von Siebenthal, G Székely, A Lomax, P Cattin. Inter-Subject Modelling of Liver Deformation During Radiation Therapy. *In Proc. MICCAI 2007*, volume 4791 of LNCS, pages 659-666. Springer, 2007

26. A Khamene, JK Warzelhan, S Vogt, D Elgort, C Chefd'Hotel, JL Duerk, J Lewin, FK Wacker, F Sauer. Characterization of internal organ motion using skin marker positions. *In: Medical image computing and*

computer-assisted intervention-MICCAI 2004. Springer, New York, pp 526–533, 2004.

27. JM Blackall, GP Penney, AP King, DJ Hawkes. Alignment of sparse freehand 3-D ultrasound with preoperative images of the liver using models of respiratory motion and deformation. *IEEE Trans Med Imaging*, 24(11):1405-1416, 2005.

28. JR McClelland, DJ Hawkes, T Schaeffter, AP King. Respiratory motion models: A review. *Medical image analysis*. 17, 19-42, 2012

29. Liver - Wikipedia. Retrived Jun.11 2015, http://en.wikipedia.org/wiki/liver.

30. EJ Rijkhorst, I Rivens, GT Haar, D Hawkes, D Barratt. Effects of Respiratory Liver Motion on Heating for Gated and Model-Based Motion-Compensated High-Intensity Focused Ultrasound Ablation. *MICCAI 2011*, 605-612, 2011.

31. Source of figure: https://glutenfreedoms.files.wordpress.com/2012/12/breathing.jpg.

32. F Ernst, V Martens, S Schlichting, A Besirevic, M Kleemann, C Koch, D Petersen, A Schweikard. Correlating Chest Surface Motion to Motion of the Liver Using - SVR - A Porcine Study. *MICCAI 2009*, 356-364, 2009.

33. M von Siebenthal. Analysis and Modelling of Respiratory Liver Motion using 4DMRI. PhD thesis, *ETH ZURICH*, 2008

34. C Studholme, DLG Hill, DJ Hawkes. Automated Three-dimensional Registration of Magnetic Resonance and Positron Emission Tomography Brain Images by Multiresolution Optimization of Voxel Similarity Measures. *Med. Phys*., 24(1):25-35, 1997.

35. D Rueckert, LI Sonoda, C Hayes, DLG Hill, MO Leach, and DJ Hawkes. Nonrigid registration using free-form deformations: application to breast MR images. *IEEE T. Med. Imag*., 18(8):712-721, 1999.

36. WH Press, BP Flannery, SA Teukolsky, and WT Vetterling. Numerical recipes in C: the art of scientific computing, 2nd Edition. *Cambridge University Press*, New York, NY, USA, 1992.

37. C Randazzo, A Licata, PL Almasio. Liver Biopsy-Indications, Procedures, Results. *InTech*, 2012.

38. BW Loo Jr., IC Gibbs. Image-Guided Robotic Stereotactic Ablative Radiotherapy for Lung Tumors: The CyberKnife. *Advances in Radiation Oncology in Lung Cancer*. Springer Berlin Heidelberg, 715-724, 2012.

39. SC Davies, AL Hill, RB Holmes, M Halliwell, and PC Jackson. Ultrasound quantitation of respiratory organ motion in the upper abdomen. *Brit. J. Radiol.*, 67(803):1096-1102, 1994.

40. AE Lujan, JM Balter, and RK Ten Haken. A method for incorporating organ motion due to breathing into 3D dose calculations in the liver: Sensitivity to variations in motion. *Med. Phys*., 30(10):2643-2649, 2003.

41. K Kitamura, H Shirato, Y Seppenwoolde, T Shimizu, Y Kodama, H Endo, R Onimaru, M Oda, K Fujita, S Shimizu, K Miyasaka. Tumor location, cirrhosis, and surgical history contribute to tumor movement in the liver, as measured during stereotactic irradiation using a real-time tumor-tracking radiotherapy system. *Int. J. Radiat. Oncol. Biol. Phys.*, 56(1):221-228, 2003

42. Y Seppenwoolde, H Shirato, K Kitamura, S Shimizu, M van Herk, J Lebesque, K Miyasaka. Precise and real-time measurement of 3D tumor motion in lung due to breathing and heartbeat, measured during radiotherapy. *Int. J. Radiat. Oncol. Biol. Phys*., 53(4):822-834, 2002.

43. GS Mageras, A Pevsner, ED Yorke, KE Rosenzweig, EC Ford, A Hertanto, SM Larson, DM Lovelock, YE Erdi, SA Nehmeh, JL Humm, CC Ling. Measurement of lung tumor motion using respiration-correlated CT. *Int. J. Radiat. Oncol. Biol. Phys*., 60(3):933-941, 2004.

44. EWeiss, K Wijesooriya, SV Dill, PJ Keall. Tumor and normal tissue motion in the thorax during respiration: Analysis of volumetric and positional variations using 4D CT. *Int. J. Radiat. Oncol. Biol. Phys*., 67(1):296-307, 2007.

45. G Hugo, C Vargas, J Liang, L Kestin, JW Wong, and D Yan. Changes in the respiratory pattern during radiotherapy for cancer in the lung. *Radiother. Oncol*., 78(3):326-331, 2006.

46. A Aliverti, V Brusasco, PT Macklem, et al. Mechanics of Breathing. *Springer-Verlag*, 2002.

47. S Malone, JM Crook, WS Kendal, JS Zanto. Respiratoryinduced prostate motion: quantification and characterization. *Int. J. Radiat. Oncol. Biol. Phys*., 48(1):105-109, 2000.

48. JM Balter, RK Ten Haken, TS Lawrence, KL Lam, JM Robertson. Uncertainties in CT-based radiation therapy treatment planning associated with patient breathing. *Int. J. Radiat. Oncol. Biol. Phys.*, 36(1):167-174, 1996.

49. S Shimizu, H Shirato, H Aoyama, S Hashimoto, T Nishioka, A Yamazaki, K Kagei, K Miyasaka. High-speed magnetic resonance imaging for four-dimensional treatment planning of conformal radiotherapy of moving body tumors. *Int. J. Radiat. Oncol. Biol. Phys.*, 48(2):471-474, 2000.

50. MA Clifford, F Banovac, E Levy, K Cleary. Assessment of hepatic motion secondary to respiration for computer assisted interventions. *Comput. Aided Surg*., 7(5):291-299, 2002.

51. GD Hugo, D Yan, J Liang. Population and patient-specific target margins for 4D adaptive radiotherapy to account for intra- and inter-fraction variation in lung tumour position. *Phys. Med. Biol.*, 52(1):257-274, 2007.

52. JE Kennedy, F Wu, GR ter Haar, FV Gleeson, RR Phillips, MR Middleton, D Cranston. High-intensity focused ultrasound for the treatment of liver tumours. *Ultrasonics*, 42(1-9):931-935, 2004.

53. E Rietzel, GT Chen, NC Choi, CG Willet. Fourdimensional image-based treatment planning: Target volume segmentation and dose calculation in the presence of respiratory motion. *Int. J. Radiat. Oncol. Biol. Phys.*, 61(5):1535-1550, 2005.

54. M Rosu, JM Balter, IJ Chetty, ML Kessler, DL McShan, P Balter, RK Ten Haken. How extensive of a 4D dataset is needed to estimate cumulative dose distribution plan evaluation metrics in conformal lung therapy? *Med. Phys.*, 34(1):233-245, 2007.

55. PJ Keall, GS Mageras, JM Balter, RS Emery, KM Forster, S Jiang, JM Kapatoes, DA Low, MJ Murphy, BR Murray, CR Ramsey, MB van Herk, SS Vedam, JW Wong, E Yorke. The management of respiratory motion in radiation oncology report of AAPM task group 76. *Med. Phys*., 33(10):3874-3900, 2006.

56. Source of figure: http://www.medicalook.com/test_images/Needle_Biopsy.jpg.

57. QT Le, BW Loo, A Ho, C Cotrutz, AC Koong, H Wakelee, ST Kee, D Constantinescu, RI Whyte, J Donington. Results of a phase I doseescalation study using single-fraction stereotactic radiotherapy for lung tumors. *J. Thorac. Oncol*., 1(8):802-809, 2006.

58. GS Mageras, E Yorke, K Rosenzweig, L Braban, E Keatley, E Ford, SA Leibel, CC Ling. Fluoroscopic evaluation of diaphragmatic motion reduction with a respiratory gated radiotherapy system. *J. Appl. Clin. Med. Phys*., 2(4):191-200, 2001.

59. P Giraud, E Yorke, EC Ford, R Wagman, GS Mageras, H Amols, CC Ling, and KE Rosenzweig. Reduction of organ motion in lung tumors with respiratory gating. *Lung Cancer*, 51(1):41-51, 2006.

60. M Uematsu, A Shioda, A Suda, et al. Intrafractional tumor position stability during computed tomography (CT)-guided frameless stereotactic radiation therapy for lung or liver cancers with a fusion of CT and linear accelerator (FOCAL) unit. *Int. J. Radiat. Oncol. Biol. Phys.*, 48(2):443-448, 2000.

61. T Zhang, NP Orton, WA Tome. On the automated definition of mobile target volumes from 4D-CT images for stereotactic body radiotherapy. *Med. Phys*., 32(11):3493-3502, 2005.

62. K Herfarth, J Debus, F Lohr, ML Bahner, P Fritz, A Hoss, W Schlegel, MF Wannenmacher. Extracranial stereotactic radiation therapy: set-up accuracy of patients treated for liver metastases. *Int. J. Radiat. Oncol. Biol. Phys.*, 46(2):329-335, 2000.

63. W Lu, PJ Parikh, JP Hubenschmidt, JD Bradley, DA Low. A comparison between amplitude sorting and phase-angle sorting using external respiratory measurement for 4D CT. *Med. Phys.*, 33(8):2964-2974, 2006.

64. J Hanley, MM Debois, D Mah, et al. Deep inspiration breath-hold technique for lung tumors: the potential value of target immobilization and reduced lung density in dose escalation. *Int. J. Radiat. Oncol. Biol.*

Phys., 45(3):603-611, 1999.

65. JM Balter, KK Brock, DW Litzenberg, DL McShan, TS Lawrence, R Ten Haken, CJ McGinn, KL Lam, LA Dawson. Daily targeting of intrahepatic tumors for radiotherapy. *Int. J. Radiat. Oncol. Biol. Phys.*, 52(1):266-271, 2002.

66. R Koshani, JM Balter, JA Hayman, GT Henning, M van Herk. Short-term and long-term reproducibility of lung tumor position using active breathing control (ABC). *Int. J. Radiat. Oncol. Biol. Phys*., 65(5):1553-1559, 2006.

67. B Gagel, C Demirel, A Kientopf, M Pinkawa, M Piroth, S Stanzel, C Breuer, B Asadpour, T Jansen, R Holy, JE Wildberger, MJ Eble. Active breathing control (ABC): Determination and reduction of breathing-induced organ motion in the chest. *Int. J. Radiat. Oncol. Biol. Phys.*, 67(3):742-749, 2007.

68. VR Kini, SS Vedam, PJ Keall, S Patil, C Chen, and R Mohan. Patient training in respiratory-gated radiotherapy. *Medical Dosimetry*, 28(1):7-11, 2003.

69. PJ Keall, G Starkschall, H Shukla, KM Forster, V Ortiz, CW Stevens, SS Vedam, R George, T Guerrero, and R Mohan. Acquiring 4D thoracic CT scans using a multislice helical method. *Phys. Med. Biol*., 49(10):2053-2067, 2004.

70. SA Nehmeh, YE Erdi, T Pan, et al. Quantitation of respiratory motion during 4D-PET/CT acquisition. *Med. Phys*., 31(6):1333-1338, 2004.

71. MJ Fitzpatrick, G Starkschall, JA Antolak, J Fu, H Shukla, PJ Keall, P Klahr, and R Mohan. Displacement-based binning of time-dependent computed tomography image data sets. *Med. Phys*., 33(1):235-246, 2006.

72. J Dinkel, C Hintze, R Tetzlaff, PE Huber, K Herfarth, J Debus, C Thieke, 4D-MRI analysis of lung tumor motion in patients with hemidiaphragmatic paralysis. *Radiotherapy and Oncology*, 91(3), 449-454, 2009.

73. JM Blackall, S Ahmad, ME Miquel, JR McClelland, DB Landau, DJ Hawkes. MRI-based measurements of respiratory motion variability and assessment of imaging strategies for radiotherapy planning. *Physics in medicine and biology*, 51(17), 4147, 2006.

74. G Remmert, J Biederer, F Lohberger, M Fabel, and GH Hartmann. Four-dimensional magnetic resonance imaging for the determination of tumour movement and its evaluation using a dynamic porcine lung phantom. *Physics in medicine and biology*, 52(18), N401, 2007.

75. M von Siebenthal, G Szekely, U Gamper, P Boesiger, A Lomax, P Cattin. 4D MR imaging of respiratory organ motion and its variability. *Physics in medicine and biology*, 52(6), 1547, 2007.

76. J Tokuda, S Morikawa, HA Haque, T Tsukamoto, K Matsumiya, H Liao, T Dohi. Adaptive 4D MR imaging using navigator-based respiratory signal for MRI-guided therapy. *Magnetic Resonance in Medicine*, 59(5),

1051-1061, 2008.

77. C Plathow, S Ley, C Fink, M Puderbach, W Hosch, A Schmähl, HU Kauczor. Analysis of intrathoracic tumor mobility during whole breathing cycle by dynamic MRI. *International Journal of Radiation Oncology Biology Physics*, 59(4), 952-959, 2004.

78. H Shirato, K Suzuki, GC Sharp, K Fujita, R Onimaru, M Fujino, N Kato, Y Osaka, R Kinoshita, H Taguchi. Speed and amplitude of lung tumor motion precisely detected in four-dimensional setup and in real-time tumor-tracking radiotherapy. *Int. J. Radiat. Oncol. Biol. Phys*., 64(4):1229-1236, 2006.

79. Y Wang, PJ Rossman, RC Grimm, SJ Riederer, RL Ehman. Navigator-echo-based real-time respiratory gating and triggering for reduction of respiration effects in three-dimensional coronary MR angiography. *Radiology*, 198(1), 55-60, 1996.

80. J. Blackall, 'Respiratory Motion in Image-Guided Interventions of the Liver.' PhD thesis, University of London, 2002.

81. D Low, M Nystrom, E Kalinin, P Parikh, et al. A method for the reconstruction of four-dimensional synchronized CT scans acquired during free breathing. *Med. Phys*. 30:1254–1263, 2003.

82. E Ford, G Mageras, E Yorke, C Ling. Respiration-correlated spiral CT: A method of measuring respiratory-induced anatomic motion for radiation treatment planning. *Med. Phys*. 30:88-97, 2003.

83. T Pan, T Lee, E Rietzel, G Chen. 4D-CT imaging of a volume influenced by respiratory motion on multi-slice CT. *Med. Phys*. 31:333-340, 2004.

84. J McClelland, A Chandler, J Blackall, et al. Feasibility study of a novel technique for constructing respiratory motion models, for use in 4D lung cancer radiotherapy planning. *In: Proc. MIUA*. 220-223, 2004.

85. A Fenster, DB Downey, HN Cardinal. Three-dimensional ultrasound imaging, *Phys. Med. Biol.* 46: R67, 2001.

86. H Neshat, DW Cool, K Barker, L Gardi, N Kakani, A Fenster. A 3D ultrasound scanning system for image guided liver interventions, *Med. Phys.* 40, 2013.

87. OV Solberg, F Lindseth, H Torp, RE Blake, TN Hernes. Freehand 3D ultrasound reconstruction algorithms – a review. *Ultrasound Med. Biol*. 33: 991–1009, 2007.

88. M Nakamoto, H Hirayama, Y Sato, K Konishi, Y Kakeji, M Hashizume, et al. Recovery of respiratory motion and deformation of the liver using laparoscopic freehand 3D ultrasound system, *Med. Image Anal.* 11: 429–42, 2007.

89. C Wachinger, M Yigitsoy, EJ Rijkhorst, N Navab. Manifold learning for image-based breathing gating in ultrasound and MRI. *Med. Image Anal*. 16: 806–18, 2012.

90. J de Koste et al. Renal mobility during uncoached quiet respiration: An analysis of 4DCT scans. *Int. J. Radiat. Oncol. Biol. Phys*. 64, 799-803, 2006.

91. RA Beasley. Medical Robots: Current Systems and Research Directions. Journal of Robotics. 1-14, 2012.

92. H Ho, JSP Yuen, CWS Cheng. Robotic prostate biopsy and its relevance to focal therapy of prostate cancer. *Nature Reviews Urology*. 8, 579–585, 2011.

93. J Blackall, S Ahmad, M Miquel, et al. Modelling respiratory motion for optimisation of lung cancer radiotherapy using fast MR imaging and intensity-based image registration. *In: Proc. Intl. Soc. Mag. Reson. Med*. 12: 2610, 2004.

94. R Bruder, F Ernst, A Schlaefer, A Schweikard. A Framework for Real-Time Target Tracking in Radiosurgery using Three-dimensional Ultrasound. *CARS 2011*. pp. S306–S307, 2011.

95. C Nadeau, A Krupa, J Gangloff. Automatic Tracking of an Organ Section with an Ultrasound Probe: Compensation of Respiratory Motion. In: Fichtinger, G., Martel, A., and Peters, T. (eds.) *MICCAI 2011*. pp. 57–64. Springer Berlin Heidelberg, 2011.

96. Anatomy and physiology of the liver - Canadian Cancer Society. Cancer.ca. Retrived Jun.11 2015, http://www.cancer.ca/en/cancer-information/cancer-type/liver/anatomy-and-physiology.

97. EJ Rijkhorst, D Heanes, F Odille, D Hawkes, D Barratt. Simulating Dynamic Ultrasound Using MR-derived Motion Models to Assess Respiratory Synchronisation for Image-Guided Liver Interventions. In: Navab, N. and Jannin, P. (eds.) *IPCAI 2010*. pp. 113–123. Springer Berlin / Heidelberg (2010).

98. P Arnold, F Preiswerk, B Fasel, R Salomir, K Scheffler, PC Cattin. 3D organ motion prediction for MR-guided high intensity focused ultrasound. In: Yoshida, H., Sakas, G., and Linguraru, M. (eds.) *MICCAI 2011*. pp. 623–30. Springer, Heidelberg, 2011.

99. JM Balter, LA Dawson, S Kazanjian, C McGinn, KK Brock, T Lawrence, and R Ten Haken. Determination of ventilatory liver movement via radiographic evaluation of diaphragm position. *Int. J. Radiat. Oncol. Biol. Phys.*, 51(1):267-270, 2001.

100. F Ernst, R Bruder, A Schlaefer, A Schweikard. Correlation between external and internal respiratory motion: a validation study. *International journal of computer assisted radiology and surgery (IJCARS)*. pp. 483–92, 2012.

101. DM Tsai, CT Lin, JF Chen. The evaluation of normalized cross correlations for defect detection. *Pattern Recognition Letters*. 24, 2525–2535, 2003.

102. C Tanner, D Boye, G Samei, G Szekely. Review on 4D models for organ motion compensation. *Crit RevTM Biomed Eng* 40(2), 2012.

103. S Golnoosh, C Tanner, G Székely. Predicting liver motion using exemplar models. *Abdominal Imaging. Computational and Clinical Applications.* Springer Berlin Heidelberg, 147-157, 2012.

104. W Wolfgang, JZ Cheng, A Khamene. Ultrasound based respiratory motion compensation in the abdomen. *MICCAI 2008 Worshop on Image Guidance and Computer Assistance for Softissue Intervetions*, 32.6: 294, 2008.

105. S Nicolau, X Pennec, L Soler, N Ayache. Clinical evaluation of a respiratory gated guidance system for liver punctures. *In: Medical image computing and computer-assisted intervention-MICCAI 2007*. Springer, Berlin, pp 77-85, 2007.

106. P Biro, D Spahn, T Pfammatter. High-frequency jet ventilation for minimizing breathing-related liver motion during percutaneous radiofrequency ablation of multiple hepatic tumours. *Br J Anaesth*, 102(5):650–653, 2009.

107. W Wunderink, AM Romero. Reduction of respiratory liver tumor motion by abdominal compression in stereotactic body frame, analyzed by tracking fiducial markers implanted in liver. *Int J Radiat Oncol Biol Phys*, 71(3):907-915, 2008.

108. VM Remouchamps, N Letts, FA Vicini, MB Sharpe, LL Kestin, PY Chen, AA Martinez, JW Wong. Initial clinical experience with moderate deep-inspiration breath hold using an active breathing control device in the treatment of patients with left-sided breast cancer using external beam radiation therapy. *Int J Radiat Oncol Biol Phys* 56(3):704–715, 2003.

109. M Yang, H Ding, J Kang, et al. Subject-specific real-time respiratory liver motion compensation method for ultrasound-MRI/CT fusion imaging. *International journal of computer assisted radiology and surgery (IJCARS)*, 10(5): 517-529, 2015.

110. G Renault, F Tranquart, V Perlbarg, et al. A posteriori respiratory gating in contrast ultrasound for assessment of hepatic perfusion. *Physics in medicine and biology*, 50(19): 4465, 2005.

111. K Sugimoto, J Shiraishi, F Moriyasu, et al. Computer-aided diagnosis of focal liver lesions by use of physicians' subjective classification of echogenic patterns in baseline and contrast-enhanced ultrasonography. *Academic radiology*, 16(4): 401-411, 2009.

112. DP Gierga, J Brewer, GC Sharp, M Betke, CG Willett, GT Chen. The correlation between internal and external markers for abdominal tumors: implications for respiratory gating. *Int J Radiat Oncol Biol Phys* 61(5):1551-1558, 2005.

113. AD Groote, M Wantier, G Chéron, M Estenne, M Paiva. Chest wall motion during tidal breathing. *J Appl Physiol*, 83(5):1531-1537, 1997.

114. MIUE: Model-based Image Understanding Environment, http://www.hexalotus.com/technology/miue/

115. J Wu, C Li, S Huang, et al. Fast and robust extraction of surrogate respiratory signal from intra-operative liver ultrasound images. *International journal of computer assisted radiology and surgery (IJCARS)*. 8(6): 1027-1035, 2013.

116. J Wu, A Gogna, BS Tan, LL Ooi, Q Tian, F Liu, J Liu. A manifold learning method to detect respiratory signal from liver ultrasound images. *Computerized Medical Imaging and Graphics*, 40: 194-204, 2015.

117. Q Peng, RC Jones, CE Constantinou. 2D Ultrasound image processing in identifying responses of urogenital structures to pelvic floor muscle activity. *Annals of biomedical engineering* 34.3: 477-493, 2006.

118. M Xi, MZ Liu, QQ Li, et al. Analysis of abdominal organ motion using four-dimensional CT. *Chinese journal of cancer*, 28(9): 989-993, 2009..

119. Y Zhang, D Boye, C Tanner, AJ Lomax, A Knopf. Respiratory liver motion estimation and its effect on scanned proton beam therapy. *Phys Med Biol*, 57(7), 1779-1795, 2012.

120. H Zhang, F Banovac, K Cleary. Increasing registration precision for liver movement with respiration using electromagnetic tracking. *International Congress Series* 1281:571-576, 2005.

121. SM Thompson, JC Giraldo, B Knudsen, JP Grande, et al. Porcine Ex Vivo Liver Phantom for Dynamic Contrast-Enhanced Computed Tomography: Development and Initial Results. *Invest Radiol*. 46(9): 586-593, 2011.

122. L Maier-Hein, SA Muller, F Pianka, et al. Respiratory motion compensation for CT-guided interventions in the liver. *Computer Aided Surgery*, 13(3): 125-138, 2008.

123. K Cleary, F Banovac, E Levy, D Tanaka. Development of a Liver Respiratory Motion Simulator to Investigate Magnetic Tracking for Abdominal Interventions. *Medical Imaging 2002: Visualization, Image-Guided Procedures, and Display*, 2002.

124. F Banovac, J Tang, S Xu, D Lindisch, HY Chung, EB Levy, T Chang, MF McCullough, Z Yaniv, BJ Wood, K Cleary. Precisiontargeting of liver lesions using a novel electromagnetic navigation device in physiologic phantom and swine. *Med. Phys*., 32(8), 2698-2705, 2005.

125. NE Swailes, ME MacDonald, R Frayne. Dynamic Phantom with Heart, Lung, and Blood Motion for Initial Validation of MRI Techniques. *J. Magnetic Resonance Imaging*, 34:941-946, 2011.

126. R Kashani, K Lam, D Litzenberg, J Balter. Technical note: a deformable phantom for dynamic modeling in radiation therapy. *J. Medical physics*, 34(1): 199-201, 2006.

127. MJ Fitzpatrick, G Starkschall, P Balter, JA Antolak, T Guerrero, C Nelson, PJ Keall, R Mohan. A novel platform simulating irregular motion to enhance assessment of respiration-correlated radiation therapy procedures. *Journal of Applied Clinical Medical Physics*, 6(1), 2005.

128. M Wagar, E Mannarino, C Williams, F Hacker, R Berbeco J Lewis. SU−E−J−141: A Patient Specific Anthropomorphic Breathing Phantom for Clinically Realistic Imaging and Dosimetry Studies. *J. Medical Physics*, 40(6): 183, 2013.

129. S Kee, E Larsen, K Paluch, R Sinke, KC Yan, JJ Pilla, X Chun. Development of a dynamic heart phantom prototype for Magnetic Resonance Imaging. *Bioengineering Conference, Proceedings of the 2010 IEEE 36th Annual Northeast. IEEE*, 1-2, 2010.

130. SA Lopez-Haro, CJ Trujillo, A Vera, et al. An agarose based phantom embedded in an in vitro liver tissue to simulate tumors: First experience. *Health Care Exchanges (PAHCE), 2011 Pan American*. IEEE, 233-236, 2011.

131. M Szegedi, P Rassiah-Szegedi, G Fullerton, et al. A proto-type design of a real-tissue phantom for the validation of deformation algorithms and 4D dose calculations. *Physics in medicine and biology*, 55(13): 3685, 2010.

132. LA Drever, M Hilts. Daily quality assurance phantom for ultrasound image guided radiation therapy. *Journal of Applied Clinical Medical Physics*, 8(3), 2007.

133. MK Chmarra, R Hansen, R Mårvik, T Langø. Multimodal Phantom of Liver Tissue. *PLoS ONE* 8(5): e64180, 2013.

134. S Buchanan, J Moore, D Lammers, J Baxter, T Peters, et al. Characterization of tissue-simulating phantom materials for ultrasound-guided needle procedures. *Proc. of SPIE* Vol. 8316. 2012.

135. The CIRS Dynamic Thorax Phantom (Product Code: 008A). Available: http://www.medicaldevicedepot.com/Dynamic-Thorax-Phantom-p/008a.htm.

136. DC Wolf .Evaluation of the Size, Shape, and Consistency of the Liver. in: H. K. Walker, W. D. Hall, and J. W. Hurst (Ed.), *Clinical Methods: The History, Physical, and Laboratory Examinations*, Butterworths, 1990.

137. JM Rubin, M Feng, SW Hadley, JB Fowlkes. Potential Use of Ultrasound Speckle Tracking for Motion Management During Radiotherapy. *Journal of Ultrasound in Medicine*, 31(3), 469-481, 2011.

138. Firgelli L16 actuator. http://www.firgelli.com/products.php?id=42

139. Terason t3000 ultrasound system, http://www.terason.com/products/t3000.asp.

140. DJ Scott, WN Young, LM Watumull, G Lindberg, JB Fleming, RV Rege et al. Development of an in vivo tumor-mimic model for learning radiofrequency ablation, *J Gastrointest Surg*. 4:620–625, 2000.

141. DL Eckberg, YT Kifle, VL Roberts. Phase relationship between normal human respiration and baroreflex responsiveness. *The Journal of Physiology*, 304(1): 489-502, 1980.

142. SN Goldberg, GS Gazelle, CC Compton, PR Mueller, TC McLoud.

Radio-frequency tissue ablation of VX2 tumor nodules in the rabbit lung. *Acad Radiol*, 3:929–935, 1996.

143. JM Lee, GY Jin, CA Li, GH Chung, SY Lee, YM Han, et al. Percutaneous radiofrequency thermal ablation of lung VX2 tumors in a rabbit model using a cooled tip-electrode: feasibility, safety, and effectiveness. *Invest Radiol,* 38:129–139, 2003.

144. T Okuma, T Matsuoka, T Okamura, Y Wada, A Yamamoto, Y Oyama, et al. 18F-FDG small animal monitoring the therapeutic effect of CT-guided radiofrequency ablation on implanted VX2 lung tumors in rabbits. *J Nucl Med*, 47:1351–1358, 2006.

145. Y Miao, Y Ni, H Bosmans, J Yu, J Vaninbroukx, S Dymarkowski, et al. Radiofrequency ablation for eradication of pulmonary tumor in rabbits. *J Surg Res*, 99: 265–271, 2001.

146. R Watanabe, M Matsumura, CJ Chen, Y Kaneda, M Fujimaki. Characterization of tumor imaging with microbubble-based ultrasound contrast agent, Sonazoid, in rabbit liver. *Biol Pharm Bull*. 28(6): 972-977, 2005.

147. K Ahrar, DC Madoff, S Gupta, MJ Wallace, RE Price, KC Wright. Development of a large animal model for lung tumors. *J Vasc Interv Radiol*, 13:923–928, 2002.

148. K Ahrar, RE Price, MJ Wallace, DC Madoff, S Gupta, FA Morello Jr., et al. Percutaneous radiofrequency ablation of lung tumors in a large animal model. *J Vasc Interv Radiol*.

149. H Nomori, Y Imazu, K Watanabe, T Ohtsuka, T Naruke, T Kobayashi, et al. Radiofrequency ablation of pulmonary tumors and normal lung tissue in swine and rabbits. *Chest*. 127:973–977, 2005.

150. GD Taylor, JA Cadeddu. Training for renal ablative technique using an agarose-based renal tumour-mimic model. *BJU Int*. 97:179–181, 2006.

151. P Hildebrand, M Kleemann, U Roblick, L Mirow, HP Bruch, C Bürk. Development of a perfused ex vivo tumor-mimic model for the training of laparoscopic radiofrequency ablation, *Surg Endosc*. 21:1745–1749, 2007.

152. MD Mitchell, HL Kundel, L Axel, PM Joseph. Agarose as a tissue equivalent phantom material for NMR imaging. *Magn Reson Imaging*. 4(3): 263-266, 1986.

153. B Luo, R Yang, P Ying, M Awad, M Choti, R Taylor. Elasticity and echogenicity analysis of agarose phantoms mimicking liver tumors. *Bioengineering Conference*, 2006. Proceedings of the IEEE 32nd Annual Northeast. IEEE, 81-82, 2006.

154. D Selle, B Preim, A Schenk, HO Peitgen. Analysis of vasculature for liver surgical planning. *IEEE Trans Med Imaging*. 21(11): 1344–1357, 2002.

155. CK Wong, CS Chung. Probabilistic vessel axis tracing and its

application to vessel segmentation with stream surfaces and minimum cost paths. *Med Image Anal*. 11(6): 567–587, 2007.

156. A Gooya, L Hongen, K Matsumiya, K Masamune, Y Masutani, T Dohi. A variational method for geometric regularization of vascular segmentation in medical images. *IEEE Trans Image Process*. 17(8): 1295–1312, 2008.

157. R Manniesing, BK Velthuis, MS Leeuwen, IC Schaaf, PJ Laar, WJ Niessen. Level set based cerebral vasculature segmentation and diameter quantification in CT angiography. *Med Image Anal*. 10(2): 200–214, 2006.

158. C Florin, N Paragios, J Williams. Particle Filters, a Quasi-Monte Carlo Solution for Segmentation of Coronaries. In: Proceedings of international conference on *Medical Image Computing and Computer-Assisted Intervention (MICCAI)*. 3749: 246–53, 2005.

159. PH Kitslaar, M Frenay, E Oost, J Dijkstra, B Stoe, J Reiber. Connected component and morphology based extraction of arterial centerlines of the heart. In: Proceedings of international conference on *Medical Image Computing and Computer-Assisted Intervention (MICCAI)*, 2008.

160. SD Olabarriaga, M Breeuwer, WJ Niessen. Minimum cost path algorithm for coronary artery central axis tracking in CT Images. In: Proceedings of international conference on *Medical Image Computing and Computer-Assisted Intervention (MICCAI)*. 2879: 687–694, 2003.

161. A Szymczak, A Stillman, A Tannenbaum, K Mischaikow. Coronary vessel trees from 3D imagery: A topological approach. *Med Image Anal*. 10(4): 548–59, 2006.

162. D Lesage, ED Angelini, I Bloch, GF Lea. A review of 3D vessel lumen segmentation techniques: Models, features and extraction schemes. *Med Image Anal*. 13(6): 819–845, 2009.

163. S Esneault, C Lafon, JL Dillenseger. Liver vessels segmentation using a hybrid geometrical moments/graph cuts method. *IEEE Trans Biomed Eng*. 57(2): 276–1283, 2010.

164. C Bauer, T Pock, E Sorantin, H Bischof, R Beichel. Segmentation of interwoven 3d tubular tree structures utilizing shape priors and graph cuts. *Med Image Anal*. 14(2): 172–184, 2010.

165. O Friman, M Hindennach, C Kuhnel, HO Peitgen. Multiple hypothesis template tracking of small 3D vessel structures. *Med Image Anal*. 14(2): 160–171, 2010.

166. B Chen, T Kitasaka, H Honma, H Takabatake, M Mori, H Natori, K Mori. Automatic segmentation of pulmonary blood vessels and nodules based on local intensity structure analysis and surface propagation in 3D chest CT images. *Int J CARS*, 7(3): 465-482, 2012.

167. X Zhou, T Hayashi, T Hara, H Fujita, R Yokoyama, T Kiryu, H Hoshi. Automatic segmentation and recognition of anatomical lung structures from high-resolution chest CT images. *Computerized Medical Imaging*

and Graphics. 30: 299-313, 2006.

168. JN Kaftan, AP Kiraly, A Bakai, M Das, CL Novak, T Aach. Fuzzy pulmonary vessel segmentation in contrast enhanced CT data. *In: Proc of SPIE, Image Processing*. 6914: 1Q 1-12, 2008.

169. H Shikata, G McLennan, EA Hoffman, M Sonka. Segmentation of Pulmonary Vascular Trees from Thoracic 3D CT Images. *Int J Biomed Imaging*. 2009: 24.

170. H Shikata, EA Hoffman, M Sonka. Automated segmentation of pulmonary vascular tree from 3D CT images. *In: Proc of SPIE, Physiology, Function, and Structure from Medical Images*. 5369: 107-16, 2004.

171. C Zhou, H Chan, B Sahiner, L Hadjiiski, A Chughtai, S Patel, J Wei, J Ge, PN Cascade, EA Kazerooni. Automatic multiscale enhancement and segmentation of pulmonary vessels in CT pulmonary angiography images for CAD applications. *Med Phys*. 34(12): 4567-4577, 2007.

172. M Niemeijer, J Staal, BV Ginneken, M Loog, M Abramoff. Comparative study of retinal vessel segmentation methods on a new publicly available database. *In: Proc of SPIE, Image Processing*. 5370: 648, 2004.

173. C Lupascu, D Tegolo, E Trucco. Fabc: Retinal vessel segmentation using adaboost. *IEEE Trans Information Technology in Biomedicine*. 14(5): 1267–1274, 2010.

174. ME Gegúndez-Arias, A Aquino, JM Bravo, D Marín. A Function for Quality Evaluation of Retinal Vessel Segmentations. *IEEE Trans Med Imaging*. 31(2): 231-239, 2012.

175. UTV Nguyen, K Ramamohanarao, LAF Park. A Quantitative Measure for Retinal Blood Vessel Segmentation Evaluation. *Int J Comput Vision and Signal Processing*. 1(1): 1-8, 2012.

176. A Baddeley. An error metric for binary images. *Robust Computer Vision*. 5978, 1992.

177. I Abdou, W Pratt. Quantitative design and evaluation of enhancement/ thresholding edge detectors. *In Proceedings of IEEE*. 67(5): 753–763, 1979.

178. P Jaccard. Etude comparative de la distribution florale dans une portion des alpes et des jura. *Bull Soc Vaudoise Sci Nat*. 37: 547–579, 1901.

179. Y Chi, J Liu, SK Venkatesh, S Huang, J Zhou, Q Tian, WL Nowinski. Segmentation of Liver Vasculature From Contrast Enhanced CT Images Using Context-Based Voting. *IEEE Trans Biomed Eng*. 58(8): 2144-2153, 2011.

180. C Li, SP Ang, J Liu, H Yu. A Dynamic Liver Phantom for Ultrasound Image Guided Biopsy. In *15th International Conference on Biomedical Engineering (ICBME)*, Springer International Publishing, 152-155, 2014.

181. EJ Harris, NR Miller, JC Bamber, JRN Symonds-Tayler, PM Evans. Speckle tracking in a phantom and feature-based tracking in liver in the

presence of respiratory motion using 4D ultrasound. *Phys Med Biol*, 55(12): 3363, 2010.

182. V De Luca, M Tschannen, G Székely, C Tanner. A learning-based approach for fast and robust vessel tracking in long ultrasound sequences. In *Medical Image Computing and Computer-Assisted Intervention (MICCAI)*, Springer Berlin Heidelberg, 518-525, 2013.
183. Y Kubota, A Matsumura, M Fukahori, SI Minohara, S Yasuda, H Nagahashi. A new method for tracking organ motion on diagnostic ultrasound images. *Medical physics*, 41(9): 092901, 2014.
184. A Abdouni, B Presles, M Fargier-Voiron, S Rit, D Sarrut. Development of 2D+T tracking algorithm in ultrasound images for radiotherapy. In *Engineering in Medicine and Biology Society (EMBC)*, 2015 37th Annual International Conference of the IEEE, 2916-2919, 2015.
185. V De Luca, G Székely, C Tanner. Estimation of Large-Scale Organ Motion in B-Mode Ultrasound Image Sequences: A Survey. *Ultrasound in Medicine & Biology*, 41(12): 3044-3062, 2015.
186. Y Seo, T Ishizu, K Aonuma. Current status of 3-dimensional speckle tracking echocardiography: a review from our experiences. *Journal of cardiovascular ultrasound*, 22(2): 49-57, 2014.